

DISCOVERY OF NEW DWARF GALAXIES IN THE M81 GROUP

KRISTIN CHIBOUCAS¹, IGOR D. KARACHENTSEV², AND R. BRENT TULLY¹
Draft version October 25, 2021

ABSTRACT

An order of magnitude more dwarf galaxies are expected to inhabit the Local Group, based on currently accepted galaxy formation models, than have been observed. This discrepancy has been noted in environments ranging from the field to rich clusters. However, no complete census of dwarf galaxies exists in any environment. The discovery of the smallest and faintest dwarfs is hampered by the limitations in detecting such faint and low surface brightness galaxies. An even greater difficulty is establishing distances to or group/cluster membership for such faint galaxies. The M81 Group provides an almost unique opportunity for establishing membership for galaxies in a low density region complete to magnitudes as faint as $M_r = -10$. With a distance modulus of 27.8, the tip of the red giant branch just resolves in ground-based surveys. We have surveyed a 65 square degree region around M81 with CFHT/MegaCam. From these images we have detected 22 new dwarf galaxy candidates. Photometric, morphological, and structural properties are presented for the candidates. The group luminosity function has a faint end slope characterized by the parameter $\alpha = -1.27 \pm 0.06$. We discuss implications of this dwarf galaxy population for cosmological models.

Subject headings: galaxy groups: individual (M81) - galaxies: dwarf - galaxies: luminosity function - galaxies: photometry - galaxies: fundamental parameters (classification, luminosities, colors, radii)

1. INTRODUCTION

Standard Λ CDM, hierarchical structure formation models predict an order of magnitude more low mass halos in group environments and as satellites around Milky Way-like galaxies than there are observed dwarf galaxies (Klypin et al. 1999; Moore et al. 1999). The steeper slope of the predicted mass function over the observed luminosity function (LF) is the source of the ‘missing galaxy’ problem. There is growing evidence that there are fewer dwarfs than predicted in all environments, but the situation is even worse in field and group environments. Simulations predict low density environments to have fractionally more dwarfs than the high density cluster regions, whereas observationally the reverse has been measured (Roberts et al. 2004; Trentham et al. 2005; Roberts et al. 2007; Blanton et al. 2005; Barkhouse et al. 2007).

Several explanations to resolve this discrepancy between theory and observations have been proposed. Cosmological solutions include modifying the power spectrum on small scales (Kamionkowski & Liddle 2000), perhaps by invoking warm dark matter (Colín et al. 2000). Numerical simulations generally predict subhalo counts as a function of total mass or maximum circular velocity. For Local Group satellites, these values are not well determined, making direct comparison between these models and observations difficult unless other parameters, such as the mass within a specific radius, are used (Strigari et al. 2007). However, these more appropriate comparisons still find predictions inconsistent with observations.

A large number of astrophysical solutions have been put forth to explain the apparent underabundance of dwarf galaxies. Number counts can be brought into agreement

with models if it is assumed the observed dwarf galaxies reside in relatively massive dark matter halos while lower mass halos remain invisible (Stoehr et al. 2002). If star formation efficiency is lower in lower density halos, or if large gas reservoirs are expelled from small potential wells after an initial burst of star formation and subsequent supernova activity, low mass galaxies will remain fairly dark and difficult to detect. Greater numbers of visible dwarfs might then be expected to inhabit the high density, high gas pressure environment of rich clusters if the intracluster medium served to contain the dwarf galaxy outflows (Babul & Rees 1992). For very small masses, cooling times may be greater than the age of the universe (Haiman et al. 1996). Destructive processes which act in rich environments such as clusters may decrease dwarf number counts or lower luminosities making them more difficult to detect. Such processes include harassment, strangulation, and ram pressure stripping (Moore et al. 1996; Shaya & Tully 1984; Bekki et al. 2001b; Mori & Burkert 2000) and would be expected to play a larger role in shaping galaxy populations in denser, more massive, and hotter clusters. Instead, high density regions have been observed to contain a larger fraction of dwarf to giant galaxies than low density regions.

Another theory argues that reionization suppresses the collapse of gas in low mass halos thereby producing a shallower faint-end slope in the luminosity function (Thoul & Weinberg 1996). This process will not affect gas accretion in halos that collapsed before the era of reionization - those that resided in denser regions, such as rich clusters, would preferentially collapse earlier when intergalactic gas was still cold and halos could accumulate the gas. Reionization will therefore predominantly suppress baryon

1

Institute for Astronomy, University of Hawaii, 2680 Woodlawn Dr., Honolulu, HI 96821

2

Special Astrophysical Observatory (SAO)

accumulation in low mass halos in lower density regions such as the poorer group and field environment, naturally explaining the trend of lower dwarf-to-giant ratios found in lower density regions (Tully et al. 2002). In support of this theory, Strigari et al. (2007) and Simon & Geha (2007) find good agreement with theoretical expectations if the observed Local Group satellites correspond to the earliest collapsed halos, or the most massive at the time of accretion.

Distinguishing between all these possibilities has proven difficult, but before we can draw any conclusions as to the source of the discrepancy, we must first constrain the number counts of dwarf galaxies and the faint-end slope of the luminosity function. No complete census of dwarf galaxies has been obtained in any environment, although much recent progress has been made in the detection of faint Local Group satellites. With SDSS survey releases, the number of known Milky Way and M31 satellites has nearly doubled in just the past 4 years (Simon & Geha 2007). This new information has mitigated the missing galaxy problem, but has not brought the number counts into alignment with Λ CDM predictions. Due to the sky coverage required for a complete survey and restrictions caused by the zone of obscuration, a complete census of Local Group dwarf galaxies is not on the horizon.

The determination of the faint-end of the galaxy luminosity function is hampered by the limitations in detecting the very faintest and lowest surface brightness galaxies, and this is compounded by the the great difficulty in determining accurate distances to, or ascertaining group and cluster membership for, such faint objects. To measure the faint-end of the luminosity function for nearby clusters of galaxies, researchers have often resorted to using statistical means to estimate cluster memberships (see e.g. Bernstein et al. (1995); Trentham (1997); Chiboucas & Mateo (2007)). Others use colors or morphology in an attempt to directly assess membership probability (Secker et al. 1997; Mahdavi et al. 2005). All these methods are fraught with large uncertainty. Spectroscopy can be used to establish membership, but to observe the large numbers of galaxies to the necessary depth is prohibitively time consuming.

The M81 Group provides an alternative means to directly establish membership for galaxies to magnitudes as faint as $M_R \sim -7$ in a low density environment. Residing at a distance of only 3.6 Mpc, the galaxies in this group resolve into stars. Supergiants and giants near the tip of the red giant branch (TRGB) resolve over the diffuse main sequence population light. The degree of resolution is enough to establish the group membership status with high confidence. From color-magnitude diagrams, one can determine TRGB distances to unambiguously assign membership. Given this fortuitous circumstance, we can probe the faint-end of the LF in a group environment down to $M_R \sim -9$ to high accuracy.

The M81 Group is embedded in a filament of galaxies that runs up from behind the Galactic plane, shown in Figure 1. The M81 Group has traditionally been considered to include the galaxies around NGC 2403 and those around NGC 4236, each about 800 kpc removed in projection from M81. Maffei 1-2 and IC 342 are considered to be the dominant members of a separate group, 2 Mpc away in projection. The nearest neighbors at higher supergalactic lon-

gitude are a group around M101 at SGL=64, SGB=+23 and the near Canes Venatici group at SGL=76, SGB=+9. It has been shown by Karachentsev et al. (2002a) that the subcomponents of the M81 Group around NGC 2403 and M81 itself are falling toward each other, consistent with a total mass within the zero velocity surface bounding the group of $1.6 \times 10^{12} M_\odot$. The interest of the present study is the more dynamically evolved subcomponent around M81 contained within the box in Fig. 1.

We surveyed a 8×8 degree area centered on the M81 Group at $\alpha = 10:05:00$ $\delta = 68:15:00$ J2000 to search for new dwarf members of the group. Apart from the five brightest systems: M81, M82, NGC 2976, NGC 3077, and IC 2574, the inspected area contains 13 previously known dwarf galaxies which were discovered in the 1960-80s on POSS-I prints and the Tautenburg Schmidt telescope plates: Holm I, BK3N, KDG 61, Holm IX, Anon 0952 (Arp's loop), Garland, BK5N, KDG 63, KDG 64, HS 117, DDO 78, DDO 82, and BK6N (van den Bergh 1966; Karachentseva 1968; Boerngen & Karachentseva 1982, 1985). Later, 4 low surface brightness dwarfs: F8D1, FM1, KK 77, and IKN were found on POSS-II films by Caldwell et al. (1998), Froebrich & Meusinger (2000), Karachentsev et al. (2000), and Karachentsev et al. (2004).

Here we report on the discovery of 22 new M81 Group galaxy candidates. In Section 2 we present the observations and data reduction for our survey along with a discussion of the dwarf galaxy detection techniques, survey limits, and follow-up observations. We provide measurements of the properties of the newly discovered dwarf candidates in Section 3.1 and construct the total group LF in Section 3.2. We discuss the dwarf population characteristics in Section 4.1, the distribution of M81 satellites in Section 4.2, and implications of our survey results on the faint-end of the galaxy luminosity function and for cosmological models in Sections 4.3 and 4.4. Conclusions are presented in Section 5. Throughout this work we assume a distance modulus to M81 of 27.80 (3.6 Mpc).

2. OBSERVATIONS AND DATA REDUCTION

2.1. Initial survey

The M81 Group was chosen in large part because it is near enough at 3.6 Mpc that stars near the tip of the red giant branch just resolve in ground-based images, enabling derivation of the group luminosity function complete down to very faint magnitudes. Stars in Local Group galaxies resolve down to fainter magnitudes but a complete survey would require all-sky coverage. For a comparable survey of dwarf satellites around M31 alone, imaging of over 800 square degrees would be required, including observations within the zone of obscuration. The scale on which dwarfs cluster around parent galaxies is found to depend on the mass of the parent halo according to the relation $r_{2t} = 193(M_{12})^{1/3}$ kpc (Trentham et al. 2006) where M_{12} is the mass of the halo in units of $10^{12} M_\odot$ and r_{2t} is the second turnaround radius of spherical collapse, similar to the overdensity radius r_{200} . At a distance of 3.6 Mpc and halo mass of $1.6 \times 10^{12} M_\odot$ (Karachentsev et al. 2002a), M81 has a second turnaround radius of 230 kpc, or only 3.6 degrees. A survey of this group with complete areal coverage is therefore made possible with large format CCD detectors such as the square degree MegaCam detector mounted

on the 3.6m Canada-France-Hawaii Telescope. In addition, the M81 Group is interesting in its own right as a rich group with a large late-type dwarf galaxy population, unlike our own well studied dSph-rich Local Group.

MegaCam is a wide field camera composed of a mosaic of 36 CCDs that cover a total area of 0.96×0.94 deg with chip gaps 13 and 80 arcsec wide. Each CCD is composed of 2048×4612 pixels of $0.187''$. We imaged a 65 square degree region centered around M81 in a raster pattern that resulted in each location being observed twice for a total integration time of 1096s. The survey was conducted entirely in the r' -band because we were primarily interested in the resolved giant population. Typical seeing was 0.75 arcsec, but ranged between 0.6 and 0.9 arcsec (Figure 2). Most of the data were observed on photometric nights, although a few fields were imaged through thin cirrus. Observations were carried out by CFHT staff in queue mode over 3 semesters in the period 2005B-2006.

2.2. MegaCam data processing methods

The raw images were initially processed by TERAPIX, an astronomical data reduction center located at the Institut d’Astrophysique in Paris, which provides pipeline data reduction for MegaCam. The TERAPIX pipeline first evaluates data for image quality, identifies chip defects and cosmic rays, and generates weight and flag-map images. Each image is warped onto a common astronomical projection (TAN) and coordinate system (J2000) using SWarp software and an astrometric reference catalog. SExtractor is run on all images to perform the object detection and photometry. The astrometric and photometric calibrations are determined using SCAMP. Astrometry is performed by downloading reference astrometric catalogs e.g. USNO-B1 (Monet et al. 2003). These are cross correlated with each exposure and a pattern matching algorithm is run. Final astrometric uncertainties are dominated by errors in the reference catalogs. On large scales, the astrometric accuracy is expected to be better than ~ 0.3 arcsec. Photometric calibration uses standard stars observed on photometric nights. The weighted, quadratic sum of SExtractor parameter MAG_AUTO differences from overlapping detections is used to put all fields onto a common zero-point scale. Residuals for bright objects are typically less than 0.05 magnitudes rms with even smaller zero-point uncertainties. These raw and processed MegaCam survey data are available online through the Canadian Astronomy Data Centre.

Our fields were mosaicked in such a way that every region was imaged twice with some additional overlap along the sides of each field. These pairs of 548 sec images had still to be stacked. Because MegaCam images are huge, we first split each image and its associated mask image into quadrants. The mask image contained flagged chip defects such as bad columns and pixels as well as cosmic rays. Images were combined using IRAF tasks for image registration and image combination. Pixels that were flagged in each image were ignored during the average operation. Two to four individual images were used to produce final stacked quadrant images of size 30×30 arcmin.

SExtractor was subsequently re-run on these combined images. Weight images were created during the stacking step with the weight of each pixel set to the square of the

number of image pixels averaged together for the final pixel value. This weight image was used during the SExtractor detection of objects to put a significantly lower weight on those regions such as chip gaps where data came from only a single image as opposed to at least two images as is the case over the majority of the field. This prevented SExtractor from detecting excess noise in these regions while still reaching to ~ 0.75 magnitudes brighter than full exposure limits. SExtractor parameters were tuned to go deep enough to recover most of the mottles in the known resolved M81 Group galaxies by setting detection and deblending levels to quite low values. Object detection was set to 1σ with a minimum area of 3 contiguous pixels while the object deblending parameter NTHRESH was set to 1σ and DEBLEND_MINCONT to $5E-7$. These low detection settings have the side effect of inducing SExtractor to recover excess noise, primarily in the halos of bright stars and galaxies, and occasionally in the numerous galactic cirrus patches obscuring this part of the sky. We err on the side of picking up spurious candidates rather than losing real candidates.

We checked the reliability of the photometry by comparison with stars of known magnitudes. Perelmuter & Racine (1995) provide a catalog of B, V, R magnitudes for all objects in the vicinity of M81. We transform the R magnitudes to the SDSS r' system using the rough transformation $r' = V - 0.84(V-R) + 0.13$ provided in Fukugita et al. (1996a). The average difference in r' (Perelmuter - this work) for stars with $17 < r' < 19.5$ is 0.01 with $\sigma = 0.11$ (Figure 3). Since this is only an approximate color transformation, we take this as strong support for the reliability of the photometry.

2.3. Detection of 22 new candidate M81 companions

The tip of the red giant branch lies at $M_I = -4.05$, with $(V - I)_{tip} \sim 1.5$. For $(V - R)_{tip} \sim 0.8$ and using color transformations for metal poor population II stars from Jordi et al. (2006), we find $M_{r',tip} \sim -3.1 \pm 0.1$. With our 18 minute combined exposures, we reach limiting magnitudes for resolved stars of $r' \sim 25.0 - 25.5$. From Schlegel et al. (1998) maps, galactic reddening $A_{r'}$ in this region is typically 0.1-0.2 but as high as 0.7 magnitudes. Because the M81 Group is so nearby at a distance of only 3.6 Mpc ($\langle m - M \rangle_\odot = 27.8$), we can resolve stars down to limiting magnitudes of $M_{r'} \sim -2.9 \pm 0.5$. The radial distance within the group will also affect the limiting absolute magnitude by ± 0.15 . Thus, stars at the tip of the red giant branch are just at the edge of detection in our MegaCam images while young main sequence and red supergiant stars, and intermediate age AGB stars are well resolved.

Two different methods were used to search the MegaCam images for new M81 Group dwarf galaxy candidates. The first method used visual inspection of the images. Final images were examined by eye by two of the authors (IK and KC) for new candidates by identifying objects that had resolved and semi-resolved faint stars. Good candidates also had an associated diffuse low surface brightness (LSB) component, although this was not observed in every case. 17 new candidate M81 dwarf members were detected in this way.

The second method used to discover new candidate

dwarfs implemented a 2-point correlation auto-detection routine. The auto-detection code calculates the 2-point correlation using the natural estimator for objects having magnitudes $22 < r' < 27$ on scales of 1.1-6.4 arcsec (0.02 - 0.11 kpc at the distance of M81) and within boxes of size ~ 40 arcsec (0.7 kpc). The code is set up to use any box or scale size but we were focusing on smaller galaxies with a concentration of resolved stars. Presumably large diffuse fields of stars could be missed, although the code did pick up a number of these as well. As the box marches across the image, the correlation values within the box are summed and any region with an excess value is flagged. This value was empirically chosen to be 80 based on recovery of previously known and newly visually detected galaxies, and based on tests of the recovery of artificial galaxies (see below). The value chosen maximized the ratio of the rate of recovery of artificially added galaxies to noise detections, but does then necessarily impose minimum magnitude and concentration limits on our survey. All regions that were flagged were checked by eye. Typically 40 – 200 such regions were found in each square degree MegaCam image. The great majority turned out to be noise detections along still remaining bad columns, or an excess of noise spikes around halos of bright stars and galaxies or within cirrus. Several detections in each image proved to be distant galaxy clusters. The remainder of the detections include the M81 candidates and previously known group members.

The code recovered all previously known dwarfs and most of the ones found by eye in this paper, the 3 exceptions being d0957+70, d0944+69, and d1016+69. For these 3, too few resolved points were detected by SExtractor. It did pick out 2 dwarfs, d1009+70 and d0946+68, which have more of a diffuse LSB component than a resolved stellar population and are thus more likely to be galaxies at somewhat larger distances. We retain all 5 questionable objects in our full candidate list but although we still believe d1016+69 to be a good candidate, we consider d0957+70 to be a possible artifact and the other 3 to be potentially more distant galaxies.

The code also found a number of candidates not picked out by eye. A couple of these appear to have both stellar and diffuse LSB components: d1006+67 is the best of these candidates with a resolved stellar component contained within a diffuse low surface brightness region. d0934+70 is hidden behind cirrus but appears to have both a faint resolved stellar component and excess diffuse emission visible over the cirrus. d1048+70 appears to have a diffuse component but only a semi-resolved stellar component. If real, this may perhaps be a more distant dwarf. A couple more have an excess of faint stellar-like detections but in these cases the objects do not appear to be concentrated nor have an LSB component and may prove to be distant galaxy clusters or chance concentrations of stars. Coordinates and basic parameters for a total of 22 new candidate dwarf galaxy group members are listed in Table 1.

We display thumbnails of 3 candidate M81 Group blue compact dwarfs (BCDs) in Figure 4 along with a mosaic of another 9 good dwarf member candidates in Figure 5. Each galaxy image is 1.5 arcmin on a side. In Figures 6 - 7 we display candidates which may turn out to lie slightly in the background of the M81 Group or simply be artifacts

in the data, foreground clumps of stars, or distant galaxy clusters. Figure 8 displays a map of our 65 square degree survey region and the distribution of the new candidate sources along with previously known group member galaxies. We show a few examples of galaxy clusters detected by our 2-point correlation routine in Figure 9.

In Figure 10, we display histograms of the number counts, $N(m_R)$, of the SExtractor detections within a radius of 30 arcsec centered on each of the new M81 candidates. For the 3 BCDs and d0944+71, another bright candidate, we construct histograms for detections out to a radius of 45 arcsec. A rough estimate of the fore/background object counts is obtained by measuring the number counts in a same sized region 2.5 arcmin west of each galaxy. These are displayed as shaded histograms overlaying the candidate population histograms.

2.4. Limits of our Detection Methods

We tested our automated method of detecting dwarf candidates through the 2-point correlation of resolved stellar populations using false stars. We wish to determine to what limiting stellar densities and magnitudes our galaxy detection routines are sensitive. To simulate artificial dwarf galaxies, large numbers of stars are added to real images with the IRAF package ARTDATA and convolved with the seeing of the field. Stars were distributed according to an exponential spatial density profile with an effective radius, r_e , ranging from 4-90 arcsec (0.07-1.6 kpc). The stellar luminosity function has the form of a power law with power ~ 0.3 for the RGB (Makarov et al. 2006). This value was allowed to vary randomly between 0.25 - 0.35 in the simulations. We add between 100 stars and 120,000 stars to each galaxy realization ranging in magnitude from $r' \sim 30.0$ at the faint end to 24.7 - 25.3 at the bright end. We take the tip of the RGB magnitude as our bright limit (24.7) but include up to 0.6 magnitudes of extinction. We also include a number of simulations with a bright limit up to 22. This allows us to simulate galaxies with a range of stellar populations, from those having entirely old stellar populations to those also containing a young, bright component.

The STARLIST task was used to generate a file suitable for input to MKOBJECTS. Simulated stars were first convolved with the image seeing and Poisson noise was included before objects were added to the real images. Sets of 40 artificial galaxies were added at a time to single MegaCam quadrant images and run through our detection procedure. A total of 1900 galaxies were generated in this manner. In Figure 11, we display a few examples of our simulated galaxies. SExtractor was re-run on these images and the 2-point correlation automated method was then used to search for these artificial dwarf galaxies.

Although we expect the detectability of a galaxy to depend only on whether the dwarf galaxy has a significant resolved stellar population, we find that the detection rate and limiting depth of our survey depends on a number of factors. The primary factors are the total number of resolved stars and the concentration of these stars. These correspond to the typical measured quantities of total integrated magnitude and surface brightness of the galaxy. Results of 1200 artificial galaxy realizations generated with typical 0.64 - 0.75 arcsec seeing and with extinction values

< 0.2 are displayed in Figure 12. We plot the integrated total magnitude and half-light radius for each simulated galaxy. Open points are those objects which landed on single exposure chip gap regions of the MegaCam field, or fell on bright stars or galaxies and are less likely to be recovered. Large black diamonds represent real candidate dwarf galaxies discovered in this survey. The dashed line displays the magnitude at which recovery drops to 90% within 2-magnitude bins, while the solid line represents the 50% completeness limit. We find that we are able to detect compact galaxies with $R_e < 11$ arcsec down to $r' = 20.5$, or about $M_{r'} = -7.3$. For galaxies with $R_e < 30$ arcsec, we are able to reach $r' = 19.0$ (-8.8) with at least 50% completeness. For galaxies larger than $R_e = 30$ arcsec (~ 0.5 kpc) we are at least 50% complete to $r' = 18$ (-9.8). Assuming real dwarf galaxy sizes of $R_e < 1$ kpc, we expect our survey is 90% complete down to about $r' = 18.0$, or about -9.8 at the distance of M81.

In Figure 13, we display the survey detection limits in the $mag - \mu$ plane. Symbols are as before. Lines of constant effective radius are labeled. A curved line is drawn that best bounds the region within which simulated galaxies are recovered. This is the traditional curve that describes isophotal limits for exponential profile galaxies (Allen & Shu 1979). The completeness of this survey depends on other factors, but the recovery boundary is adequately described by isophotal limits. At a given magnitude, as one goes to fainter surface brightnesses, recovery fails because of increasingly low concentrations of stars and a failure of the eye or 2-point correlation methods to distinguish these from the background. At a given surface brightness, as one goes to fainter magnitudes, objects become smaller with decreasing stellar population sizes. Therefore, while not necessarily isophotal limits, the detection limits imposed on this survey can be translated to limiting angular sizes and surface brightness.

However, the detection efficiency will also vary by location in these fields. Because our survey just reaches the tip of the RGB, any galaxy with a pure old population is detected only at brighter magnitudes and surface brightnesses in regions of high extinction and fields with worse seeing. We test this with 240 artificial galaxies generated with 0.5 magnitudes of extinction. See Figure 14. On average, the 50% limit in the recovery is 0.3 magnitudes brighter than for the sample added with 0–0.2 magnitudes of extinction. Although the number statistics in this sample is small, this suggests that the completeness limit in magnitude depends directly on the level of extinction and that our completeness limits may vary by as much as 0.6 magnitudes throughout our survey region. Similarly, the depth of the group may affect completeness limits. Variations in the distance with respect to M81 of ± 300 kpc affect apparent magnitudes by ± 0.18 mag. This is a very small effect but implies that the dwarfs on the near side of the group with pure old populations are more likely to exhibit detectable resolved stellar populations than those on the far side.

We test the effect of poorer seeing with 400 galaxies that were simulated with 0.9 arcsec seeing. Results are presented in Figure 15. The solid line denotes the location where completeness drops to 50% with 0.9 arcsec seeing, while the dashed line represents the 50% completeness for

seeing no worse than 0.75 arcsec. We find evidence that seeing has an effect on the recovery of resolved dwarfs, and this is most significant for compact galaxies ($R_e < 20$ arcsec) where the completeness shifts 0.8 magnitudes brightward. This is to be expected. In these cases worse seeing blends the light of these small objects to produce a smooth, less resolved low surface brightness object. With the small number statistics, it is not clear that at larger R_e the 0.2 arcsec worse seeing will affect recovery by the measured 0.4 magnitudes, but the results do indicate that seeing has an effect on the detection rates of these objects. Fortunately, only ~ 19 combined images, or 11% of our survey area, will be affected by such poor seeing.

To a lesser extent, one might expect the bright cirrus patches present throughout much of this region to affect detection limits through increased sky noise. From artificial galaxy tests, however, we do not find this to significantly affect our recovery rates. Regions of high galactic stellar density can also limit detectability for the more diffuse dwarfs. At galactic latitudes ranging between 39–44 deg this is not too much of a problem, but a few fields exhibited non-uniformly distributed excess numbers of stars throughout the images, increasing the confusion level. This will primarily affect fainter, lower surface brightness dwarfs with fewer total numbers of resolved stars spread over a larger area.

Finally, two areal coverage issues will affect recovery. Any small dwarf lying behind bright saturated stars or galaxies will likely be missed. From false galaxy tests, where the galaxies are randomly placed within the images, we find less than 4% of recoverable galaxies remain undetected because they landed on bright objects. This primarily affects only the smallest galaxies which can hide entirely behind brighter foreground objects, although a few more extended simulations were obscured by bright stars or galaxies. Also, due to the survey strategy of observing each field twice by offsetting between images by half a field, all chip gap regions in the MegaCam field are observed for a total of only 10 minutes. With half the exposure time as the rest of the field, we expect the magnitude completeness limits in these regions to be about 0.75 magnitudes brighter than the above described survey limits. Because the detected dwarf galaxies in M81 have angular sizes generally greater than 16 arcsec, the vertical chips gaps of 13 arcsec should not affect recovery of any but the tiniest galaxies if by misfortune they should fall in these regions. There are however two large horizontal chip gaps which have single exposure widths of 80 arcsec each across the length of each MegaCam field, and this gap size is essentially doubled in our mosaic of two images per field. Since all our newly discovered dwarf galaxies have angular extents smaller than 160 arcsec, it is therefore entirely possible for dwarf galaxies to be lost in these regions. The total area of these single exposure regions, including the area at the top and bottom of our full mosaic, is 9.7 square degrees, or $\sim 15\%$ of the total survey area.

Based on these results, we find that we are nearly 100% complete to $r' = 17$ and 90% to $r' = 18$ ($M_{r'} = -9.8$). At fainter magnitudes, a large number of factors act to diminish our ability to detect group galaxies, although the primary factors are simply the limiting magnitude and surface brightness to which we are sensitive. Factors such as

worse seeing, higher extinction, areal coverage by brighter objects, and single exposure regions serve to push these limits to slightly brighter magnitudes.

2.5. Follow-up Spectroscopy

Follow-up spectroscopic observations were carried out with FOCAS on the 8m Subaru Telescope and SCORPIO on the Special Astrophysical Observatory 6m BTA telescope. Spectra were obtained for our three BCD candidates along with several globular clusters in a couple of previously known M81 dwarf galaxies.

Observations with Subaru were made 22-24 Nov 2006 using the R300/mm grating in second order and VPH 600-450 grating in first order. A two arcsec slit was used with the VPH grating, and images were binned 4×2 , providing a spectral resolution of 10\AA at 4000\AA . For the R300 grating, a 1 arcsec slit and 4×1 binning was used to obtain a spectral resolution of 10\AA . Spectral coverage ranged from $3800 - 5250\text{\AA}$ for the VPH and $3650 - 5950\text{\AA}$ for the R300 grating. Exposure times varied from object to object.

Longslit spectra were obtained with FOCAS of globular clusters in the previously known faint dwarf galaxies F8D1 and IKN. The globular cluster in F8D1 was originally noted by Caldwell et al. (1998). For two bright candidate galaxies (both BCDs) d1028+70 and d0958+66, we obtained spectra by simply placing the slit across the long axis of the galaxy. These data were processed using standard IRAF routines. Images were first cosmic ray corrected using CRMEDIAN and then bias subtracted using 10 median combined bias frames. Arcs were observed before or after each observation and used to wavelength calibrate the spectra. Lines in the arcs were identified using IDENTIFY and REIDENTIFY, and FITCOORD was used to obtain a dispersion correction solution which was applied using TRANSFORM. The two-dimensional spectrum for each object in the slit was extracted using APALL. Finally, RVSAO/XCSAO (Kurtz & Mink 1998) was used to obtain a cross correlation solution from template spectra for the redshift of each object and hence the galaxy itself. Spectra are displayed in Figure 16. Radial velocities are listed in Table 2.

Further observations were performed for the 3 BCD candidates with SCORPIO in long-slit mode installed at the BTA 6-meter telescope prime focus. The grism VPHG400 was used with a 1 arcsec slit yielding the spectral range $\sim 3500 - 7500\text{\AA}$ chosen to include $H\alpha$ with a resolution of $3\text{\AA}/\text{pixel}$ and FWHM $\sim 20\text{\AA}/\text{pixel}$. The objects d1028+70 and d0958+66 were observed during the night 11 November 2006 with the exposure time of 600 sec under $2''$ seeing. The galaxy UGC 5497 (d1012+64) was observed on 20 October 2007 with an exposure time of 900 sec under $2.5''$ seeing. Spectrophotometric standard stars were also observed for calibration. The standard pipeline with the use of MIDAS, as described in Afanasiev & Moiseev (2005), was applied for the reduction of these long-slit spectra. All three BCD candidates show knotty $H\alpha$ emission. We display the spectra in Figures 17 - 19. Due to the short exposure times and low S/N it is difficult to measure line ratios. However, we note that the [NII] $\lambda 6584$ line is quite weak in comparison to $H\alpha$, especially for d0958+66. We estimate an upper limit for the line ratio of 0.05 for this galaxy. From the relations of Kewley & Dopita (2002) and

Pettini & Pagel (2004), this leads to an upper limit for the metallicity of $0.3 Z_{\odot}$. Mean heliocentric radial velocities of the objects are included in Table 2.

2.6. Multi-band Imaging Follow-up

Using the UH 2.2m with Tek 2K CCD on 19-24 Dec 2006, we imaged 9 of the dwarf galaxy candidates in V and I -bands. Seeing ranged from $0.7 - 1.4$ arcsec and 5 nights were photometric. Images were 4×900 s in the V -band and 5×720 s in the I -band. Standard stars were observed on each photometric night. Images were processed using standard IRAF routines. Due to the slow speed of the mechanical shutter, a shutter mapping correction was also implemented. This was necessary for the short exposure images (5-20s) of the standard stars.

In most cases, the images did not go deep enough to produce useful color-magnitude diagrams (CMD). For 8 galaxies observed on photometric nights, we measure integrated $V - I$ colors within circular apertures out to the effective radius as measured in the r' band (Section 3.1). We correct for extinction using the maps of Schlegel et al. (1998). $V - I$ colors are listed in Table 3. We also generate color images of the 9 candidates. To create images for the blue channel we take $2 * V_{image} - I_{image}$. The V and I -band images are taken to be green and red respectively. Color images are displayed in Figure 20.

Large young, blue stellar populations are evident in d0926+70, d0958+66, d0959+68, and d1028+70. These are objects classified by us as BCDs, dIs, and tidal dwarfs. These multi-band data may not be going deep enough to reach the tip of the red giant branch. While resolved stars are seen in the MegaCam survey images, the lack of visible resolved stars in the UH 2.2m images of d0955+70 suggests it may consist predominantly of an older stellar population. Similarly, if members of the M81 Group, d0934+70 and d1006+67 also appear to contain predominantly older stellar populations.

We have recently obtained HST/WFPC2 multiband imaging for 14 of the candidates and have been awarded time to complete observations of the sample with HST/ACS. These data will be deep enough to measure distances from the CMD tip of the red giant branch. Results will be presented in a subsequent paper.

3. RESULTS

3.1. Properties of the M81 companion candidates

To determine centroids of the new objects, we used the intensity weighted means of pixel values, $\frac{\sum \bar{x}I}{\sum I}$, around each galaxy. Ellipticity and position angle around these centroids were then derived from the intensity weighted second moments (Secker & Harris 1997). The measured ellipticities, $(1 - b/a)$, for the faintest objects are highly uncertain due to low S/N of the diffuse light component and small visible stellar populations. Measuring total magnitudes for these very faint and diffuse extended resolved galaxies is challenging because of expected contamination from foreground stars, and in several cases, from excess foreground cirrus reflected flux, not to mention extinction. We therefore estimated total magnitudes using several methods.

We first mask all obvious bright foreground stars and

background galaxies around each of our candidates. Simple aperture magnitudes were obtained for each galaxy with radii 50, 100, 150, or 200 pixels (9.35, 18.7, 28.05, and 37.4 arcsec) depending on the visible extent of the galaxy. The sky was determined in an annulus 4 pixels wide with a radius of 400 pixels. Alternatively, we measure total flux in an identical sized aperture in 4-5 regions around each galaxy. Taking the average of these as an estimate for the contribution from both sky and foreground/background object flux we subtract this from our object flux for a second estimate of total magnitude.

To obtain structural parameter measurements for each galaxy, we extracted fluxes in successive elliptical apertures around each galaxy out to a radius of 40 arcsec and truncated the data if it exhibited a $> 30\%$ increase in slope attributed to contamination by an unmasked neighboring object, or, more often, to features like bright cirrus bands. The central 4 arcsec were also discarded. We then fit both the surface brightness profile with a Sersic function and the curve of growth with a cumulative Sersic function. We extracted parameters from the best of these two fits. This provides a third estimate of the total magnitude along with central surface brightness, effective surface brightness, and half-light radius. The generalized Sersic function is defined as

$$I(r) = I_o e^{-(r/r_o)^{1/n}} \quad (1)$$

where n is the Sersic parameter. For $n = 1$, this reduces to an exponential profile which usually provides a good fit for disk and dwarf galaxies, and for $n = 4.0$ becomes a de Vaucouleurs profile. The cumulative Sersic function is then

$$I(r) = 2\pi\sigma_o r_o^2 n \cdot \gamma[2n, (r/r_o)^{1/n}] \quad (2)$$

where $\gamma[a,x]$ is the Incomplete Gamma function,

$$\int_0^x \exp(-t)t^{a-1} dt. \quad (3)$$

This can be integrated to obtain the total object flux,

$$I_t = 2\pi\sigma_o r_o^2 n \Gamma[2n] \quad (4)$$

with total magnitude,

$$m_t = \mu_o - 5 \log(r_o) - 2.5 \log(n\Gamma[2n]) - 2.0 \quad (5)$$

(Binggeli & Jerjen 1998) where $\Gamma[a]$ is the Gamma function.

The fitting of this nonlinear function to the data was done using a Levenberg-Marquard algorithm (Press et al. 1992) which performs a χ^2 minimization that implements an inverse-Hessian method far from the minimum and switches to a steepest decent method as the minimum is approached. In Figures 21 - 26, we display both curve of growth and surface brightness profile fits for our candidate galaxies. From these fits we directly obtained the central surface brightness, scale length, and profile type, where scale length in the generalized Sersic function is directly related to the half-light or effective radius through

$$R_o^{1/n} = R_e^{1/n} / (2.3026b_n) \quad (6)$$

with $b_n = 0.868 - n - 0.142$ (Caon et al. 1993).

The majority of the galaxies are best fit with Sersic index $n < 1.0$. From inspection of the plots it is clear that these low n fits are primarily driven by large cores, typical of dwarf galaxies. In the outer radii, the surface brightness profile tends to drop exponentially. We overlay best fit exponential profiles to the outer radii in the surface brightness profiles of Figures 21 - 26. A number of cases exhibit a sharper drop-off, but are still consistent with an exponential fall-off within the large uncertainties of the low surface brightnesses at these radii.

We estimate typical magnitude measurement errors of 0.5. Sources of uncertainty come from sky determination (0.4, estimated from curve of growth fitting when using 3 different estimates of sky values), foreground/background contamination (typically 0.2, from magnitudes measured with and without masking of likely foreground sources), aperture magnitude measurement error from qphot (0.04), and the zeropoint uncertainty (0.015, estimated from comparison with Perelmuter & Racine (1995) catalog stars). Cirrus may also effect measurements of some of the galaxies. Sky estimates in these regions have an even larger uncertainty, and faint old stellar populations may be lost in the excess sky noise. In particular, d0934+70, if real, appears largely obscured by cirrus. d0944+71, d0959+68, and d1048+70 are strongly effected by fore or background objects. We estimate total magnitude uncertainties of 0.8 for d0958+68 and 0.6 for d1048+70. The magnitude for d0944+71 is corrected by assuming a symmetric shape. Flux from the star superposed quadrant is replaced by the flux in the symmetrically opposite quadrant. We assume a magnitude uncertainty of 0.8. Candidate d1019+69 is affected by missing data in a chip gap; the measured magnitude is corrected in a similar way as d0944+71.

We estimate measurement errors in R_e by comparing results from the surface brightness profile and curve of growth fits and comparing differences from fits using slightly different estimates for the mean sky value. We find fractional uncertainties in R_e range from 1% for the bright BCD d1028+70 to 40% for low surface brightness object d0955+70, with a median uncertainty of 10%. Similarly, we find an uncertainty in the central surface brightness ranging from 0.05 to 0.5 magnitudes arcsec $^{-2}$ with a median uncertainty of 0.2.

Because of the shallow nature of our survey, we can assume that our magnitude and size measurements are lower limits. To obtain estimates of total magnitudes, all measured magnitudes had to be corrected for light lost in the sky noise. Since many of the profile fits were influenced by the bright O/B stars, it is possible that measured profiles do not accurately reflect that of the underlying old stellar populations. We therefore calculate the missing fraction of light assuming both the fitted profile shape and an exponential surface brightness profile. Dwarf galaxies may be better fit with King profiles than exponential due to the presence of large cores and possible truncation in the wings of the profile. This is supported by our generalized Sersic function profile fits which find $n < 1.0$ for most of our galaxies, implying a steeper fall off of the galaxy light in the wings of the profile. Magnitude corrections calculated by assuming exponential profiles may therefore be overestimates for these galaxies, and thus provide upper limits on the total galaxy luminosities.

From an isophotal limiting surface brightness (ranging from 27.0 to 28.5 depending on the sky level and presence of cirrus), along with the measured central surface brightness and total magnitudes, we extrapolate to obtain the intrinsic total magnitude. Over x scale lengths, $x = r/r_o$, the surface brightness of an exponential profile drops by

$$-2.5 \log e^{-x^{1/n}} = 1.086x \quad (7)$$

for $n = 1$ or

$$= 1.086x^{1/n} \quad (8)$$

for a generalized Sersic profile. The number of scale lengths observed between μ_o and μ_{lim} is

$$\Delta x = (\mu_{lim} - \mu_o)/1.086 \quad (9)$$

or

$$\Delta x = ((\mu_{lim} - \mu_o)/1.086)^n. \quad (10)$$

For $m_T - m_{lim} = m_{extrap}$ with

$$m_i \propto 2.5 \log[(1+x)e^{-x}] \quad (\text{exponential}) \quad (11)$$

and

$$m_i \propto 2.5 \log\left[\int_0^{r_i} e^{-x^{1/n}} r dr\right] \quad (\text{Sersic}), \quad (12)$$

we find the extrapolation beyond the measured magnitudes is

$$\Delta m = 2.5 \log[1 - (1 + \Delta x)e^{-\Delta x}] \quad (13)$$

and

$$\Delta m = 2.5 \log[\gamma[2n, \Delta x^{1/n}]/\Gamma[2n]] \quad (14)$$

for exponential and generalized Sersic profiles respectively. See also Tully et al. (1996). Exponential profile corrections from the isophotal magnitude are less than -0.1 mag for our brightest new candidates, but as high as -1.2 mag for the faintest objects with a mean value of -0.4 . Corrections for the best fit Sersic profiles range from 0. to -0.8 magnitudes with a mean of -0.2 . Besides assuming a profile shape, these corrections further assume an old stellar population exists which may be too faint to detect, even as a diffuse low surface brightness component, in some cases. For potential tidal dwarfs like d0959+68, it is not clear that this assumption is valid. There may be evidence that d0959+68 is dominated by a very young population formed less than 70 Myr ago (Durrell et al. 2004). We therefore do not apply a correction for this object.

We provide the detailed structural and photometric properties of these new objects in Table 3. If we assume all candidates are group members at the distance of M81, we find $M_{r'}$ magnitudes range from -6.7 for d0944+69 to -13.3 for d1012+64. Half-light radii range from 90 to 490 pc for objects well fit with Sersic functions. Because we do not yet have distances to these galaxies, we estimate that intrinsic magnitudes and radii can vary by as much as 0.14 mag and 6% in size (assuming a distance range of $\pm r_{2t}$). We provide r' total magnitudes of previously known M81 Group members that lie within our survey region in Table 4. For the largest galaxies, we expect larger magnitude measurement errors, up to 1 mag, due to large errors in the local sky determination and subsequent negative features in the images. For measuring the local sky backgrounds, the TERAPIX reduction pipeline implements box sizes much smaller than the size of our largest galaxies.

3.2. M81 Group Luminosity Function

To construct the M81 Group differential luminosity function (LF), we bin number counts as a function of magnitude in 2-magnitude bins. Such large bin sizes are necessary because of the small number counts we are working with and because of large magnitude measurement errors (> 0.5 mag). Counts are normalized by the size of our survey region. We construct luminosity functions for all previously known members, all previously known plus all new candidates from this work, and for previously known plus best candidates from this work. In the case of 'best', we include objects in Figures 4-5. We have excluded counts for objects we believe may be background or which could potentially prove to be artifacts. Of the previously known objects, we also exclude from this 'best' sample Arp's loop and Garland since we do not have reliable magnitude estimates for these likely tidal objects. The luminosity functions for these different samples are displayed in Figure 27. We have constructed the LFs using measured magnitudes (top), exponential profile corrected total magnitudes (middle), and Sersic profile corrected total magnitudes (bottom).

Based on our artificial galaxy tests, we shade the region where incompleteness sets in. Brighter than $r' = 17$, we expect we are 100% complete, and to $r' = 18$, to be at least 90% complete. We may still be missing a small number of dwarfs which are lurking behind bright stars or other galaxies, but find this should be less than a 4% effect, primarily affecting only the smallest objects. We use our simulations to determine estimates for our completeness at each magnitude bin in the LF. The lower limits in the detection efficiency imply that, at least in regions with good seeing and low extinction, we should recover all artificial galaxies down to $r' = 17$. At magnitudes brighter than this, we find no candidate dwarf galaxies with effective radii greater than 30 arcsec. Fainter galaxies will presumably be smaller. As a conservative estimate, we assume a maximum R_e of 35 arcsec and uniform distribution in R_e and calculate the fraction of galaxies we would expect to recover in each 2-magnitude bin of our luminosity function. In reality, we expect galaxies to be weighted towards smaller sizes at fainter magnitudes. The assumption of a uniform distribution should therefore provide us with an upper limit for the fraction of the real population we would expect to have missed, and an upper limit for corrected counts. Results are plotted in Figure 28. The solid line is a fit to the recovery results of simulations with good seeing, low extinction, and falling on full integration regions. The dashed line incorporates the 15% of the survey with single exposures and takes into account any lower completeness due to worse seeing and extinction in each field. We apply these fractions as completeness corrections to the counts in our luminosity function (open circles in Figure 27). Applied corrections also include a 3% correction for areal coverage by brighter objects for $r' \geq 17.0$. Although these are only crude corrections since we do not know the true distribution of M81 Group galaxy sizes faintward of our 100% completeness limits, we do not find any evidence suggesting the faint-end slope steepens beyond what we measure from our observed galaxy counts.

The luminosity distribution of galaxies is traditionally modeled by a Schechter (1976) function or with a simple

power law for the faint end only. To measure the faint-end slope of the magnitude distribution, we perform a power law fit to the complete set of galaxy counts between $8 < r' < 18$ and find a faint-end slope, α , ranging from $-1.26_{-0.08}^{+0.09}$ for the case of measured magnitudes to a maximum of $-1.39_{-0.05}^{+0.05}$ for exponential profile corrected total magnitudes. The slope for the full, completeness corrected sample ranges from $-1.28_{-0.05}^{+0.04}$ to $-1.32_{-0.05}^{+0.04}$. We measure a slightly shallower faint-end slope for only previously known group members of $-1.19_{-0.07}^{+0.07}$ to $-1.26_{-0.08}^{+0.08}$. However, it is clear from the figures that the slope does not increase much with the addition of these new candidate dwarf group members; only the completeness has shifted to fainter limiting magnitudes. Completeness corrected counts as a function of both measured and Sersic corrected magnitudes are well described by $\alpha = -1.3$ slopes. It is possible that our luminosity functions display an upturn at the faint-end, at magnitudes $r' > -15$. We therefore also fit all counts at the faint-end in the range $-15 \leq r' < -10$ where we expect to be nearly complete. This provides us with the steepest slopes consistent with our data, with $\alpha \sim -1.45$. However, we caution that this measurement is based on few counts and low number statistics. Best fit values for the faint-end slope, α , for all samples are listed in Table 5.

Due to the overall small number counts of group galaxies, uncertainties in each bin of our differential luminosity function are large. This has the effect of producing a number count distribution that does not monotonically rise as a function of magnitude and, with so few data points, is not well fit with a power law. We therefore also produce a plot of the unbinned cumulative distribution of galaxy counts as a function of measured and corrected total magnitude for all subsamples in Figure 29. We fit a cumulative Schechter function to the cumulative counts,

$$\int \Phi(M) dM = 0.4 \ln 10 \phi_* \int 10^{0.4(\alpha+1)(M_*-M)} e^{-10^{0.4(M_*-M)}} dM \quad (15)$$

such that

$$N(< M) = \phi_* \gamma [\alpha + 1, 10^{0.4(M_*-M)}] \quad (16)$$

using maximum likelihood techniques with a Poisson estimator. M_* is not only not well constrained due to the very small number of objects at the bright end of the LF, but is also affected by large errors in measured magnitude for the the brightest galaxies. For M81, we know our measured total magnitude is strongly affected by improper sky subtraction. For the luminosity function we therefore assume a total magnitude for this galaxy, $M_{r'} = -21.8$, from previously obtained R band data (Tully & Pierce 2000). For fitting the cumulative Schechter function to our data, we hold M_* and ϕ_* constant while solving for the best fit slope, α . Results for the different samples are presented in Table 6. To test the effect of M_* on the fit, we re-fit the data allowing all parameters to vary. We find the slope changes typically by about 0.015, and no more than 0.04, smaller than the random errors in our fitted slope values. Results are similar when we use our original total magnitude measurement for M81. Therefore, the value of M_* , although coupled to α , does not significantly affect the determination of the faint-end slope. In Figure 30, we display the 1σ $\alpha - M_*$ error ellipses for the luminosity

functions of 'best' and 'all' candidate samples with Sersic corrected magnitudes. It can be seen that M_* is unconstrained at the bright end, but the choice of M_* will not strongly effect the value of α .

Overall, we obtain very similar values for the faint-end slope as compared with the power law fit to the faint end of the differential LF. For all samples, we find a faint-end slope $\alpha \sim -1.28$. Slopes for only originally known and 'best' candidates are insignificantly shallower than for all candidates. We furthermore find the faint-end slope to be robust against corrections from measured to total magnitude.

Fits to completeness corrected counts do not produce steeper faint-end slopes, but do extend our fits to all counts down to $r' \sim -7$. Since we expect these completeness corrections are already an upper limit given the expected true size distribution of real galaxies, we do not believe the slope steepens appreciably at magnitudes fainter than our completeness limit. The steepest measured slopes are for the full sample of objects which assume all candidate objects we have detected are real galaxies within the M81 Group. Certainly some subset of these candidates are not true M81 Group galaxies, so we can take these slopes as an upper limit. We find the best fit slope for the subsample of most likely M81 members using Sersic profile corrected magnitudes to be -1.30 ± 0.10 and -1.26 ± 0.05 for the differential and integrated LFs respectively.

4. DISCUSSION

4.1. Dwarf Population Characteristics

Of the new candidate galaxies, roughly 45% are believed to belong to the dwarf spheroidal class with dominant old stellar populations, while the rest exhibit dwarf irregular or BCD morphology with younger stellar populations and ongoing/recent star formation. At least one new object may be a tidal dwarf, formed in the tidal streams connecting the three closely interacting galaxies of M81, M82, and NGC 3077. This area contains a number of knots of star formation and tidal debris. Previously known or suspected tidal objects include Arp's loop knots, Garland knots, Ho IX, and BK3N (Makarova et al. 2002). These objects are found to be dominated by young stellar populations and have high gas contents (de Mello et al. 2008; Sabbi et al. 2008). Davidge (2008) recently found an arc of stars in the M82 halo which may have formed around the same time as these other tidal features. One of our candidate objects, d0959+68, was first noted by Durrell et al. (2004) in a search for intragroup stars in the field of the M81-NGC 3077 HI tidal tail. It has recently undergone a burst of star formation as evidenced by the large population of bright blue stars seen in Figure 20. Durrell et al. (2004) match isochrones to the CMD of this object and find evidence that star formation occurred 30-70 Myr ago, after the formation of the HI tidal arm. In a search for HI clouds in the M81 Group, Brinks et al. (2007) find a number of free floating clouds without optical counterparts which they suggest may be tidal debris from the 3-body interaction involving M81, M82, and NGC 3007. One of these clouds is just offset from d0959+68, about $1'.5$ arcmin to the SW, several times the measured optical half-light radius. This HI cloudlet has a radial velocity distinct from both the Milky Way and M81 tidal arm. If it turns out the

optical component has a similar radial velocity as the HI cloud, it would be likely that the two were associated. It may be possible that, like the Local Group Phoenix dwarf (Young et al. 2007), blow out from supernovae energetics from this young stellar population has displaced the neutral hydrogen gas. We display this new object along with previously suspected tidal dwarf galaxies superimposed on the HI map of Yun et al. (1994) in Figure 31.

Three new M81 candidate member galaxies (d1028+70, d0958+66, d1012+64) are of the poorly understood blue compact dwarf class. Spectra of these galaxies were obtained with Subaru/FOCAS and BTA/SCORPIO. Radial velocities of $\sim +60$, -100 , and $+150$ km s $^{-1}$ support group membership for d0958+66, d1028+70 and d1012+64 respectively. All spectra exhibit strong Balmer absorption lines indicative of recent star formation. The BTA 6m spectra also find H α emission in all three cases indicating active star formation, in agreement with the blue $(V - I) \sim 0.8$ colors found for these galaxies. These three candidates bring the total number of M81 Group BCDs to at least four, including UGC 6456, long considered an isolated member of the M81 Group (Lynds et al. 1998; Tully et al. 1981). DDO 82 may have a BCD component as well. It has an optical structure and color that corresponds to that of BCDs but has an HI flux contaminated by local HI. UGC 6456 lies far outside our survey region, at SGL = 37° , SGB = $+11^\circ$ in Figure 1, while DDO 82 lies at the projected distance of the second turnaround radius for the M81 Group. BCDs tend to be found more frequently in field environments than clusters and are one of the least clustered galaxy types known (van Zee et al. 2001). The three BCDs discovered here all lie in low density regions at a minimum projected distance of 140 kpc from M81, with d1012+64 lying outside of the second turnaround radius at a projected distance of 315 kpc. The excess of this type of galaxy observed in this group may indicate that the termination of star formation is due to processes such as ram pressure stripping which occur preferentially in more massive and more dynamically evolved groups/clusters. However, given the projected distances of the M81 BCD population, it is possible that these galaxies are on first infall orbits and processes such as strangulation that serve to shut down star formation even in poor groups (Kawata & Mulchaey 2008) have yet to act on these galaxies.

We find no ultra-compact dwarfs (UCDs) such as those found in the richer Fornax and Virgo clusters (Drinkwater et al. 2000, 2003). Neither have UCDs been discovered in the Local Group. This may support the hypothesis that UCD formation is driven by a mechanism that occurs preferentially in denser environments, such as tidal stripping of nucleated dwarf ellipticals (Bekki et al. 2001a) or late-type spirals (Moore et al. 1998). Alternatively, Fellhauer & Kroupa (2002) suggest the possible formation of UCDs as objects evolved from young massive star clusters which are formed within tidal tails of massive galaxy-galaxy mergers. In this scenario, one might expect the formation of such objects to be ongoing in the tidal tails of the galaxy interactions occurring in the M81 Group although we find no evidence for this. It is possible that we would be unable to detect the more compact UCDs in this survey using our current search techniques. We show in Figure 13 the location in $r' - \mu_e$ space the UCDs would occupy. Our

detection limit would enclose only the brighter and larger UCDs. Due to the extremely compact nature of UCDs, it is probable that the smaller ones would not appear in our images as resolved concentrations of stars. Rather, the light on these small scales would be blended making detection based on a resolved stellar population difficult and in some cases impossible. However, we would expect to be able to detect the larger and brighter subpopulation. As we do not detect a single UCD, this suggests that UCDs may be absent in this poor, unevolved environment.

No new bright ($r' < -12$) ultra-diffuse dwarfs like F8D1 and IKN have been found in this survey. This could partially be due to selection effects since neither our eye nor the two-point correlation code would be particularly sensitive to extremely diffuse objects, although these two objects were easily picked out both by eye and recovered with the two-point correlation technique. We would therefore expect to detect similarly low density objects if they existed. We do find a number of very diffuse, faint, and small candidates including d1013+68, d1014+68, and d1016+69 which may or may not prove to be real objects.

In comparison with the Local Group, we find a very different morphological mix of dwarf satellites. In the M81 Group, we have found 3 new BCD candidates while no such objects have been discovered around M31 or the Milky Way. The fraction of late type, dwarf irregulars is also much higher in the M81 Group. Including the recent detections of ultra-faint dwarfs in the Local Group, the fraction of late types is $\sim 25\%$ while in the M81 Group, including our new best candidates, the fraction of late types could be as high as 55% . This different morphological mix had been noted earlier for giant galaxies and brighter dwarfs, but recently discovered faint dwarfs in both groups maintain the distinctly different population fractions. It is inferred that the M81 Group is dynamically less evolved than the Local Group.

We do not find any objects as faint as the recently discovered ultra-faint Local Group galaxies. This is due to incompleteness at these low magnitudes. We do find one candidate, d0944+69, with an absolute r' magnitude of -6.7 ± 0.5 . This would make it the faintest known M81 Group dwarf. It also would have one of the smallest sizes for known dwarfs of $R_e = 90$ pc, similar in size to some of the recent Local Group satellite discoveries with R_e ranging from 23 - 125 pc (Willman et al. 2005; Zucker et al. 2006; Martin et al. 2006; Belokurov et al. 2007a; Walsh et al. 2007). We do not yet know if this object is either a real galaxy or a member of the M81 Group. If this object does turn out to be a group member, its lower limit half-light radius would impinge on the $40 < R_e < 100$ pc 'size gap' between dwarfs and globular clusters (Belokurov et al. 2007a). However, as most of the galaxy light likely falls below the level of the sky, we are certainly underestimating its physical size and perhaps, even with the magnitude correction, total luminosity.

The other candidates all have properties consistent with normal faint dwarfs. We plot $M_{r'}$ vs log (half-light radius) in Figure 32. New candidates are shown as filled circles (assuming a distance modulus of 27.8) while previously known group members are displayed as filled squares. The three candidate BCDs are distinguished by their high surface brightnesses. For comparison, we include Local Group

dwarfs in this plot. Recent discoveries are denoted by open circles while previously known galaxies are shown as open squares. To transform from V to r' magnitudes, we use $r' = V - 0.84(V - R) + 0.13$ (Fukugita et al. 1996b) assuming an approximate $(V - R)$ color of 0.6 for dwarf galaxies. Lines of constant surface brightness are shown. New Local Group detections only became possible with the SDSS survey reaching effective surface brightnesses below $27.0 \text{ mag}_V \text{ arcsec}^{-2}$ (Belokurov et al. 2007b), corresponding to a stellar surface density limit. Incompleteness in our survey may be starting to set in by $26.0 \text{ mag}_{r'} \text{ arcsec}^{-2}$ and most of our detections are brighter than $27.0 \text{ mag}_{r'} \text{ arcsec}^{-2}$, so we may still be missing a large population of ultra-faint dwarfs. According to Figures 13 and 32, we would expect these missing galaxies to have total magnitudes fainter than $M_{r'} \sim -8$.

4.2. Distribution of M81 Galaxies

The asymmetric distribution of dSphs noted by Karachentsev et al. (2000) has become less pronounced with the addition of the new objects. As discussed in that paper, a possible cause for the asymmetry is contamination of the M81 Group area with many reflecting nebulae (galactic cirrus) which made it difficult to find extreme LSB dwarfs that are unresolved into stars or have only old stellar populations. In Figure 33 we show the M81 region of the sky in the Schlegel et al. (1998) galactic dust map. Superimposed are the locations of galaxies in the group. A number of new candidates (diamonds) can be seen to lie in regions of higher extinction and, given the dearth of detections in regions with the highest extinction, it is possible we are still missing faint M81 dwarfs concealed by these clouds. However, it seems unlikely we would be missing dwarfs of comparable brightness to the ones displaying the noted asymmetry, given that the new candidates from this survey which are detected in regions of high extinction are all 1-2 mags fainter.

We compare the projected distribution of morphological types in Figure 34. Late types, early types, and tidal candidates are distinguished by symbol types while point sizes indicate surface brightness with brighter surface brightnesses denoted by larger points. All the bright giant galaxies are late types (circles) and all candidate tidal dwarfs (squares) lie near the center of the cluster right around M81, M82, and NGC 3077. Early type dwarf spheroidals (hexagons) lie primarily towards the group core while all late type dwarfs lie towards the periphery of the group. A clear morphology-density relation is seen. We find the median distance from M81 for late type dwarfs is 1.7 times that for dwarf spheroidals.

4.3. Faint-end of the Group Environment Luminosity Function

Λ CDM models predict a faint-end slope for the mass function of -1.8 (Trentham & Tully 2002). We measure a luminosity function faint-end slope, $\alpha \sim -1.28 \pm 0.06$ for M81 group galaxies. The steepest faint-end slopes consistent with our data are found to be -1.39 ± 0.05 for our binned differential LF, constructed with all candidates and having presumably overestimated magnitude corrections under the assumption of exponential profiles, and -1.45 ± 0.06 when fitting a possible faint-end upturn

observed in the full sample. Even when we apply completeness corrections at faint magnitudes, we find faint-end slopes flatter than -1.30 . When we include only most likely member candidates in our LF, we find a slightly shallower slope of -1.27 ± 0.06 . We therefore expect -1.30 to be an upper limit.

We compare the M81 Group LF with that of other nearby groups. Detections of dwarf galaxies in the Local Group go much fainter than we recover in M81. However, because of the full sky coverage necessary to obtain a complete census, completeness is still quite low. We therefore look only at the LF for Andromeda and its satellites. Large areal coverage is still required, including probing into the zone of obscuration, but progress is being made. We construct a cumulative LF for Andromeda satellites including all previously known galaxies (van den Bergh 2006) and recent family additions (Ibata et al. 2007; Majewski et al. 2007; Martin et al. 2006; Irwin et al. 2008; McConnachie et al. 2008) (Figure 35). A fit to the cumulative V band counts finds a shallow faint-end slope of $-1.13_{-0.06}^{+0.06}$. This is very similar to the best Schechter function fit for Local Group galaxies found by Pritchet & van den Bergh (1999) with $\alpha = -1.1 \pm 0.1$. The recent discoveries of Local Group dwarfs have not increased the slope significantly.

The nearby Cen A group at 3.6 Mpc, in contrast to the spiral dominant Local Group and M81 Groups, contains a dominant giant elliptical galaxy with radio loud AGN and a late type fraction of only $\sim 38\%$. Using B band magnitudes for the Cen A group from Karachentsev et al. (2002b), we find a faint-end slope $\alpha = -1.23_{-0.10}^{+0.04}$, nearly as steep as that of M81 (Figure 35).

Boyce et al. (2001) find that steep LFs are generated by the combined number counts of dI and dE galaxies, and when dIs are excluded from the construction of the LF, the faint-end slope flattens. This might imply that more evolved regions with fewer late types should have shallower slopes. Alternatively, from a comparison of poor groups, clusters, and field environments, Zabludoff & Mulchaey (2000) found that the dwarf-to-giant ratio (and therefore the faint end of the LF) increased in regions of higher density, and that this increase was specifically due to an increase in the fraction of quiescent dwarfs. In our work on M81 we find a steeper slope in the dynamically unevolved, dI-rich M81 Group than these other two groups and in particular the dSph-rich Local Group. However, recent work on the luminosity function for two nearby dynamically evolved groups with large early type galaxy populations finds steep faint-end slopes with values of -1.3 ± 0.1 for the NGC 5846 group (Mahdavi et al. 2005) and -1.35 for the NGC 1407 group (Trentham et al. 2006), slightly steeper than what we find for M81. These works determine group membership on the basis of morphology and surface brightness and both reach down to $M_R = -12$.

It is possible that the shallower Local Group LF is due in part to incompleteness in the surveyed region. In recent work, Koposov et al. (2007) construct the LF for the Local Group including the recent discoveries of ultra-faint dwarfs with SDSS. They also include a volume correction factor, assuming different number density laws for the distribution of halo satellites, and find faint-end slopes ranging between $-1.29 < \alpha < -1.25$ for the magnitude range $-19 < M_V < -3$, very similar to the slope we find for

M81. In this case, with all groups discussed here having faint end slopes of $\alpha \sim -1.3$, we find no clear trend in faint end slope as a function of environment within groups of galaxies.

A few recent studies have found steep faint-end slopes in group environments. Using a statistical subtraction of the background for nearby groups and poor clusters identified in SDSS data, González et al. (2006) find a sharp upturn in composite LFs at $M_r \sim -17$ with slopes of $-1.9 < \alpha < -1.6$. They find this upturn regardless of group mass, number of members, or environment. Using colors and morphology to establish membership, Krusch et al. (2006) also find a steep upturn with $\alpha \sim -1.7$ starting around $M_B > -15$ in Hickson compact groups. While we do see a possible increase in slope around $M_{r'} > -15$, this appears to be followed by a flattening at fainter magnitudes. We do not find any evidence for a slope as steep as -1.7 . If the slope were this steep in our survey region, we would expect to detect the large numbers of bright dwarf galaxies implied by this slope. It is hardly conceivable that our faint-end slope measurement suffers from selection effects compatible with a factor of 10 inconsistency in counts at $M_{r'} \sim -10$. Down to at least $M_{r'} < -10$ we do not find such a steep upturn in the poor M81 Group when constructing the LF from our nearly complete survey of galaxies whose membership is established through more direct means. Alternatively, the M81 Group may represent a different environment than probed in these two studies. Our results are more consistent with the large field surveys such as SDSS and COSMOS which find slopes of -1.3 (or -1.5 with corrections for surface brightness selection effects) and -1.2 respectively (Blanton et al. 2005; Liu et al. 2008). With our deeper survey limit we probe a fainter dwarf galaxy population yet find a similar slope to that found in these redshift studies.

4.4. Implication for Cosmological Models

Assuming the LF follows a constant slope of -1.3 , rather than turning over at $r' > 17.0$ where we start to become incomplete, we would expect to be missing at least ~ 70 M81 Group members in our survey area in the range $17 < r' < 22$ ($-11 < M_{r'} < -6$). If the slope increased to -1.8 at faint magnitudes, beginning at $M_{r'}^f = -12$, we would expect to be missing over 1700 galaxies in our survey area. This is over an order of magnitude greater than we would expect from our data. For the intrinsic faint-end slope to be this steep, we would have to be missing a very large population of very faint and low surface brightness, low stellar concentration galaxies, and based on our simulations, we do not find any evidence that we could be missing such large numbers of galaxies brighter than $M_{r'} = -7$.

Recently there have been a number of successful attempts at bringing model predictions closer into line with the lower number counts of observations. One idea is that the dark matter halo circular velocity is larger than extrapolated from measured stellar velocity dispersions. This could be caused by dark matter halos having much larger extents than the luminous component of the galaxy such that velocity dispersions only provide an estimate of the mass in the interior of the halo (Peñarrubia et al. 2008). Another explanation posits that dark matter ha-

los had more mass at higher redshift but have since lost mass through dynamical friction (Kravtsov et al. 2004). In both of these scenarios, the observed galaxies today correspond to larger dark matter halos in the simulations, thus alleviating the problem of excess counts predicted at the measured luminosities. Another widely used solution to the discrepancy incorporates the effects of reionization on the smallest mass halos in galaxy formation models. Reionization suppresses the accumulation of gas and thus star formation, leaving lower mass halos dark. A number of recent models find good agreement with observations (Simon & Geha 2007; Kang 2008; Bovill & Ricotti 2008).

Koposov et al. (2007) compare the Milky Way LF to semi-analytical predictions and find a reasonable match with Benson et al. (2003) who include effects of tidal disruption and photoionization with CDM theory predictions. Counts to $M_V < -3$ agree well within the uncertainties. This provides some support for the hypothesis that at least part of the cause of the disparity between Λ CDM predictions and observations is due to the suppression of gas accumulation in small galaxies collapsing post reionization although other predictions from their model, such as central surface brightness values, do not agree well with observations. In further support of this idea, Simon & Geha (2007) compare the observed Local Group circular velocity distribution function (a proxy for the mass function) to that predicted from the Via Lactea N-body simulation (Diemand et al. 2007). They find good agreement when assuming that the Local Group halos observed at $z=0$ were the ones which collapsed prior to reionization and which correspond to the model objects with the largest values of v_{circ} at various high redshifts.

We find a faint-end slope of the M81 Group LF to a limiting magnitude of $M_{r'} = -10$ that is much shallower than Λ CDM cosmology would predict but similar to that found for Milky Way halo satellites. We do not reach to the same ultra faint population as is currently being uncovered in the Local Group, and we have not obtained kinematical measurements to directly compare the mass function with theoretical predictions. The M81 halo has a similar mass as the Milky Way, thus solutions to the missing halo problem which bring model number counts into agreement with observations by associating more massive halos with fainter galaxies while lower mass halos remain dark could equally well explain the shallow slope we find. Therefore, part of the explanation for the 'missing galaxy' problem may be in the physics of how mass is converted to light. Incorporating the effects of feedback and star formation efficiency may help reconcile theory and observations. Accounting for the suppression of gas infall into the low mass halos of the forming galaxies by reionization in the early universe may explain the bulk of the discrepancy and naturally explains the noted environmental dependence of the LF, with clusters and more dynamically evolved regions exhibiting slopes with α steeper than -1.4 (see e.g. Trentham et al. (2005); Conselice (2002); Chiboucas & Mateo (2006); de Propris & Pritchet (1998); Bernstein et al. (1995)) as compared to the shallower slopes typically measured in group and field environments, and which we find in the M81 Group.

We have discovered 22 new candidate dwarf galaxies in the M81 Group from our 65 square degree CFHT/MegaCam survey, designed to extend beyond the second turnaround radius for the group. Of these candidates, we believe 12 are likely members. The remainder may prove to be background galaxies, foreground associations of stars, or artifacts in our data. The 12 likely members consist of 3 candidate BCDs lying near the periphery of the group, 1 tidal dwarf candidate lying within the HI tidal bridge between M81 and NGC 3077, and a number of dI and dSph candidates. No new large diffuse or any ultra compact dwarfs are detected. The large fraction of late to early types previously noted in the M81 Group is reconfirmed with our new objects. Assuming all objects lie at the distance of M81, we find r' absolute magnitudes for these new objects range from -6.7 to -13.3 . The faintest object, if real, has a measured size of 90 pc that would cause it to encroach on the 40 - 100 pc size gap region between globular clusters and dwarf galaxies. From false star/galaxy tests we expect to detect nearly 100% of the group member dwarfs down to $M_{r'} = -10$ and over 50% to $M_{r'} = -9$, not quite into the regime of the recently discovered ultra faint Local Group galaxies. Including all 22 previously known M81 Group members in our survey region, we construct the group differential and cumulative luminosity functions and find modestly steep faint-end slopes of $\sim -1.30 \pm 0.06$. Including only the most likely members, we find a similar slope of -1.27 ± 0.06 . This

slope is steeper than what has been found in the case of the Andromeda satellites, but may be consistent with the Local Group after taking into account all new discoveries and including corrections for completeness. Even with the addition of the 22 new candidate dwarf galaxies in the M81 Group, number counts remain an order of magnitude below cosmological predictions of halo counts.

This research was funded in part by NSF award AST03-07706, RFBR grant 07-02-00005, and NASA/STScI grant HST-GO-11126.01-A. Based on observations obtained with MegaPrime/MegaCam, a joint project of CFHT and CEA/DAPNIA, at the Canada-France-Hawaii Telescope (CFHT) which is operated by the National Research Council (NRC) of Canada, the Institut National des Sciences de l'Univers of the Centre National de la Recherche Scientifique (CNRS) of France, and the University of Hawaii. This work is based in part on data products produced at TERAPIX. Thanks to Canada-France-Hawaii Telescope queue observers, TERAPIX at the Institut d'Astrophysique de Paris, and Subaru Telescope support staff, Hélène Courtois and Luca Rizzi for UH88 observations, Viktor Afanasiev and Alex Moiseev for work with the BTA 6m data, and Elias Brinks for providing information on an HI cloudlet near one of our candidates. We thank the referee for constructive comments and suggestions.

REFERENCES

- Afanasiev, V. L. & Moiseev, A. V. 2005, *Astronomy Letters*, 31, 194
 Allen, R. J. & Shu, F. H. 1979, *ApJ*, 227, 67
 Babul, A. & Rees, M. J. 1992, *MNRAS*, 255, 346
 Barkhouse, W. A., Yee, H. K. C., & López-Cruz, O. 2007, *ApJ*, 671, 1471
 Bekki, K., Couch, W. J., & Drinkwater, M. J. 2001a, *ApJ*, 552, L105
 Bekki, K., Couch, W. J., & Shioya, Y. 2001b, *PASJ*, 53, 395
 Belokurov, V., Zucker, D. B., Evans, N. W., Kleyna, J. T., Koposov, S., Hodgkin, S. T., Irwin, M. J., Gilmore, G., Wilkinson, M. I., Fellhauer, M., Bramich, D. M., Hewett, P. C., Vidrih, S., De Jong, J. T. A., Smith, J. A., Rix, H.-W., Bell, E. F., Wyse, R. F. G., Newberg, H. J., Mayor, P. A., Yanny, B., Rockosi, C. M., Gnedin, O. Y., Schneider, D. P., Beers, T. C., Barentine, J. C., Brewington, H., Brinkmann, J., Harvanek, M., Kleinman, S. J., Krzesinski, J., Long, D., Nitta, A., & Snedden, S. A. 2007a, *ApJ*, 654, 897
 —. 2007b, *ApJ*, 654, 897
 Benson, A. J., Frenk, C. S., Baugh, C. M., Cole, S., & Lacey, C. G. 2003, *MNRAS*, 343, 679
 Bernstein, G. M., Nichol, R. C., Tyson, J. A., Ulmer, M. P., & Wittman, D. 1995, *AJ*, 110, 1507+
 Binggeli, B. & Jerjen, H. 1998, *A&A*, 333, 17
 Blanton, M. R., Lupton, R. H., Schlegel, D. J., Strauss, M. A., Brinkmann, J., Fukugita, M., & Loveday, J. 2005, *ApJ*, 631, 208
 Boerngen, F. & Karachentseva, V. E. 1982, *Astronomische Nachrichten*, 303, 189
 —. 1985, *Astronomische Nachrichten*, 306, 301
 Bovill, M. S. & Ricotti, M. 2008, *ArXiv e-prints*, 806
 Boyce, P. J., Phillipps, S., Jones, J. B., Driver, S. P., Smith, R. M., & Couch, W. J. 2001, *MNRAS*, 328, 277
 Brinks, E., Walter, F., & Skillman, E. D. 2007, *ArXiv e-prints*, 708
 Caldwell, N., Armandroff, T. E., Da Costa, G. S., & Seitzer, P. 1998, *AJ*, 115, 535
 Caon, N., Capaccioli, M., & D'Onofrio, M. 1993, *MNRAS*, 265, 1013
 Chiboucas, K. & Mateo, M. 2006, *AJ*, 132, 347
 —. 2007, *ApJS*, 170, 95
 Colin, P., Avila-Reese, V., & Valenzuela, O. 2000, *ApJ*, 542, 622
 Conselice, C. J. 2002, *ApJ*, 573, L5
 Davidge, T. J. 2008, *ArXiv e-prints*, 803
 de Mello, D. F., Smith, L. J., Sabbi, E., Gallagher, J. S., Mountain, M., & Harbeck, D. R. 2008, *AJ*, 135, 548
 de Propris, R. & Pritchet, C. J. 1998, *AJ*, 116, 1118
 Diemand, J., Kuhlen, M., & Madau, P. 2007, *ApJ*, 657, 262
 Drinkwater, M. J., Gregg, M. D., Hilker, M., Couch, W. J., Ferguson, H. C., Jones, B., & Phillipps, S. 2003, *The Cosmic Cauldron*, 25th meeting of the IAU, Joint Discussion 10, 18 July 2003, Sydney, Australia, 10
 Drinkwater, M. J., Jones, J. B., Gregg, M. D., & Phillipps, S. 2000, *Publications of the Astronomical Society of Australia*, 17, 227
 Durrell, P. R., Decesar, M. E., Ciardullo, R., Hurley-Keller, D., & Feldmeier, J. J. 2004, in *IAU Symposium*, Vol. 217, *Recycling Intergalactic and Interstellar Matter*, ed. P.-A. Duc, J. Braine, & E. Brinks, 90+
 Fellhauer, M. & Kroupa, P. 2002, *MNRAS*, 330, 642
 Froebrich, D. & Meusinger, H. 2000, *A&AS*, 145, 229
 Fukugita, M., Ichikawa, T., Gunn, J. E., Doi, M., Shimasaku, K., & Schneider, D. P. 1996a, *AJ*, 111, 1748
 —. 1996b, *AJ*, 111, 1748
 González, R. E., Lares, M., Lambas, D. G., & Valotto, C. 2006, *A&A*, 445, 51
 Haiman, Z., Thoul, A. A., & Loeb, A. 1996, *ApJ*, 464, 523
 Ibata, R., Martin, N. F., Irwin, M., Chapman, S., Ferguson, A. M. N., Lewis, G. F., & McConnachie, A. W. 2007, *ApJ*, 671, 1591
 Irwin, M. & Hatzidimitriou, D. 1995, *MNRAS*, 277, 1354
 Irwin, M. J., Ferguson, A. M. N., Huxor, A. P., Tanvir, N. R., Ibata, R. A., & Lewis, G. F. 2008, *ApJ*, 676, L17
 Jordi, K., Grebel, E. K., & Ammon, K. 2006, *A&A*, 460, 339
 Kamionkowski, M. & Liddle, A. R. 2000, *Physical Review Letters*, 84, 4525
 Kang, X. 2008, *ArXiv e-prints*, 806
 Karachentsev, I. D., Dolphin, A. E., Geisler, D., Grebel, E. K., Guhathakurta, P., Hodge, P. W., Karachentseva, V. E., Sarajedini, A., Seitzer, P., & Sharina, M. E. 2002a, *A&A*, 383, 125
 Karachentsev, I. D., Karachentseva, V. E., Dolphin, A. E., Geisler, D., Grebel, E. K., Guhathakurta, P., Hodge, P. W., Sarajedini, A., Seitzer, P., & Sharina, M. E. 2000, *A&A*, 363, 117
 Karachentsev, I. D., Karachentseva, V. E., Huchtmeier, W. K., & Makarov, D. I. 2004, *AJ*, 127, 2031
 Karachentsev, I. D., Sharina, M. E., Dolphin, A. E., Grebel, E. K., Geisler, D., Guhathakurta, P., Hodge, P. W., Karachentseva, V. E., Sarajedini, A., & Seitzer, P. 2002b, *A&A*, 385, 21

- Karachentseva, V. E. 1968, *Soobshcheniya Byurakanskoj Observatorii Akademii Nauk Armyanskoj SSR Erevan*, 39, 62
- Kawata, D. & Mulchaey, J. S. 2008, *ApJ*, 672, L103
- Kewley, L. J. & Dopita, M. A. 2002, *ApJS*, 142, 35
- Klypin, A., Kravtsov, A. V., Valenzuela, O., & Prada, F. 1999, *ApJ*, 522, 82
- Koposov, S., Belokurov, V., Evans, N. W., Hewett, P. C., Irwin, M. J., Gilmore, G., Zucker, D. B., Rix, H., Fellhauer, M., Bell, E. F., & Glushkova, E. V. 2007, *ArXiv e-prints*, 706
- Kravtsov, A. V., Gnedin, O. Y., & Klypin, A. A. 2004, *ApJ*, 609, 482
- Krusch, E., Rosenbaum, D., Dettmar, R.-J., Bomans, D. J., Taylor, C. L., Aronica, G., & Elwert, T. 2006, *A&A*, 459, 759
- Kurtz, M. J. & Mink, D. J. 1998, *PASP*, 110, 934
- Liu, C. T., Capak, P., Mobasher, B., Paglione, T. A. D., Rich, R. M., Scoville, N. Z., Tribiano, S. M., & Tyson, N. D. 2008, *ApJ*, 672, 198
- Lynds, R., Tolstoy, E., O'Neil, Jr., E. J., & Hunter, D. A. 1998, *AJ*, 116, 146
- Mahdavi, A., Trentham, N., & Tully, R. B. 2005, *AJ*, 130, 1502
- Majewski, S. R., Beaton, R. L., Patterson, R. J., Kalirai, J. S., Geha, M. C., Muñoz, R. R., Seigar, M. S., Guhathakurta, P., Gilbert, K. M., Rich, R. M., Bullock, J. S., & Reitzel, D. B. 2007, *ApJ*, 670, L9
- Makarov, D., Makarova, L., Rizzi, L., Tully, R. B., Dolphin, A. E., Sakai, S., & Shaya, E. J. 2006, *AJ*, 132, 2729
- Makarova, L. N., Grebel, E. K., Karachentsev, I. D., Dolphin, A. E., Karachentseva, V. E., Sharina, M. E., Geisler, D., Guhathakurta, P., Hodge, P. W., Sarajedini, A., & Seitzer, P. 2002, *A&A*, 396, 473
- Martin, N. F., Ibata, R. A., Irwin, M. J., Chapman, S., Lewis, G. F., Ferguson, A. M. N., Tanvir, N., & McConnachie, A. W. 2006, *MNRAS*, 371, 1983
- Mateo, M. L. 1998, *ARA&A*, 36, 435
- McConnachie, A., Huxor, A., Martin, N., Irwin, M., Chapman, S., Fahlman, G., Ferguson, A., Ibata, R., Lewis, G., Richer, H., & Tanvir, N. 2008, *ArXiv e-prints*, 806
- McConnachie, A. W. & Irwin, M. J. 2006, *MNRAS*, 365, 1263
- Monet, D. G., Levine, S. E., Canzian, B., Ables, H. D., Bird, A. R., Dahn, C. C., Guetter, H. H., Harris, H. C., Henden, A. A., Leggett, S. K., Levison, H. F., Luginbuhl, C. B., Martini, J., Monet, A. K. B., Munn, J. A., Pier, J. R., Rhodes, A. R., Riepe, B., Sell, S., Stone, R. C., Vrba, F. J., Walker, R. L., Westerhout, G., Brucato, R. J., Reid, I. N., Schoening, W., Hartley, M., Read, M. A., & Tritton, S. B. 2003, *AJ*, 125, 984
- Moore, B., Ghigna, S., Governato, F., Lake, G., Quinn, T., Stadel, J., & Tozzi, P. 1999, *ApJ*, 524, L19
- Moore, B., Katz, N., Lake, G., Dressler, A., & Oemler, A. 1996, *Nature*, 379, 613
- Moore, B., Lake, G., & Katz, N. 1998, *ApJ*, 495, 139
- Mori, M. & Burkert, A. 2000, *ApJ*, 538, 559
- Peñarrubia, J., McConnachie, A. W., & Navarro, J. F. 2008, *ApJ*, 672, 904
- Perlmutter, J.-M. & Racine, R. 1995, *AJ*, 109, 1055
- Pettini, M. & Pagel, B. E. J. 2004, *MNRAS*, 348, L59
- Press, W. H., Teukolsky, S. A., Vetterling, W. T., & Flannery, B. P. 1992, *Numerical recipes in FORTRAN. The art of scientific computing* (Cambridge: University Press, —c1992, 2nd ed.)
- Pritchett, C. J. & van den Bergh, S. 1999, *AJ*, 118, 883
- Roberts, S., Davies, J., Sabatini, S., Auld, R., & Smith, R. 2007, *MNRAS*, 379, 1053
- Roberts, S., Davies, J., Sabatini, S., van Driel, W., O'Neil, K., Baes, M., Linder, S., Smith, R., & Evans, R. 2004, *MNRAS*, 352, 478
- Sabbi, E., Gallagher, J. S., Smith, L. J., de Mello, D. F., & Mountain, M. 2008, *ArXiv e-prints*, 802
- Schechter, P. 1976, *ApJ*, 203, 297
- Schlegel, D. J., Finkbeiner, D. P., & Davis, M. 1998, *ApJ*, 500, 525+
- Secker, J. & Harris, W. E. 1997, *PASP*, 109, 1364
- Secker, J., Harris, W. E., & Plummer, J. D. 1997, *PASP*, 109, 1377
- Shaya, E. J. & Tully, R. B. 1984, *ApJ*, 281, 56
- Simon, J. D. & Geha, M. 2007, *ArXiv e-prints*, 706
- Stoehr, F., White, S. D. M., Tormen, G., & Springel, V. 2002, *MNRAS*, 335, L84
- Strigari, L. E., Bullock, J. S., Kaplinghat, M., Diemand, J., Kuhlen, M., & Madau, P. 2007, *ApJ*, 669, 676
- Thoul, A. A. & Weinberg, D. H. 1996, *ApJ*, 465, 608
- Trentham, N. 1997, *MNRAS*, 286, 133
- Trentham, N., Sampson, L., & Banerji, M. 2005, *MNRAS*, 357, 783
- Trentham, N. & Tully, R. B. 2002, *MNRAS*, 335, 712
- Trentham, N., Tully, R. B., & Mahdavi, A. 2006, *MNRAS*, 369, 1375
- Tully, R. B., Boesgaard, A. M., Dyck, H. M., & Schempp, W. V. 1981, *ApJ*, 246, 38
- Tully, R. B. & Pierce, M. J. 2000, *ApJ*, 533, 744
- Tully, R. B., Somerville, R. S., Trentham, N., & Verheijen, M. A. W. 2002, *ApJ*, 569, 573
- Tully, R. B., Verheijen, M. A. W., Pierce, M. J., Huang, J.-S., & Wainscoat, R. J. 1996, *AJ*, 112, 2471
- van den Bergh, S. 1966, *AJ*, 71, 922
- 2006, *AJ*, 132, 1571
- van Zee, L., Salzer, J. J., & Skillman, E. D. 2001, *AJ*, 122, 121
- Walsh, S. M., Jerjen, H., & Willman, B. 2007, *ApJ*, 662, L83
- Willman, B., Blanton, M. R., West, A. A., Dalcanton, J. J., Hogg, D. W., Schneider, D. P., Wherry, N., Yanny, B., & Brinkmann, J. 2005, *AJ*, 129, 2692
- Young, L. M., Skillman, E. D., Weisz, D. R., & Dolphin, A. E. 2007, *ApJ*, 659, 331
- Yun, M. S., Ho, P. T. P., & Lo, K. Y. 1994, *Nature*, 372, 530
- Zabludoff, A. I. & Mulchaey, J. S. 2000, *ApJ*, 539, 136
- Zucker, D. B., Belokurov, V., Evans, N. W., Kley, J. T., Irwin, M. J., Wilkinson, M. I., Fellhauer, M., Bramich, D. M., Gilmore, G., Newberg, H. J., Yanny, B., Smith, J. A., Hewett, P. C., Bell, E. F., Rix, H.-W., Gnedin, O. Y., Vidrih, S., Wyse, R. F. G., Willman, B., Grebel, E. K., Schneider, D. P., Beers, T. C., Kniazev, A. Y., Barentine, J. C., Brewington, H., Brinkmann, J., Harvanek, M., Kleinman, S. J., Krzesinski, J., Long, D., Nitta, A., & Snedden, S. A. 2006, *ApJ*, 650, L41

TABLE 1
NEW M81 DWARF CANDIDATES

Name	α	δ J2000.0	B_t^a	$a' \times b'^b$	Type	Comments
d0926+70	09 26 27.9	+70 30 24	19.0	0.8×0.6	dI	
d0934+70	09 34 03.7	+70 12 57	19.3	0.7×0.6	dSph	behind cirrus
d0939+71	09 39 15.9	+71 18 42	20.0	0.7×0.6	dSph?	9.4 arcmin from HoI
d0944+69	09 44 22.5	+69 12 40	21.0	0.2×0.2	dSph	
d0944+71	09 44 34.4	+71 28 57	17.5	1.3×0.8	dI	behind brt foreground star
d0946+68	09 46 13.0	+68 42 55	20.5	0.2×0.2	dI	background?
d0955+70	09 55 13.6	+70 24 29	20.5	0.8×0.7	dSph	
d0957+70	09 57 12.4	+70 12 35	21.0	0.3×0.3	dSph?	
d0958+66	09 58 48.5	+66 50 59	16.0	1.6×0.8	BCD	KUG 0954+670
d0959+68	09 59 33.1	+68 39 25	18.0	0.8×0.6	dI/tdI	tidal? Durrell et al. (2004)
d1006+67	10 06 46.2	+67 12 04	21.0	0.7×0.7	dSph	
d1009+70	10 09 34.9	+70 32 55	18.5	0.6×0.5	dI	semi-resolved, background?
d1012+64	10 12 48.4	+64 06 27	15.6	1.4×0.9	BCD	UGC5497
d1013+68	10 13 11.7	+68 43 45	20.5	1.5×0.9	dI?	artifact?
d1014+68	10 14 55.8	+68 45 27	21.0	0.4×0.4	dSph	
d1015+69	10 15 06.9	+69 02 15	20.5	0.4×0.3	dI	backgrnd?
d1016+69	10 16 18.3	+69 29 45	21.0	0.4×0.4	dSph	
d1019+69	10 19 52.9	+69 11 19	18.5	0.6×0.5	dI	backgrnd?
d1020+69	10 20 25.0	+69 11 50	20.5	1.5×0.7	dSph?	artifact?
d1028+70	10 28 39.7	+70 14 01	16.2	1.4×0.9	BCD	
d1041+70	10 41 16.8	+70 09 03	20.5	0.8×0.4	dI	pear-shaped
d1048+70	10 48 57.0	+70 25 38	21.0	1.0×0.9	dSph	background?

^a B_t are estimated by eye on POSS-II

^bangular dimensions correspond to an isophote 28m arcsec^{-2}

TABLE 2
SPECTROSCOPY OF 5 DWARFS IN M81

Name	α	δ (J2000.0)	telescope	date	exposure (s)	grating	objects	$V_{rad(Sub)}$ (km/s)	$V_{rad(BTA)}$ (km/s)
Previously known:									
F8D1	9 44 39.3	+67 26 06	Subaru	24 Nov 06	1800	VPH	globular cluster	-125 ± 130	
IKN	10 08 05.2	+68 24 33	Subaru	24 Nov 06	1800	VPH	globular cluster	-140 ± 64	
New Candidates:									
d0958+66	09 58 48.5	+66 50 59	Subaru	22 Nov 06	600	R300	galaxy	$+33 \pm 94$	
			BTA	11 Nov 06	600	VPHG400	galaxy		$+90 \pm 50$
d1028+70	10 28 39.7	+70 14 01	Subaru	23 Nov 06	600	VPH	galaxy	-90 ± 79	
			BTA	11 Nov 06	600	VPHG400	galaxy		-114 ± 50
d1012+64	10 12 48.4	+64 06 27	BTA	20 Oct 07	900	VPHG400	galaxy		$+150 \pm 50$

TABLE 3
STRUCTURAL AND PHOTOMETRIC PROPERTIES OF M81 GROUP CANDIDATES

galaxy	r'_{ap} ^a	r'_{ap2} ^b	r'_{fit} ^c	$(V-I)^d$	ϵ	PA	$r'_{arcsec^{-2}}$	μ_0	$r'_{arcsec^{-2}}$	$\langle \mu_e \rangle$	R_e	R_e	n	$A_{r'}$	$r'_{cor,e}$	$r'_{cor,s}$	$M_{r',cor,s}$	g
	mag	mag	mag			deg		$arcsec^{-2}$	$arcsec^{-2}$	$arcsec^{-2}$	arcsec	kpc	mag	mag	mag	mag	$M_{r',cor,s}$	mag
d0926+70 [†]	18.3	18.9	18.4	0.87	0.18	-23.9	26.0	26.2	26.2	14.3	0.25	0.42	0.48	17.4	17.9	17.9	-9.9	-9.9
d0934+70 [†]	18.9	18.9	18.5	1.07	0.07	63.5	26.2	26.4	26.4	15.3	0.27	0.42	0.66	17.5	18.0	18.0	-9.8	-9.8
d0939+71	18.9	19.1	18.2		0.05	-80.9	25.5	26.1	26.1	15.3	0.27	0.66	0.09	18.3	18.5	18.5	-9.3	-9.3
d0944+69	21.6	21.9	21.2		0.09	-9.7	25.9	26.7	26.7	4.9	0.09	0.78	0.22	20.7	21.1	21.1	-6.7	-6.7
d0944+71	15.6	15.9	15.6		0.20	-27.4	23.4	23.9	23.9	18.3	0.32	0.61	0.09	15.0	15.2	15.2	-12.6	-12.6
d0946+68	19.4	19.5	19.6		0.04	48.6	24.8	25.6	25.6	7.5	0.13	0.76	0.21	19.0	19.2	19.2	-8.6	-8.6
d0955+70	18.5	18.6	18.8	1.03	0.04	86.8	26.6	27.1	27.1	18.6	0.32	0.61	0.43	17.5	17.9	17.9	-9.9	-9.9
d0957+70	19.5	19.3	19.9		0.04	-27.6	27.1	27.3	27.3	11.3	0.20	0.36	0.24	18.2	19.1	19.1	-8.7	-8.7
d0958+66	14.8	14.8	15.0	0.84	0.36	-6.9	21.6	22.3	22.3	11.6	0.20	0.71	0.17	14.7	14.7	14.7	-13.1	-13.1
d0959+68 [†]	16.4	16.5	16.2	0.74	0.10	35.1	26.0	26.5	26.5	26.6	0.46	0.21	0.20	16.2	16.2	16.2	-11.6	-11.6
d1006+67	18.3	18.5	18.1		0.05	86.1	26.2	26.5	26.5	18.1	0.32	0.44	0.17	17.6	18.0	18.0	-9.8	-9.8
d1009+70	17.9	17.8	17.8	0.68	0.19	-17.6	24.9	25.2	25.2	11.6	0.20	0.50	0.38	17.4	17.5	17.5	-10.3	-10.3
d1012+64	14.6	14.6	14.6		0.15	17.0	21.5	22.3	22.3	13.9	0.24	0.88	0.05	14.5	14.5	14.5	-13.3	-13.3
d1013+68 [†]	19.0	19.6	18.6		0.10	-34.5	26.9	27.9	27.9	29.5	0.51	1.00	0.11	18.5	18.5	18.5	-9.3	-9.3
d1014+68	18.7	18.8	18.8		0.01	-8.9	27.2	27.3	27.3	19.7	0.34	0.29	0.13	17.5	18.5	18.5	-9.3	-9.3
d1015+69 [†]	19.4	19.5	19.4		0.07	-49.7	25.5	26.0	26.0	8.5	0.15	0.68	0.13	18.9	19.1	19.1	-8.7	-8.7
d1016+69	18.9	19.0	19.1		0.01	87.6	27.1	27.6	27.6	19.3	0.34	0.60	0.13	17.8	18.4	18.4	-9.4	-9.4
d1019+69	18.1	17.5	18.1		0.09	38.1	24.5	25.0	25.0	9.8	0.17	0.63	0.11	17.7	17.8	17.8	-10.0	-10.0
d1020+69	18.6	18.3	18.1		0.13	-31.5	26.7	26.9	26.9	22.3	0.39	0.41	0.10	17.5	18.1	18.1	-9.7	-9.7
d1028+70	15.7	15.7	15.7	0.77	0.20	-54.8	22.4	23.3	23.3	13.4	0.23	0.88	0.11	15.5	15.5	15.5	-12.3	-12.3
d1041+70	18.5	18.6	19.0	1.00	0.18	26.0	26.1	26.2	26.2	10.9	0.19	0.30	0.15	18.1	18.5	18.5	-9.3	-9.3
d1048+70 [†]	18.3	19.5	19.4		0.02	-10.6	27.3	27.6	27.6	17.5	0.30	0.42	0.10	18.2	18.7	18.7	-9.1	-9.1

Note. — Measured apparent magnitudes and surface brightnesses are uncorrected for extinction.

^aMagnitude measured in circular aperture, mean sky measured in circular annulus $> 2r_{galaxy}$

^bAperture magnitude with sky+foreground contamination estimated from counts in nearby circular apertures

^cMagnitude from curve of growth fitting with cumulative Sersic function

^dIntegrated color within R_e

^eAverage measured r' corrected to total magnitudes assuming an exponential profile, extinction corrected. See text.

^fAverage measured r' corrected to total magnitudes assuming a Sersic profile, extinction corrected. See text.

^gExtinction corrected absolute magnitude assuming galaxy is at the distance of M81, 3.6Mpc, and taking the Sersic profile corrected r' measurement

[†]Measurements affected by cirrus or foreground/background objects, or not well fit by a Sersic function

TABLE 4
PHOTOMETRY OF PREVIOUSLY KNOWN M81 GROUP MEMBERS

Name	α (J2000.0)	δ	type	ϵ	μ_o $r' \text{ arcsec}^{-2}$	μ_e $r' \text{ arcsec}^{-2}$	R_e arcsec	r'_{meas}	$A_{r'}$ mag	r'_{core} ^a mag	r'_{cor_s} ^b mag	$M_{r'_{cor_s}}$ ^c
HoI	9 40 28.2	+71 11 11	dI		25.0	25.2	66.7	13.9	0.1	13.4	13.4	-14.4
F8D1	9 44 50.0	+67 28 32	dSph		26.5	26.6	67.3	15.3	0.2	14.0	14.7	-13.0
FM1	9 45 10.0	+68 45 54	dSph	0.14	24.8	25.2	21.1	16.5	0.2	15.9	16.2	-11.5
N2976	9 47 15.6	+67 54 49	Sc pec	0.60	20.4	20.7	43.6	10.5	0.2	9.7	9.8	-18.0
KK77	9 50 10.0	+67 30 24	dSph	0.29	24.5	25.2	36.7	15.4	0.4	14.7	14.9	-12.8
BK3N	9 53 48.5	+68 58 09	dI	0.01	25.9	24.8	6.7	18.6	0.2	17.8	17.8	-10.2
M81	9 55 33.5	+69 04 00	Sb		17.1	19.3	81.1	7.8	0.2	7.2	7.2	-20.6
M82	9 55 53.9	+69 40 57	Irr		17.4	19.1	60.0	8.4	0.4	7.9	7.9	-19.9
K61	9 57 02.7	+68 35 30	dSph	0.25	23.9	24.7	38.4	14.8	0.2	14.5	14.5	-13.3
A0952+69	9 57 29.0	+69 16 20	pec					16.3	0.2			
HoIX	9 57 32.4	+69 02 35	dI	0.24	24.1	24.7	46.8	14.3	0.2	13.9	14.0	-13.8
N3077	10 03 21.0	+68 44 02	Irr	0.24	19.6	20.2	37.5	10.3	0.2	10.0	10.1	-17.8
Garland	10 03 42.0	+68 41 36	pec					16.5	0.2			
BK5N	10 04 40.3	+68 15 20	dSph	0.20	24.5	25.1	22.1	16.4	0.1	16.1	16.1	-11.8
K63	10 05 07.3	+66 33 18	dSph	0.18	23.9	24.1	24.9	15.1	0.2	14.4	14.8	-13.0
K64	10 07 01.9	+67 49 39	dSph	0.33	23.2	23.8	22.1	15.1	0.2	14.6	14.7	-13.1
IKN	10 08 05.9	+68 23 57	dSph					(15.7)	0.2	(15.5)	(15.5)	(-12.3)
HS117	10 21 25.2	+71 06 58	dI	0.39	24.3	24.8	19.9	16.3	0.3	15.5	15.9	-11.9
DDO78	10 26 27.9	+67 39 24	dSph	(0.10)	(24.8)	(25.0)	(25.0)	(15.9)	0.1	(15.0)	(15.0)	(-12.8)
IC2574	10 28 22.4	+68 24 58	SABm		22.6	24.0	142.0	11.5	0.3	10.2	10.3	-17.7
DDO82	10 30 35.0	+70 37 10	Im	0.40	21.8	22.7	33.9	13.1	0.1	12.9	12.9	-15.1
BK6N	10 34 31.9	+66 00 42	dSph	0.32	24.6	24.6	16.6	16.2	0.0	15.9	15.9	-12.0

Note. — Values in parentheses highly uncertain due to presence of bright foreground stars. Values for brightest galaxies may be underestimates due to sky subtraction errors in the TERAPIX reduction pipeline.

^aCorrected for extinction and flux lost in sky assuming an exponential profile.

^bCorrected for extinction and flux lost in sky assuming a Sersic profile.

^cAbsolute Sersic profile corrected magnitude, using distance moduli from Table 2 of Karachentsev et al. (2002a) or assuming 27.8 where not provided.

TABLE 5
FAINT-END SLOPE FROM DIFFERENTIAL LUMINOSITY FUNCTIONS

Sample	$\alpha (r'_{meas})$	$\alpha (r'_{cor(exp)})$	$\alpha (r'_{cor(sersic)})$
All (completeness corr.)	$-1.29^{+0.04}_{-0.04}$	$-1.28^{+0.04}_{-0.05}$	$-1.32^{+0.04}_{-0.05}$
All	$-1.26^{+0.09}_{-0.08}$	$-1.39^{+0.05}_{-0.05}$	$-1.36^{+0.09}_{-0.08}$
Best	$-1.20^{+0.10}_{-0.10}$	$-1.34^{+0.07}_{-0.07}$	$-1.30^{+0.10}_{-0.10}$
Original	$-1.19^{+0.07}_{-0.07}$	$-1.24^{+0.09}_{-0.08}$	$-1.26^{+0.08}_{-0.08}$
All ($-15 \leq r' < -10$)	$-1.43^{+0.09}_{-0.09}$	$-1.44^{+0.07}_{-0.07}$	$-1.46^{+0.10}_{-0.10}$

TABLE 6
FAINT-END SLOPE FROM INTEGRATED LUMINOSITY FUNCTIONS

Sample	$\alpha (r'_{meas})$	$\alpha (r'_{cor(exp)})$	$\alpha (r'_{cor(sersic)})$
All (completeness corr.)	$-1.29^{+0.02}_{-0.05}$	$-1.28^{+0.03}_{-0.05}$	$-1.28^{+0.02}_{-0.05}$
All	$-1.29^{+0.04}_{-0.06}$	$-1.29^{+0.05}_{-0.08}$	$-1.28^{+0.04}_{-0.04}$
Best	$-1.27^{+0.05}_{-0.06}$	$-1.27^{+0.04}_{-0.07}$	$-1.26^{+0.05}_{-0.04}$
Original	$-1.26^{+0.07}_{-0.10}$	$-1.24^{+0.06}_{-0.07}$	$-1.25^{+0.06}_{-0.06}$

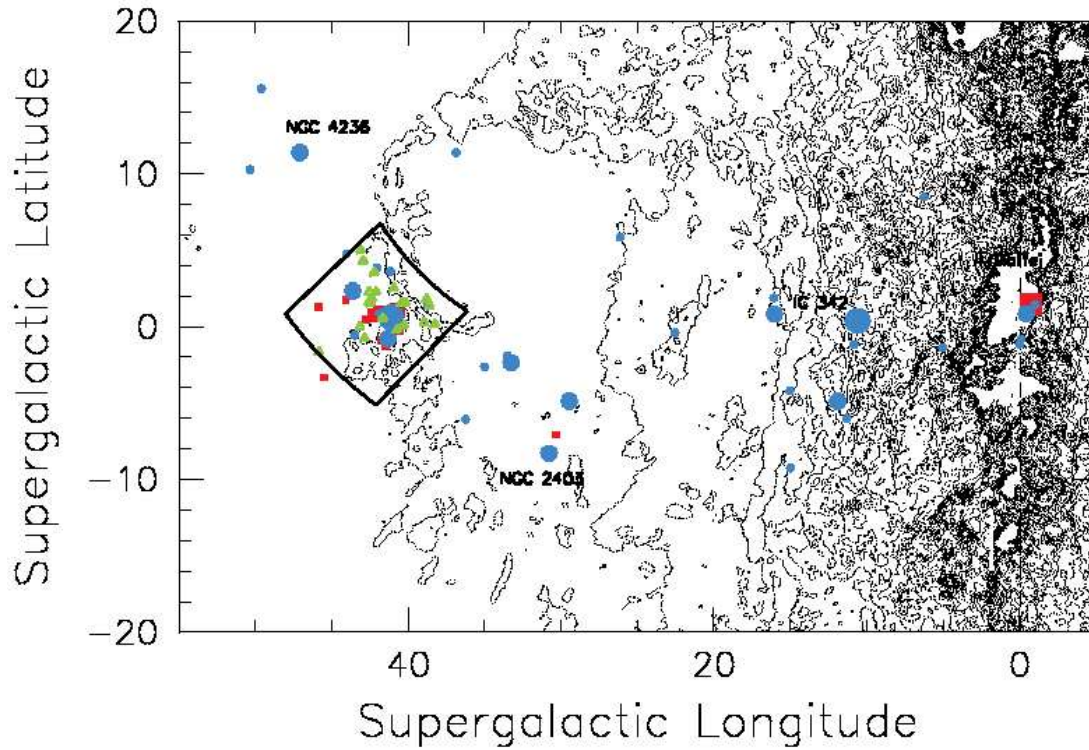


FIG. 1.— The extended region around M81. All galaxies with velocities in the Galactic standard of rest less than 400 km s^{-1} in an area of 60×40 degrees in supergalactic coordinates. Circles: spirals and irregulars. Squares: early types. Large, mid, and small symbols identify galaxies with $M_B < -20$, $-20 < M_B < -16$, and $M_B > -16$, respectively. The box outlines the area of the CFHT MegaCam survey and the small open triangles identify the newly discovered dwarfs. Contours illustrate the dust maps of Schlegel et al. (1998) at intervals of $0.2 r'$ magnitudes of extinction.

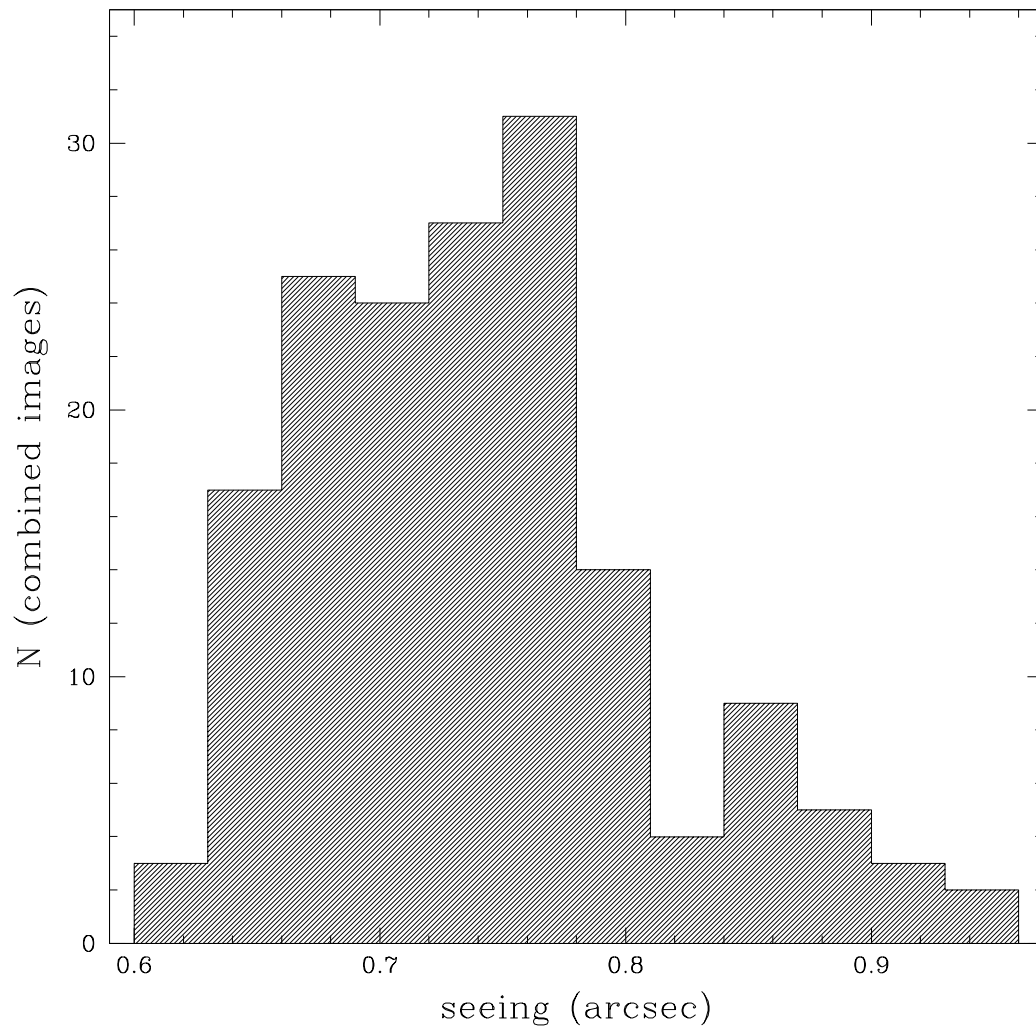


FIG. 2.— Histogram displaying the seeing range for all combined images in our survey.

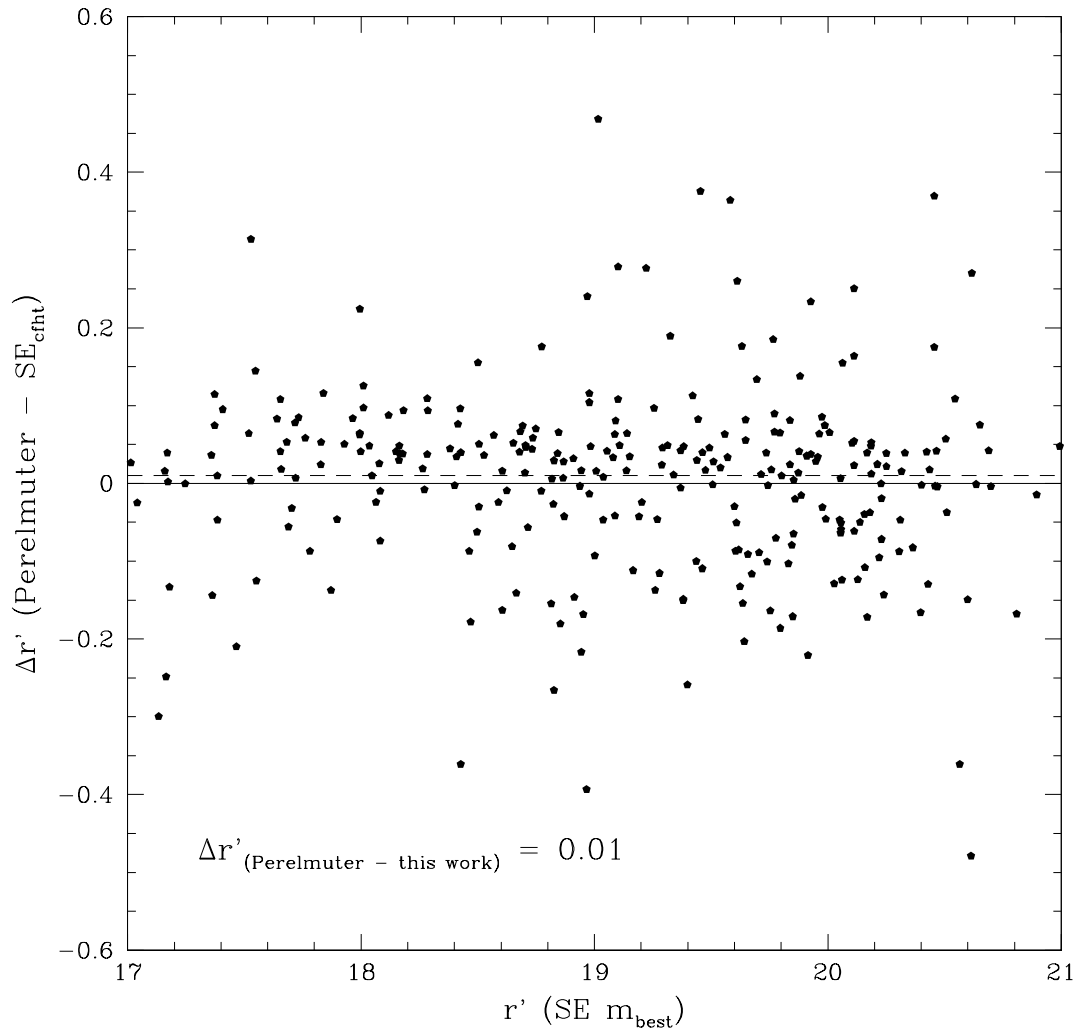


FIG. 3.— Tests of photometric accuracy. We compare our r' total magnitudes to transformed R magnitudes of Perelmuter & Racine (1995).

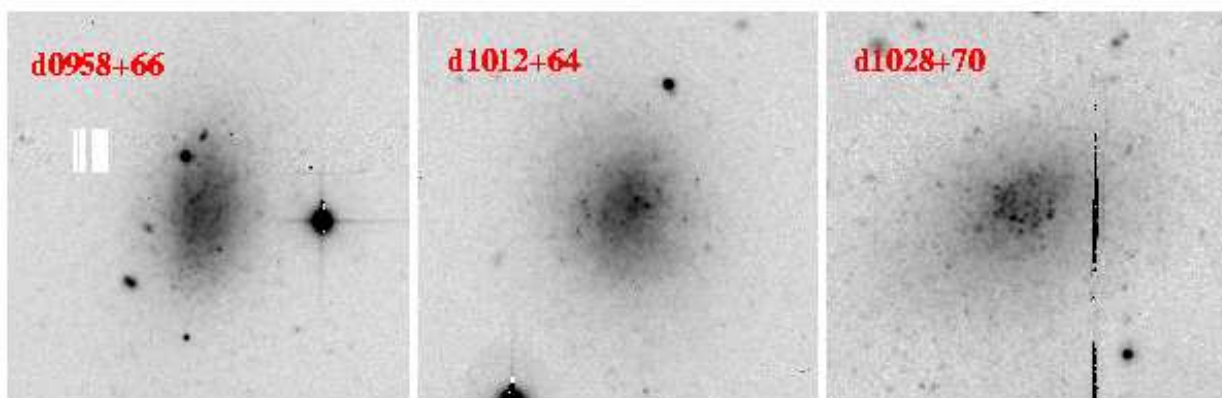


FIG. 4.— Thumbnails of the 3 new M81 candidate BCDs. Images are 1.5 arcmin on a side.

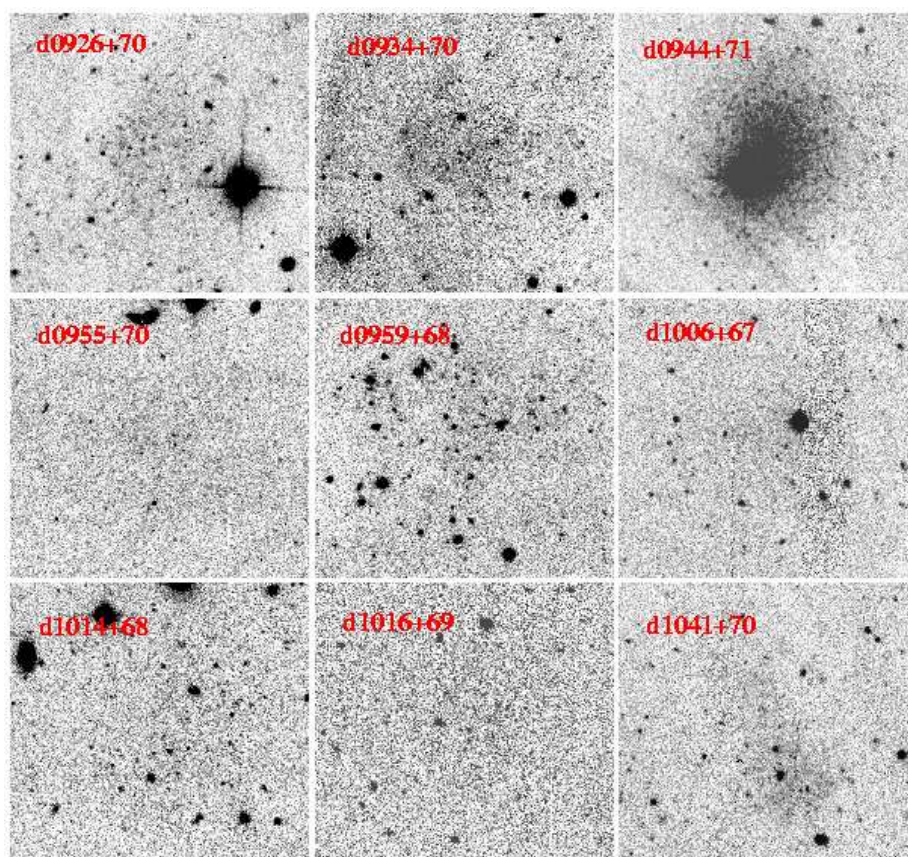


FIG. 5.— We display a mosaic of images of 9 new candidates that were detected by eye and/or 2-point correlation of resolved points. Images are 1.5 arcmin on a side.

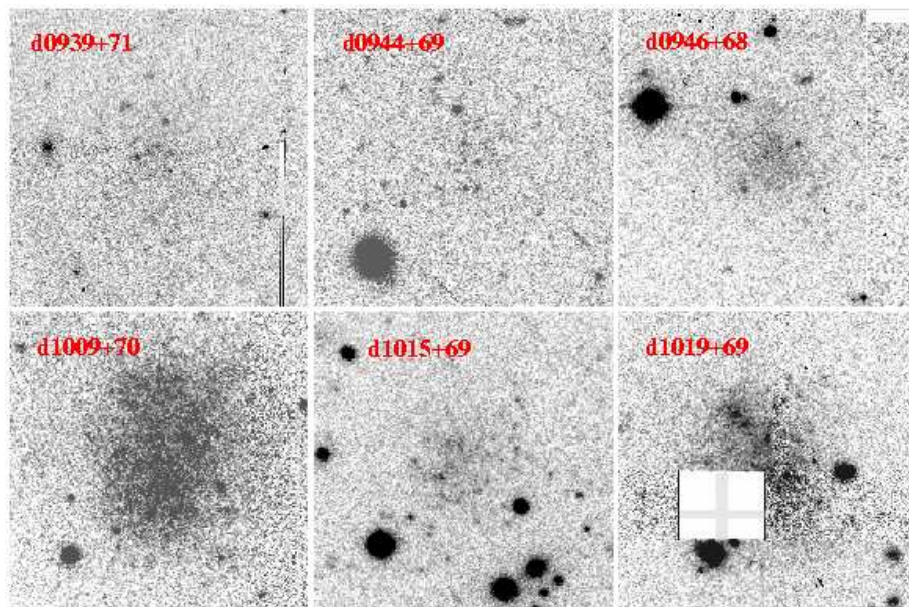


FIG. 6.— While these six candidates have a slight degree of resolution, many of these may prove to lie in the background of the M81 Group.

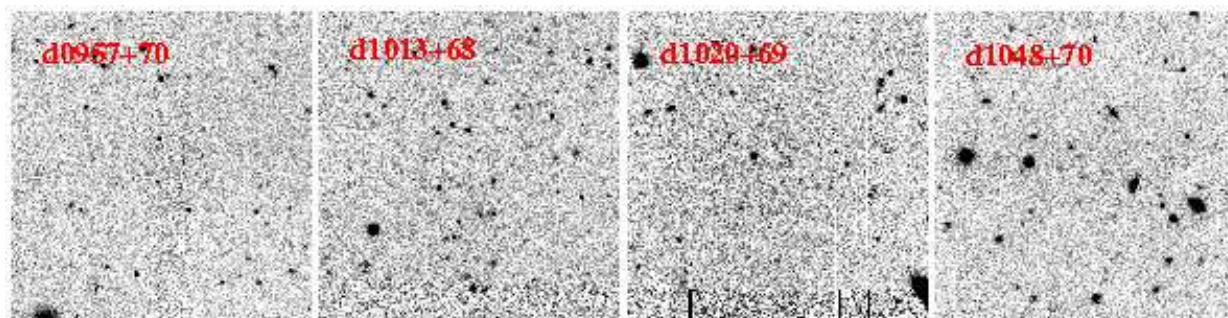


FIG. 7.— Four candidates which may turn out to be artifacts (excess noise or foreground concentrations of stars) or distant galaxy clusters.

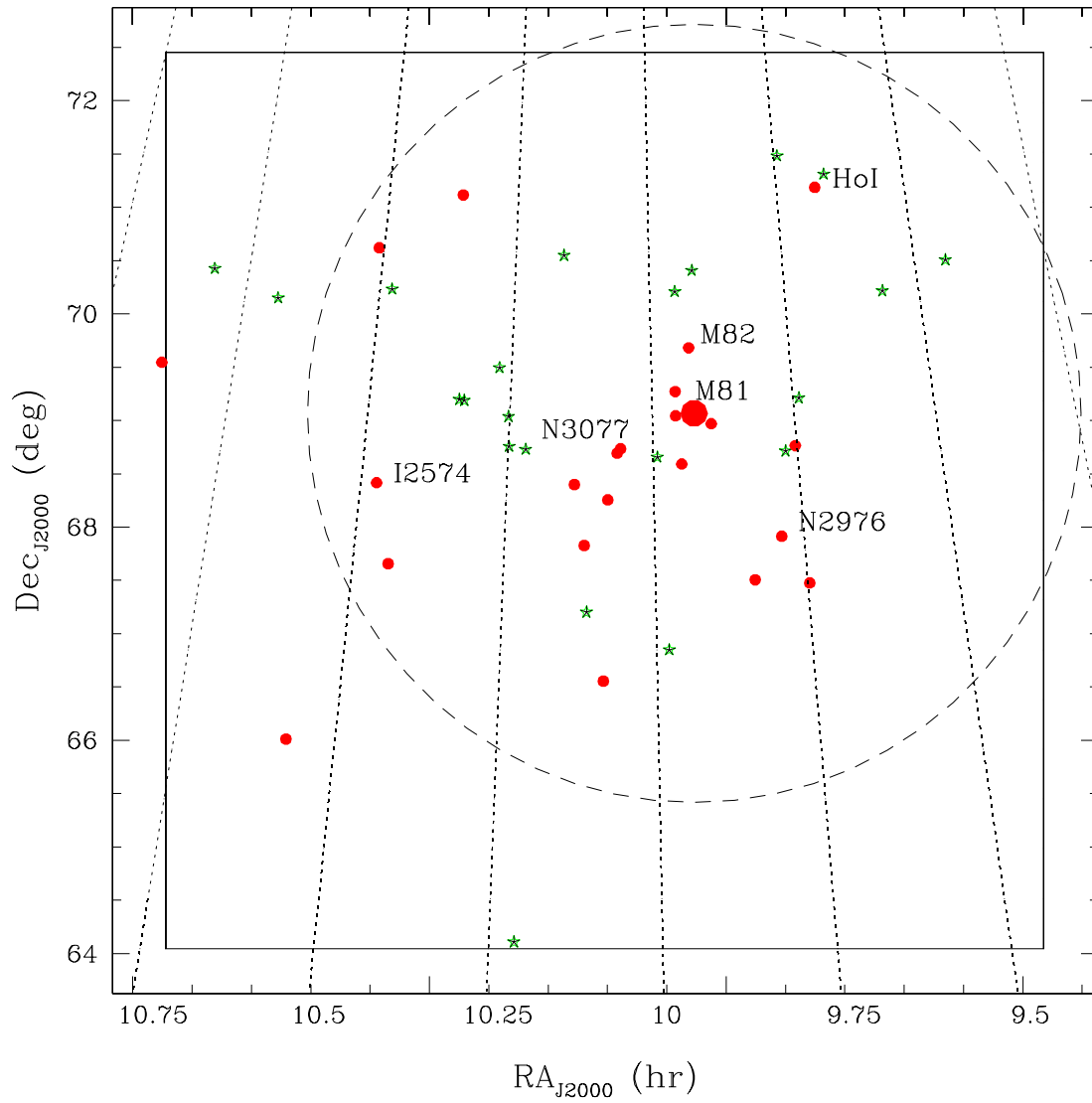


FIG. 8.— Map of our M81 survey region (large box almost filling the figure). Circles indicate previously known group members while stars denote the location of the new group candidates. The large dashed circle is the projection of the putative surface of second turnaround at 230 kpc from M81.

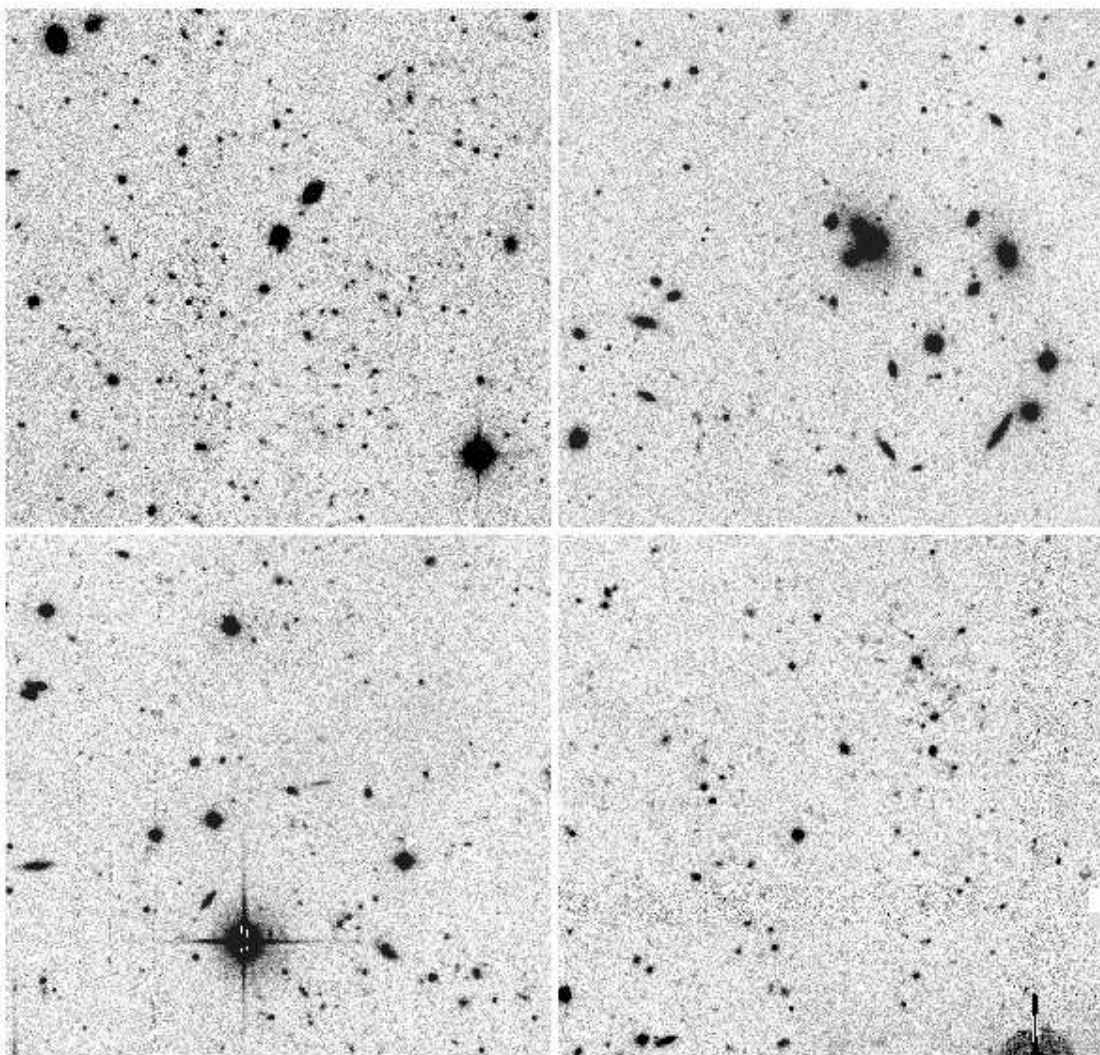


FIG. 9.— Four examples of object concentrations detected with our 2-point correlation routine that we believe to be distant galaxy clusters. Image sections are 2.2 arcmin across.

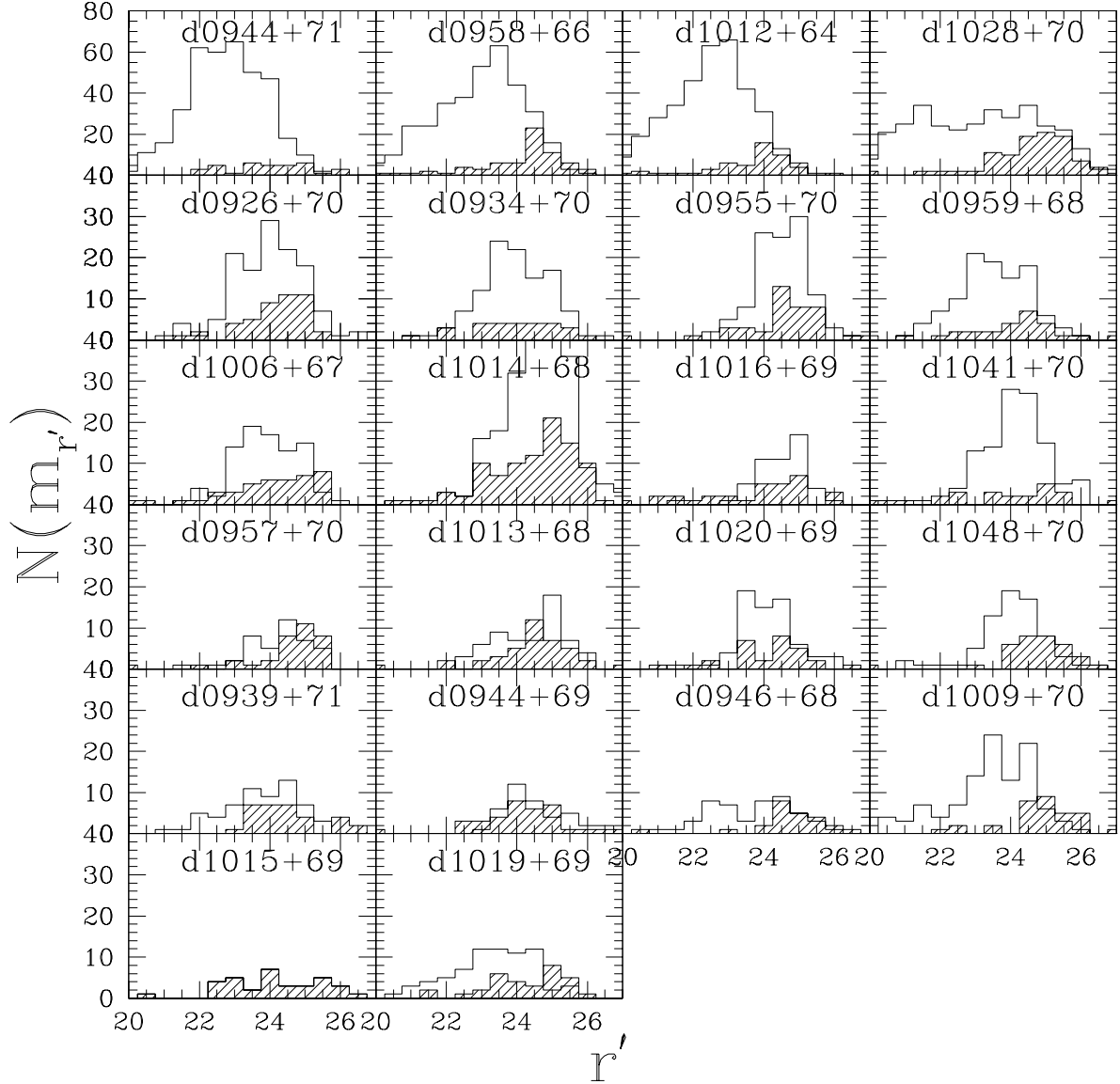


FIG. 10.— We display histograms of the resolved objects in the new M81 candidates. Number counts of objects recovered by SExtractor within a 30–45 arcsec radius (see text) centered on the new candidates are binned as a function of magnitude. The top row includes 4 objects, including 3 BCD candidates, with the largest resolved stellar populations. The next 2 rows include a further 8 good candidates. The 4th row contains 4 objects that may prove to be artifacts, while the bottom 2 rows include possible more distant galaxies. The shaded histograms represent number counts in an identical sized region 2.5 arcmin west of each galaxy.

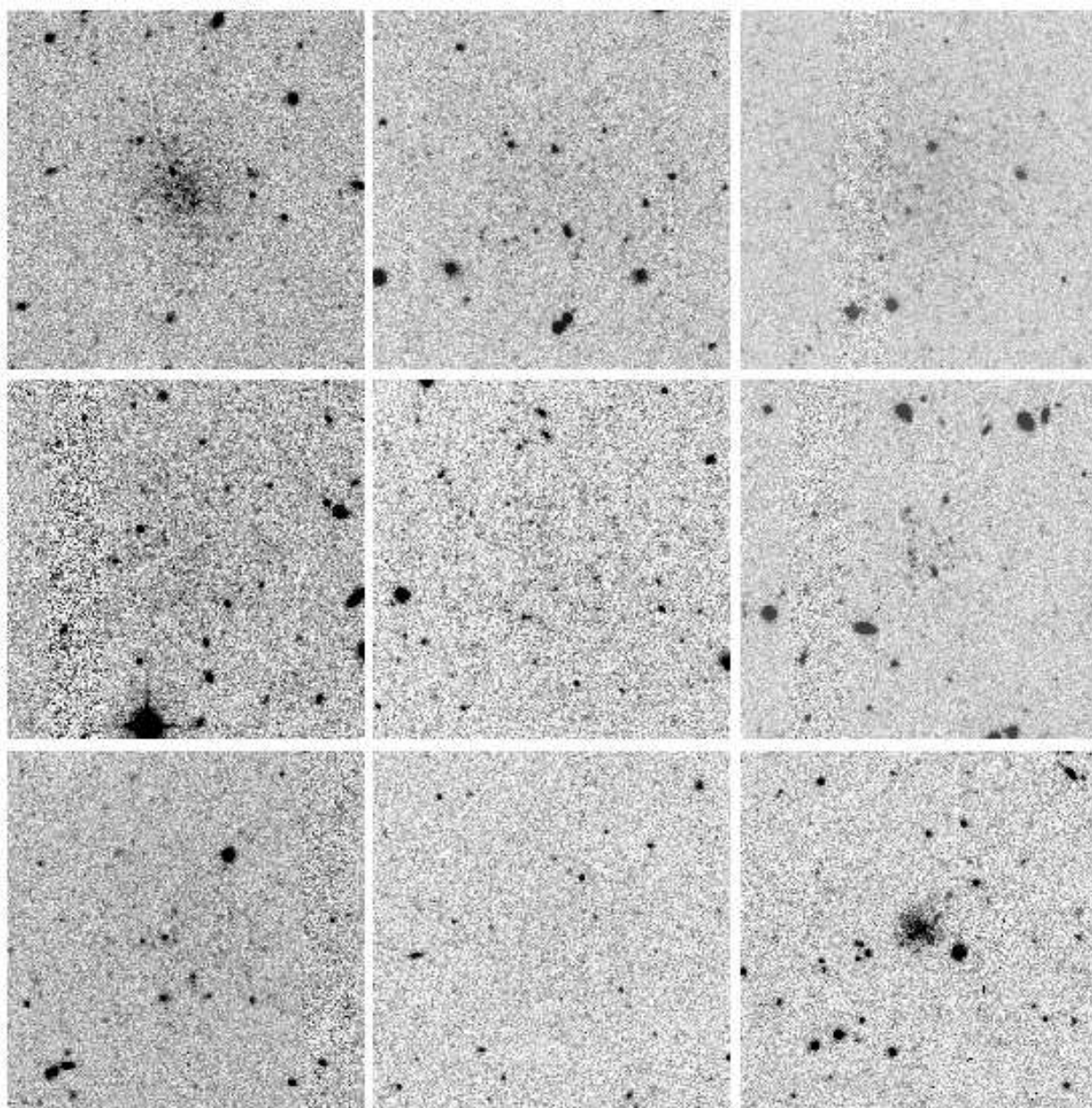


FIG. 11.— Examples of artificial galaxies that were added to real images with which we test the recovery efficiency of our detection techniques. Images are 1.5 arcmin on a side.

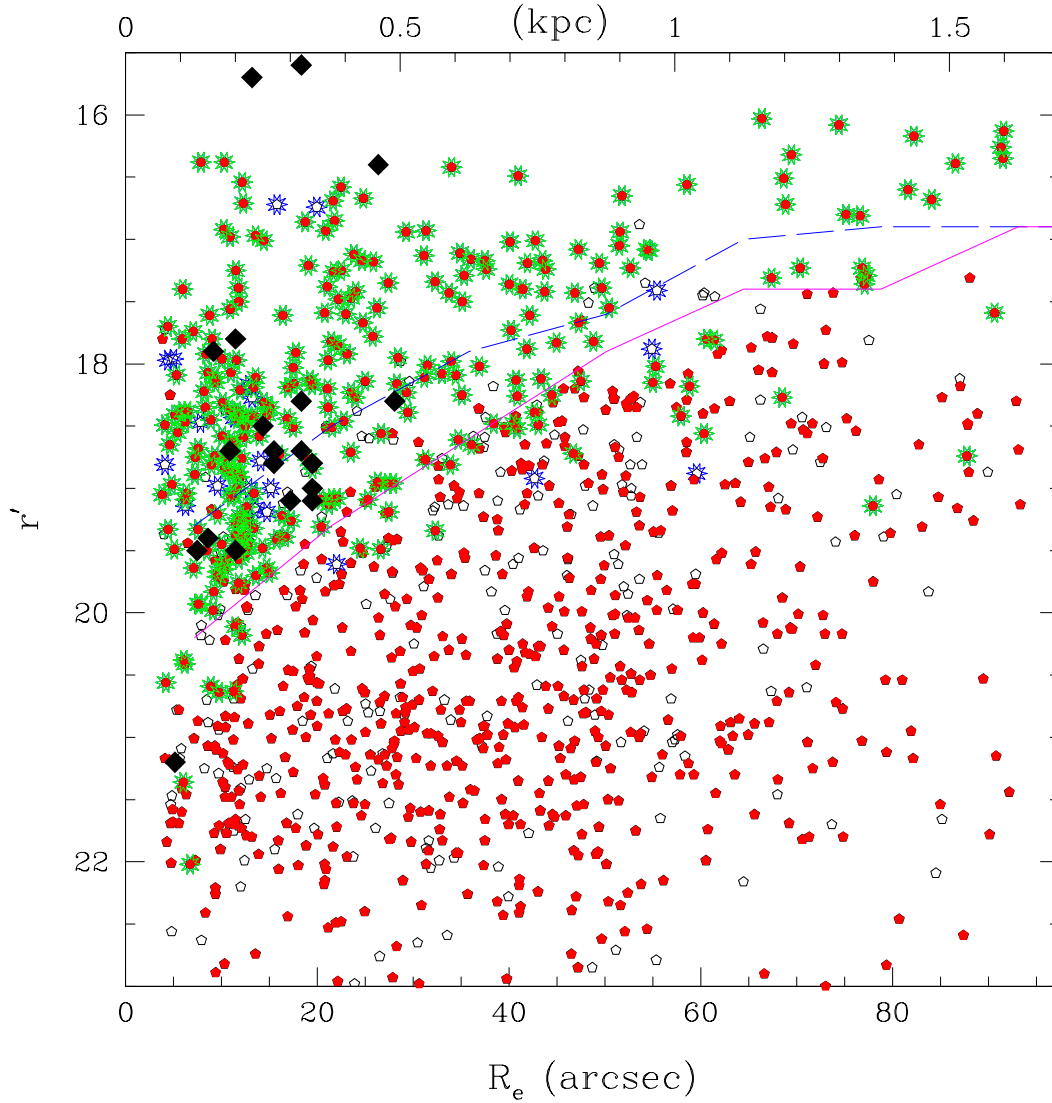


FIG. 12.— Results of 1200 artificial galaxy recovery tests. Small pentagons represent all artificial galaxies. Open pentagons are those galaxies that landed at least partially in chip gap regions of the MegaCam field or are largely obscured by bright saturated stars or other objects and are less likely to be recovered. Stars around these points denote that the simulated galaxy was recovered. Overlaid as black diamonds are the candidate real galaxies in this magnitude - effective radius plane. The solid line denotes the magnitude at which the recovery drops to 50% (in 2-magnitude bins), while the dashed line marks the boundary of 90% completeness.

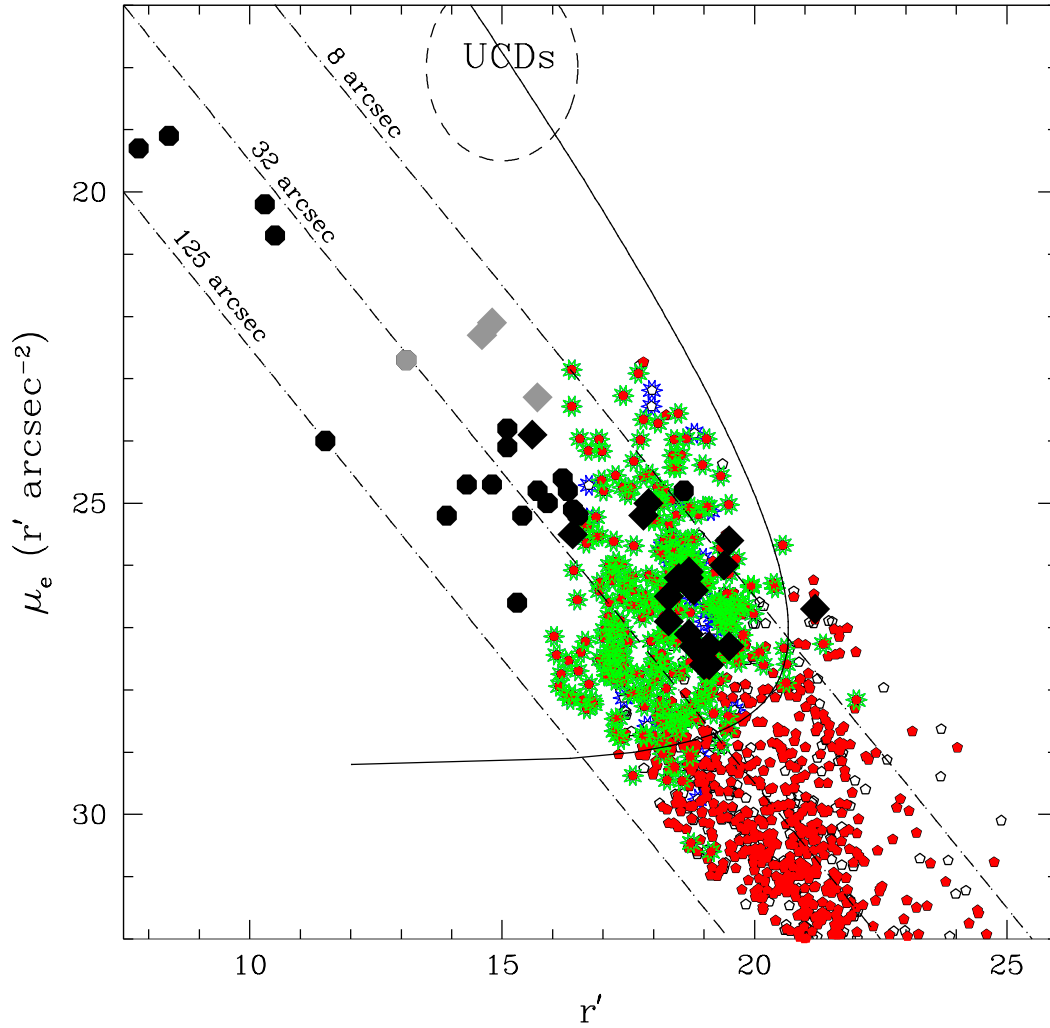


FIG. 13.— We plot the recovery of 1200 artificial galaxies in the magnitude-surface brightness plane. As before, pentagons represent all artificial galaxies. Stars around these points indicate that the simulated galaxy was recovered. Overlaid as black (gray) diamonds are the candidate real galaxies (BCDs) in this magnitude - effective surface brightness plane. Circles represent previously known M81 Group galaxies. DDO 82, shaded in gray, is a potential BCD. Lines of constant effective radius for exponential profiles are labeled. We draw a solid curved line which bounds the region of recovered artificial galaxies.

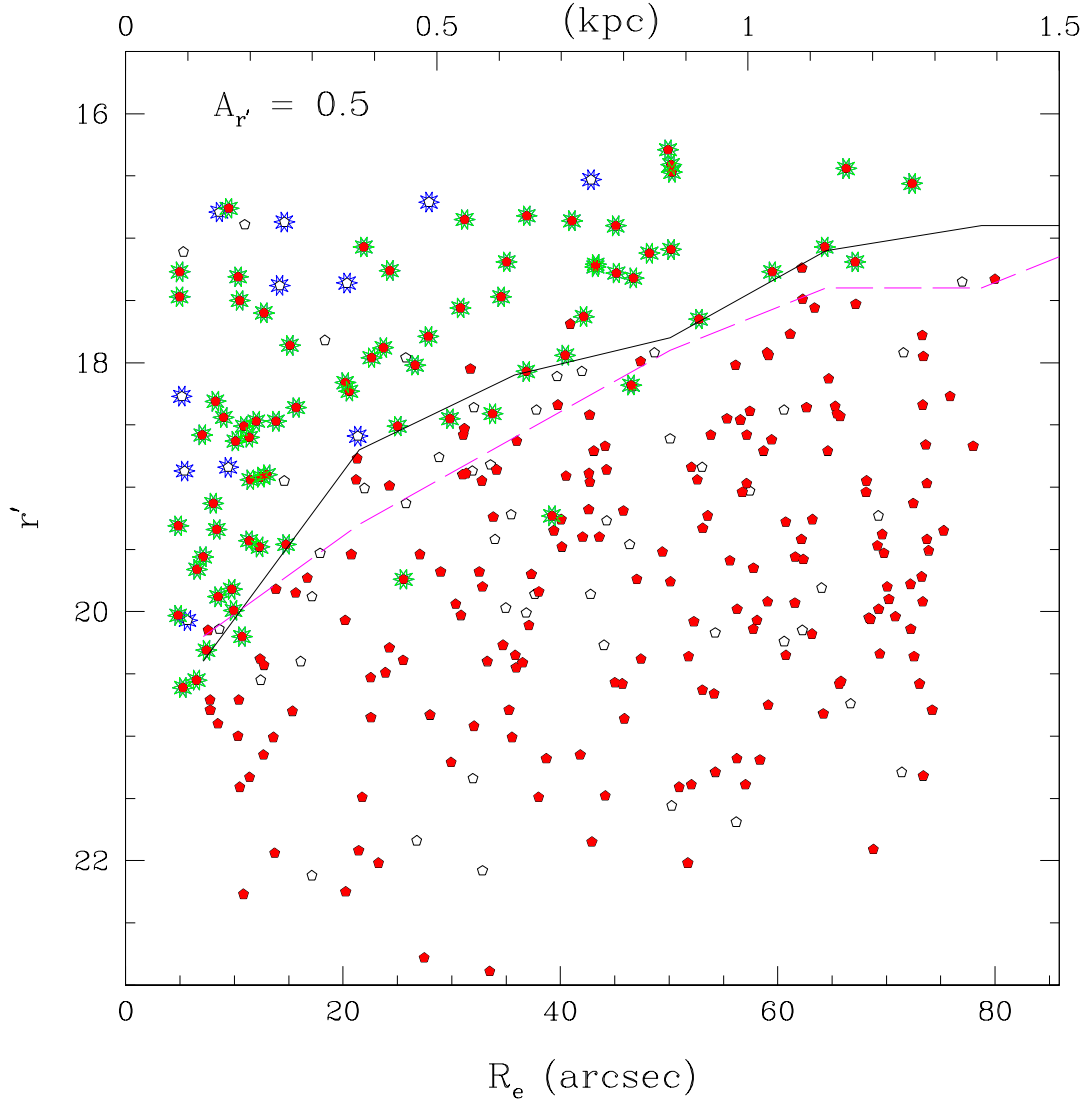


FIG. 14.— Recovery results for objects simulated with 0.5 magnitudes of extinction. Symbols as in previous figures. The solid line represents the magnitude at which the recovery drops to 50% for these galaxies, while the dashed line denotes the magnitude at which the recovery for artificial galaxies with 0.-0.2 magnitudes of extinction drops to 50%.

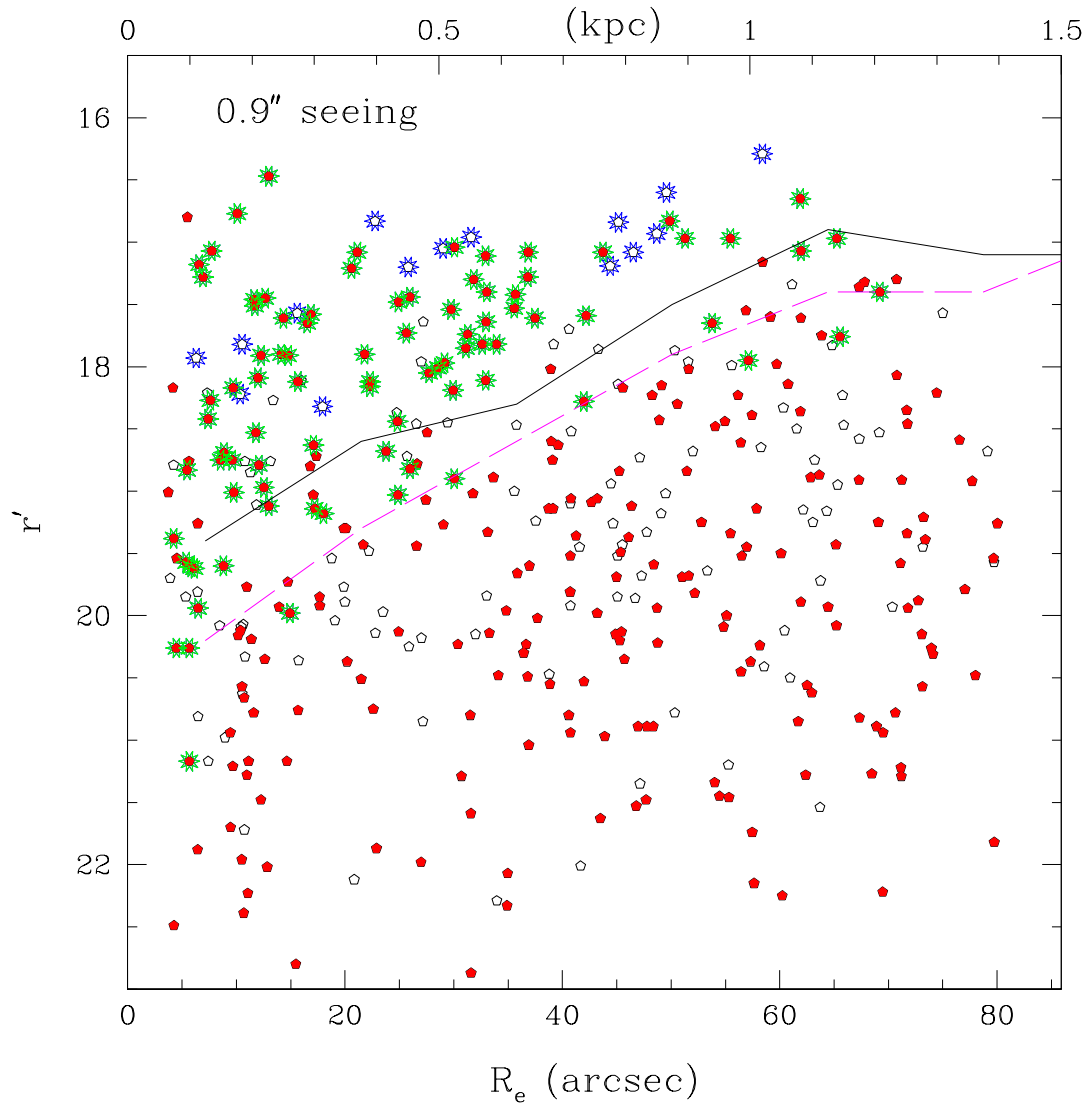


FIG. 15.— Recovery of 400 galaxies added with 0.9 arcsec seeing. Symbols as in previous figures. We compare results to that of the original 1200 simulations. The dashed line represents the magnitude at which the completeness drops to 50% for artificial galaxies added with seeing less than 0.75 arcsec. The solid line displays the 50% completeness for artificial galaxies added with 0.9 arcsec seeing.

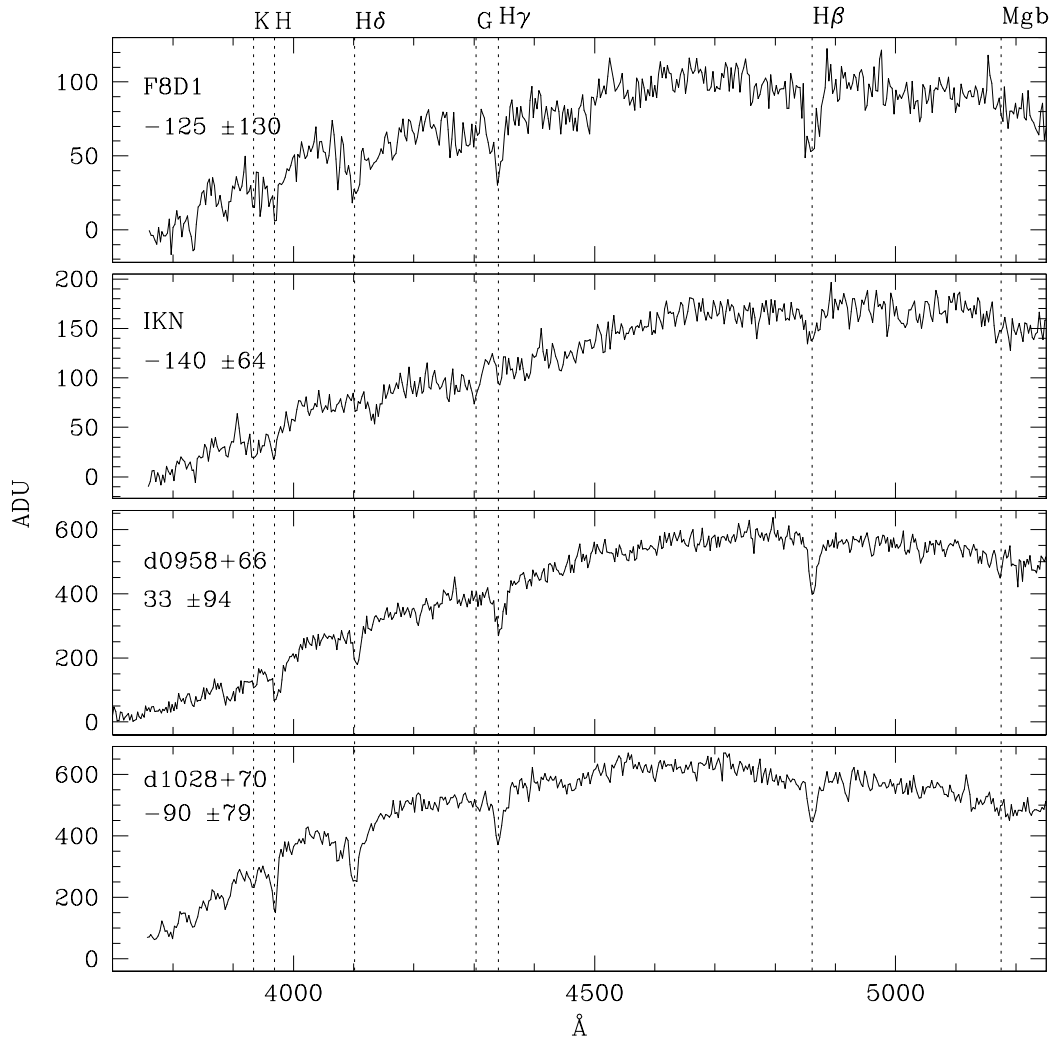


FIG. 16.— Spectra of 4 M81 group members obtained with Subaru/FOCAS. All spectra are shifted to the rest frame given the cross-correlation measured velocities as labeled.

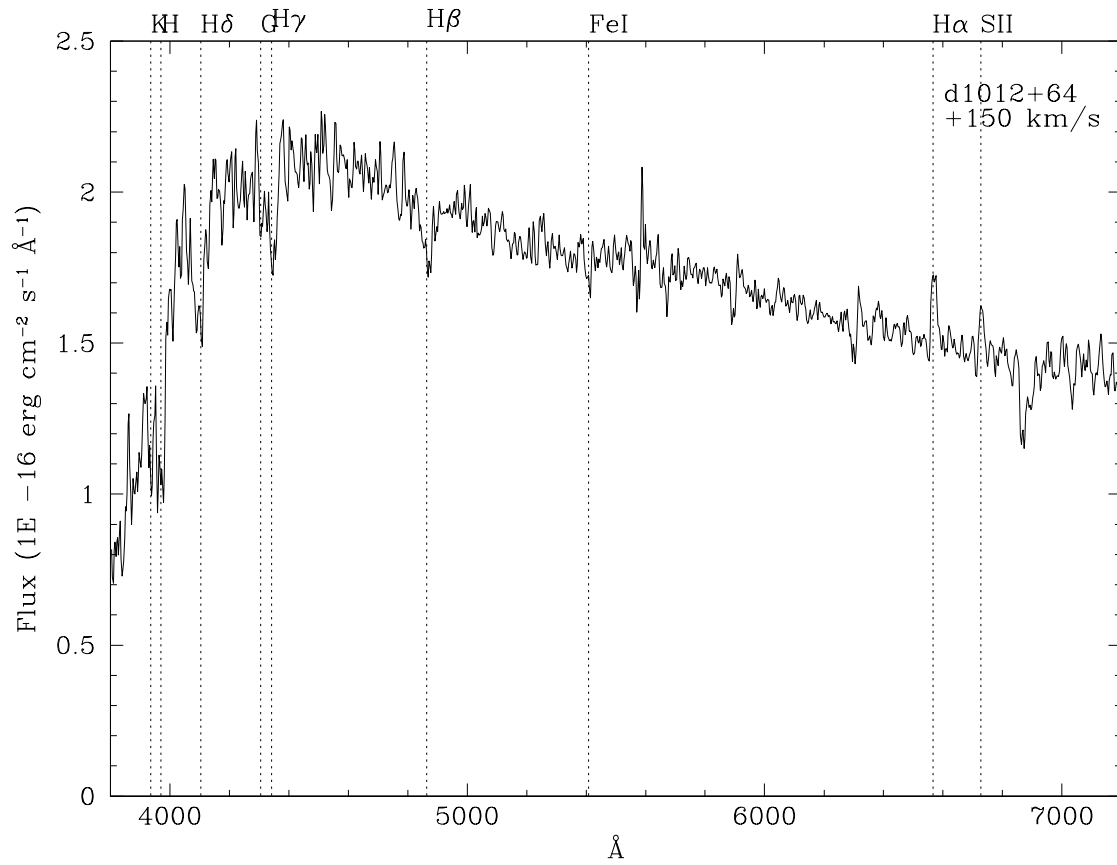


FIG. 17.— Spectrum of d1012+64 from the 6m BTA telescope. H α emission is detected and used to measure a heliocentric radial velocity.

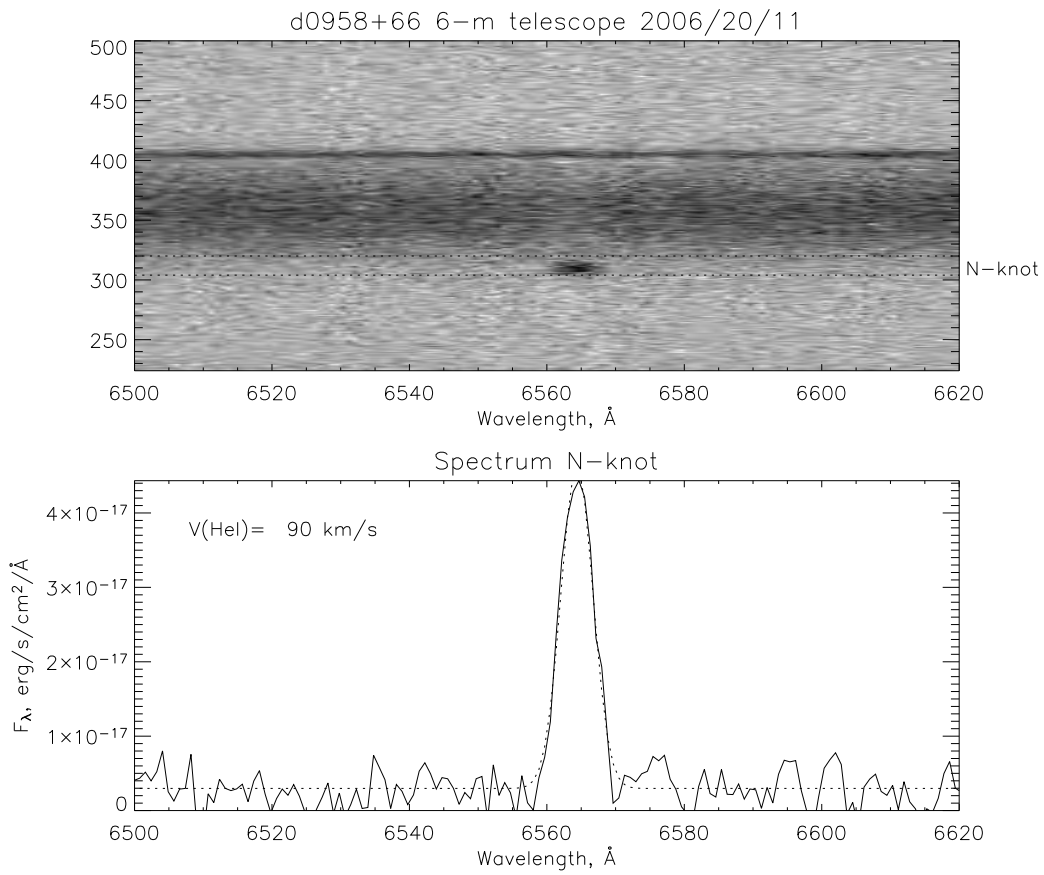


FIG. 18.— Spectrum of d0958+66 from the 6m BTA telescope. Strong H α emission is detected and used to measure a heliocentric radial velocity.

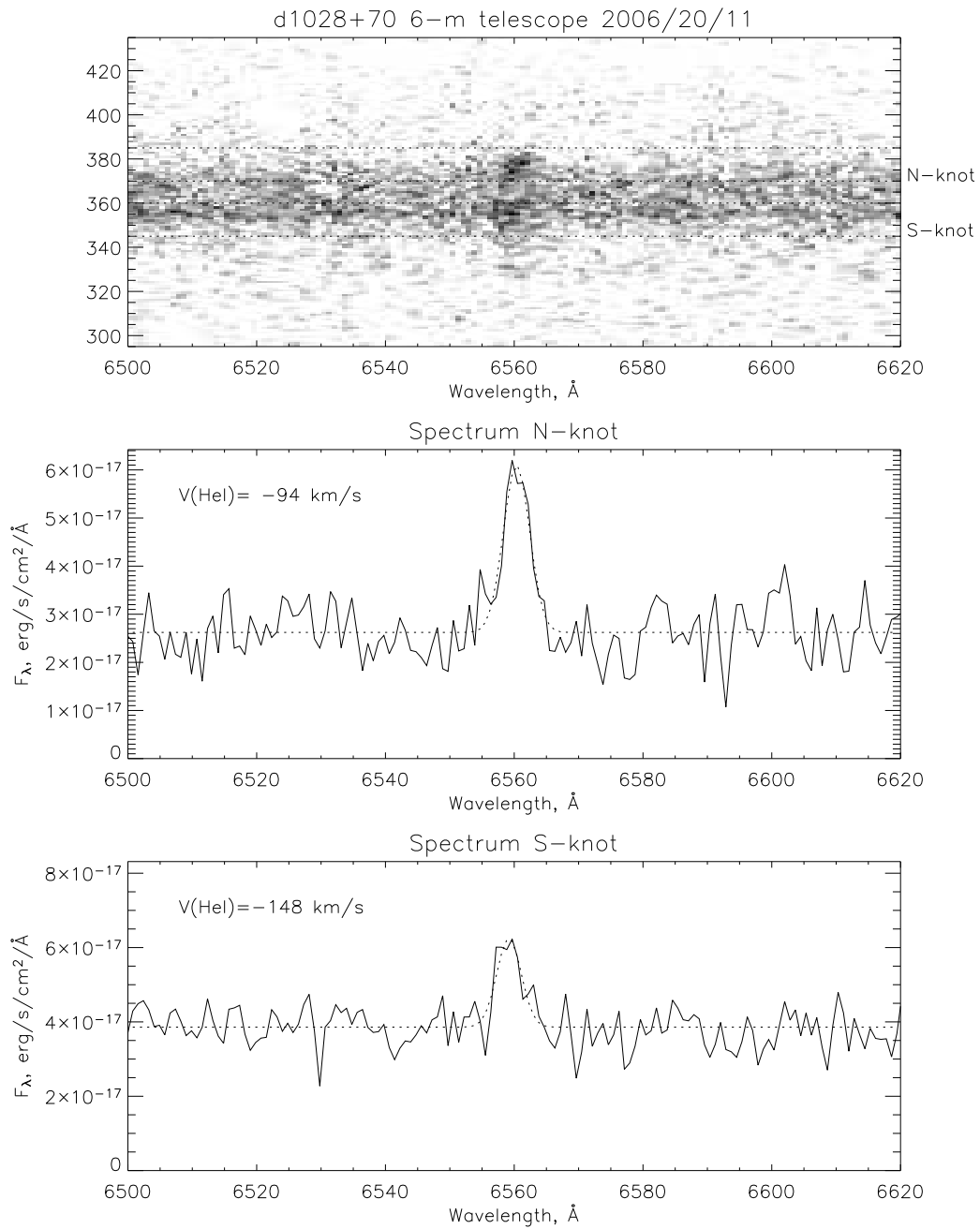


FIG. 19.— Spectrum of d1028+70 from the 6m BTA telescope. $\text{H}\alpha$ emission is detected in two separate knots which we label as N and S-knots.

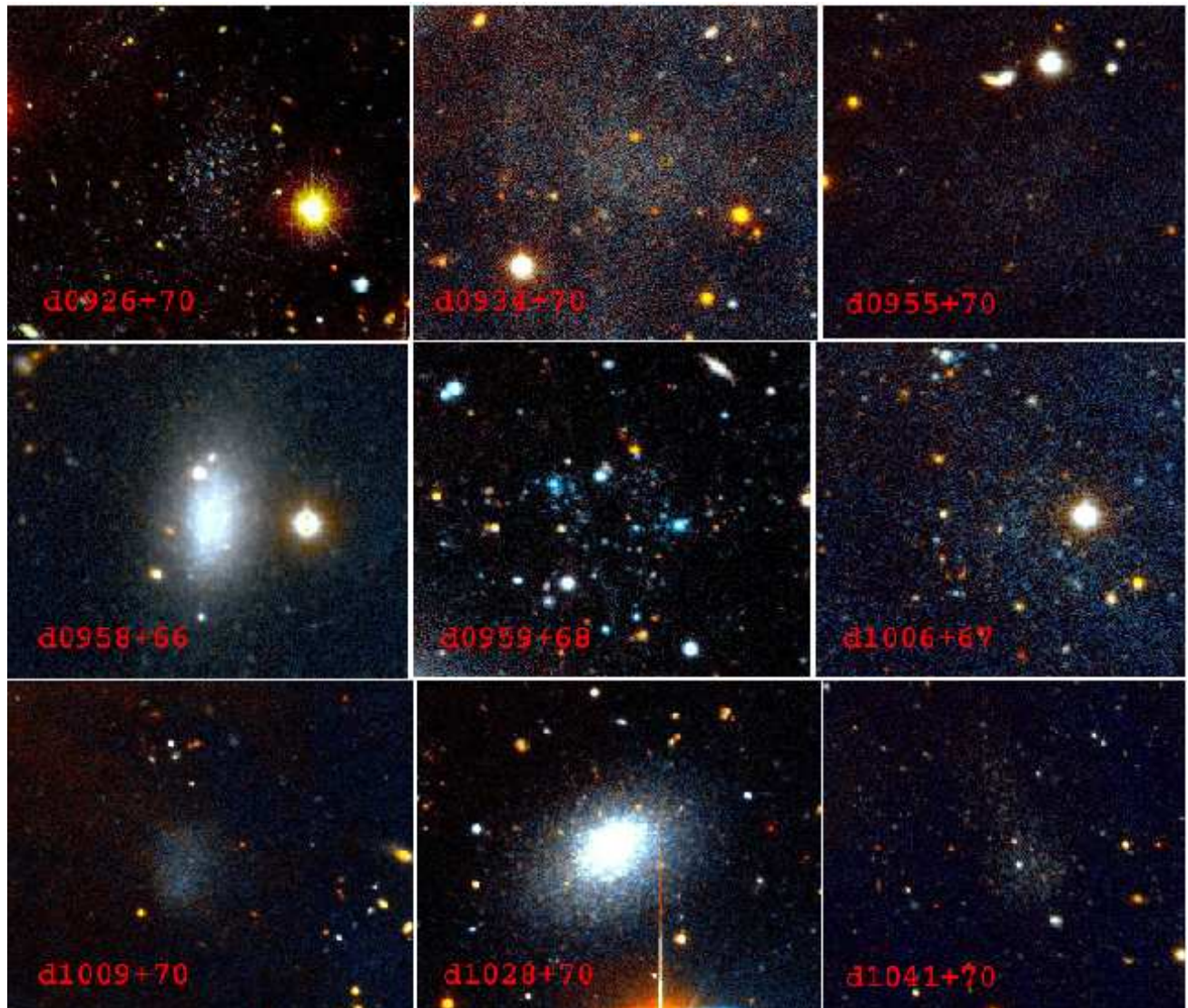


FIG. 20.— Color images based on 2 color photometry of 9 dwarf candidates.

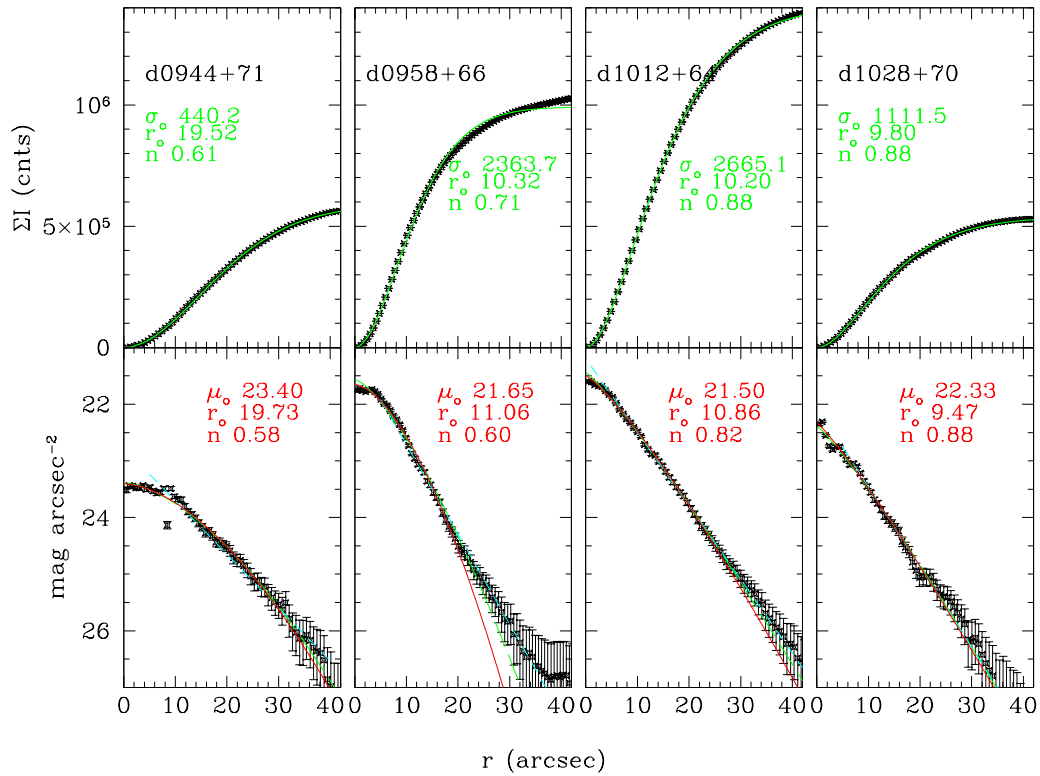


FIG. 21.— Curve of growth (top) and surface brightness profiles (bottom) for our 4 brightest candidates with best cumulative (top) and surface brightness profile (bottom) Sersic function fits overlaid. In the bottom plots, we also overlay the best cumulative Sersic function fit (green long dash) and best exponential surface brightness profile fit to outer radii only (cyan short dash).

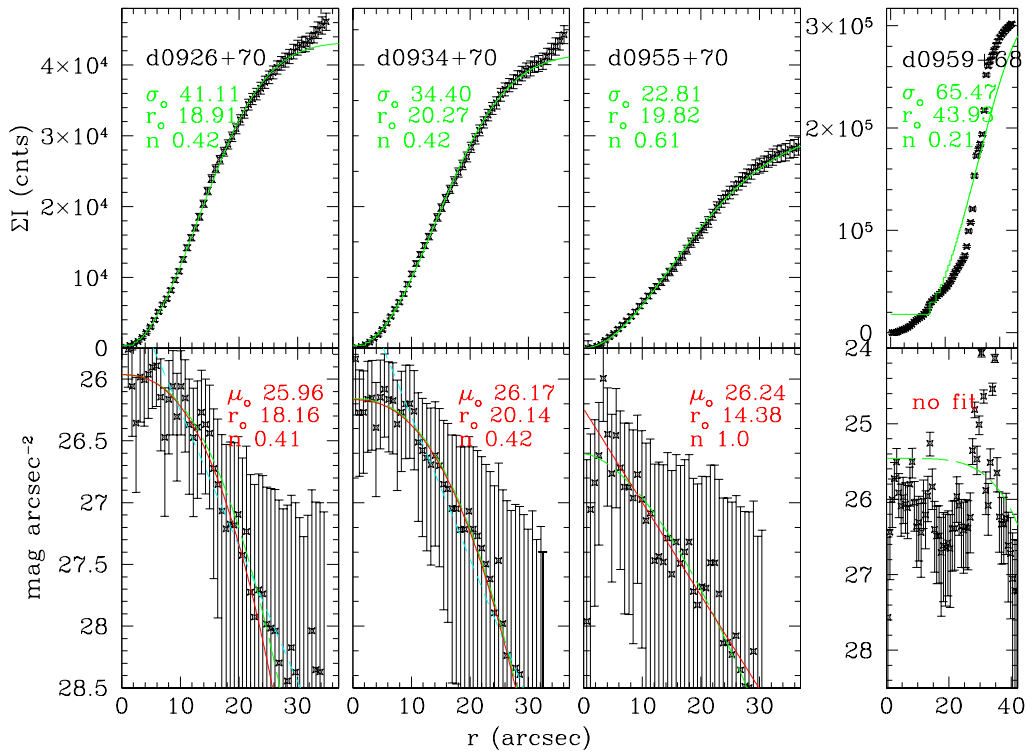


FIG. 22.— Fits for 4 of our candidate galaxies, as in Figure 21. Curve of growth profile data points which exhibit a sharp increase in slope beyond 10 arcsec were truncated during profile fitting. For d0926+70 and d0934+70 this rise was determined to be due to nearby bright cirrus. For d0959+68 we were unable to obtain a surface brightness profile fit due to the fact that this object consists almost entirely of bright stars without a significant low surface brightness component.

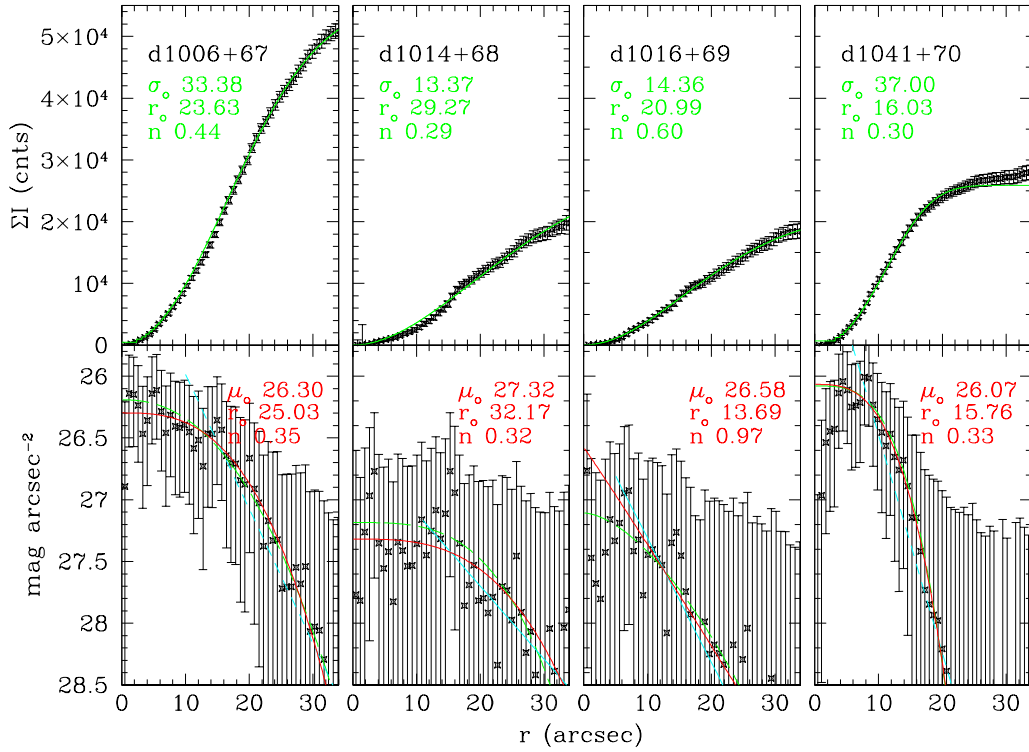


FIG. 23.— Fits for 4 of our candidate galaxies, as in Figure 21.

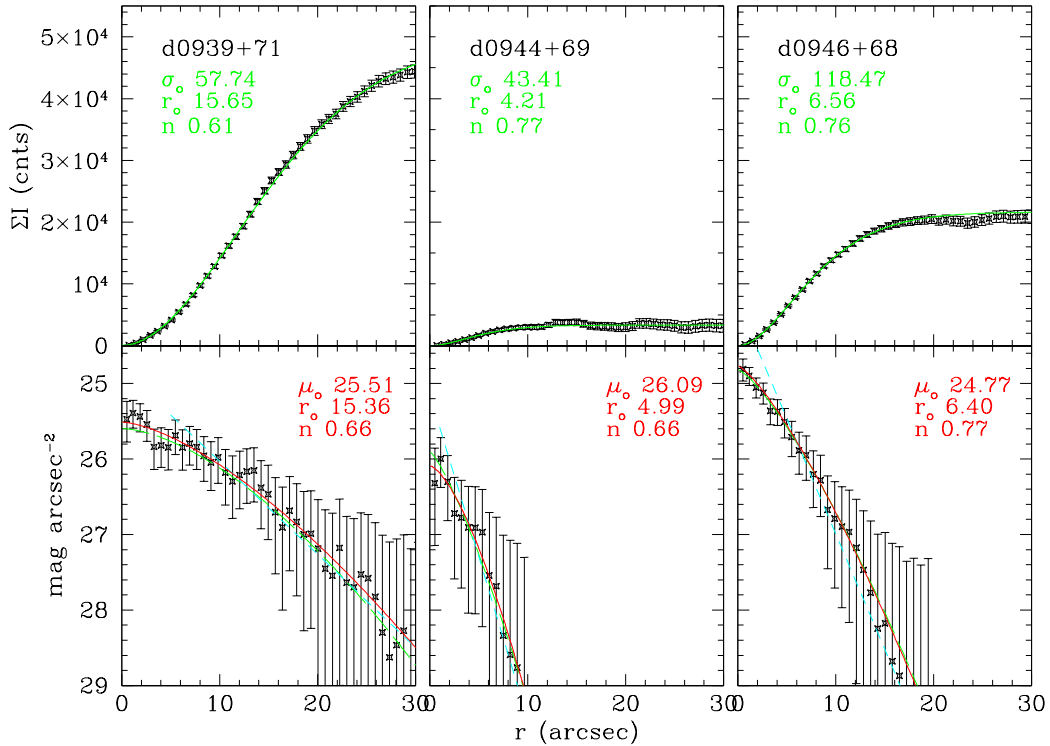


FIG. 24.— Fits for 3 potential background galaxies, as in Figure 21.

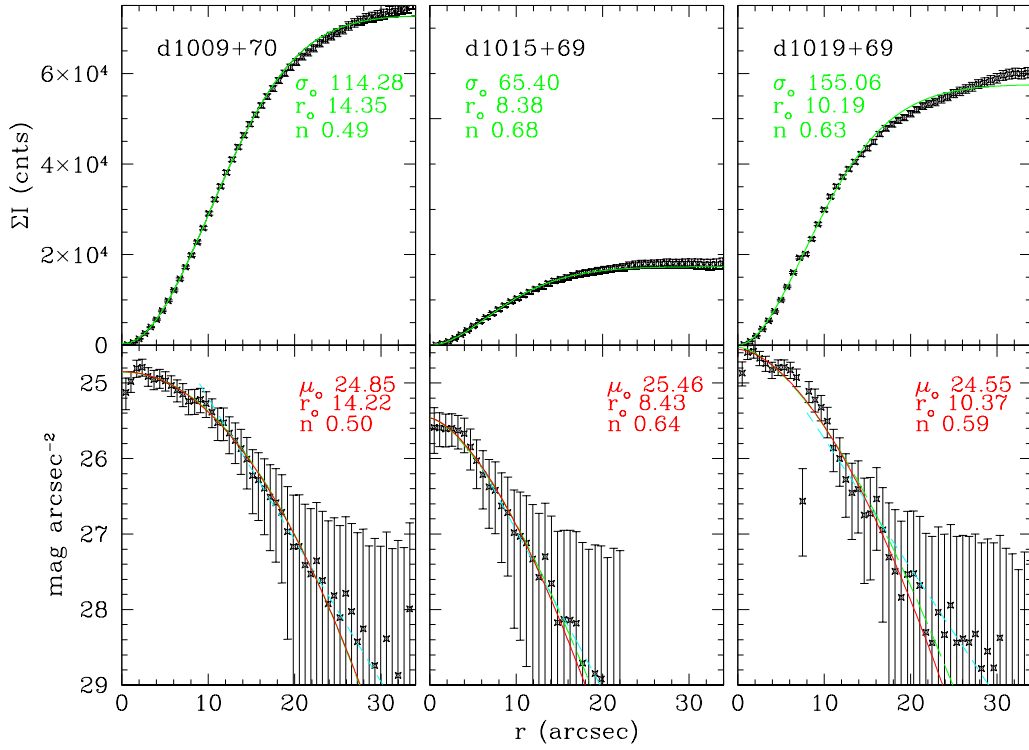


FIG. 25.— Fits for a further 3 likely background objects, as in Figure 21.

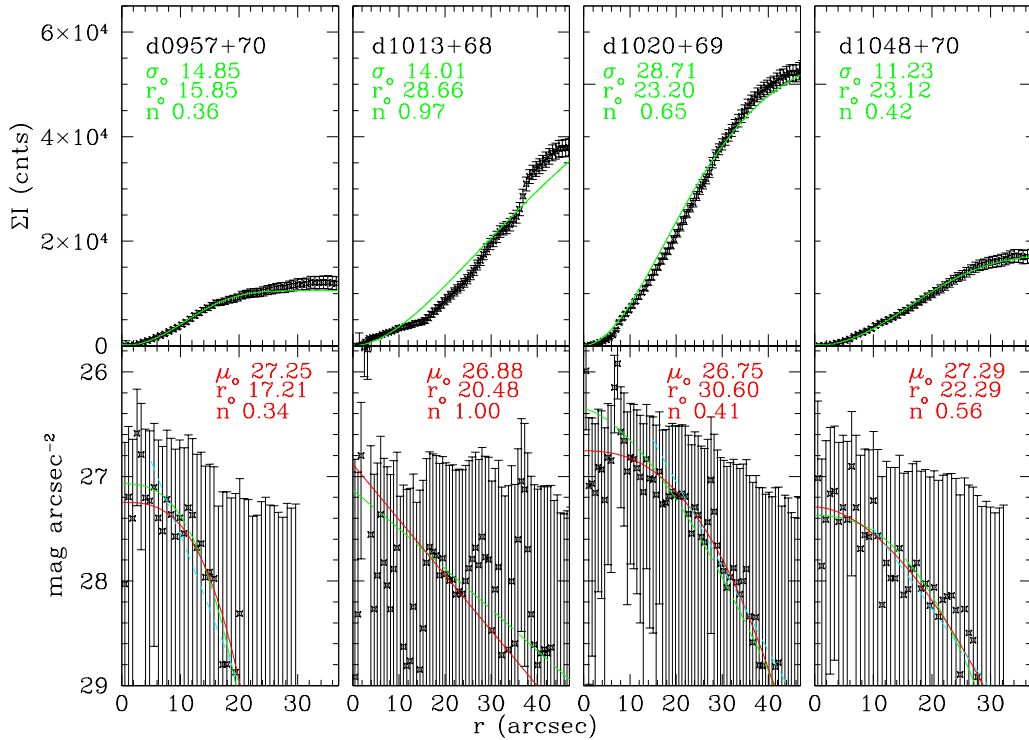


FIG. 26.— Fits for 4 of our poorer candidates, as in Figure 21.

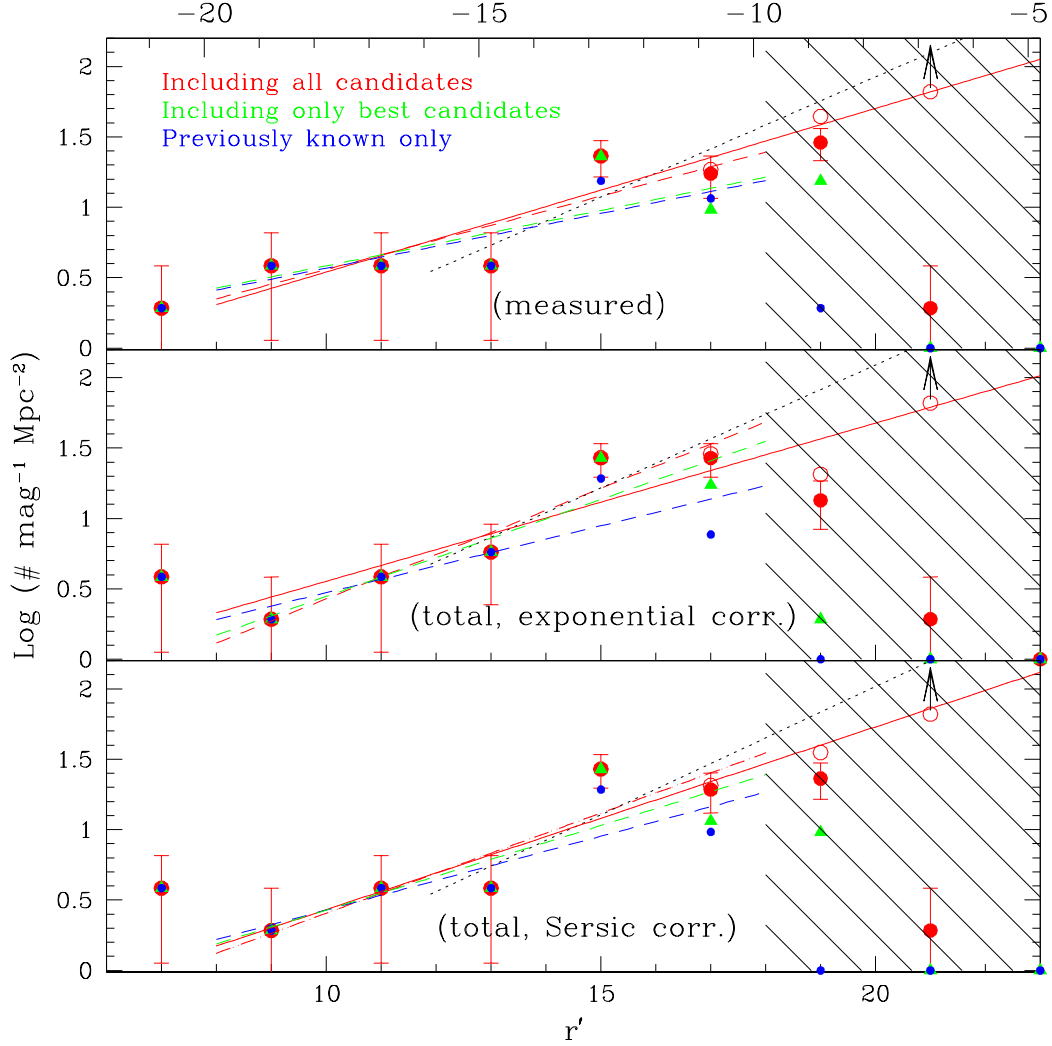


FIG. 27.— Differential luminosity function for the M81 Group, using measured magnitudes (top), total magnitudes corrected assuming exponential profiles (middle), and total magnitudes assuming Sersic profiles (bottom). Counts are normalized to the area of the survey coverage. Solid red circles include previously known group members and all candidates from this survey. Open circles are corrected for incompleteness. Green triangles include only the best candidates from this work. Small blue circles represent only previously known group members. The hatched region denotes where this survey is incomplete; brightward of this we expect nearly 100% completeness in the detection of member dwarfs. The best power law fits to the data brightward of our completeness limit are shown by the dashed lines, while the solid line is the best fit for corrected counts. Dotted lines are faint-end only fits to all counts within the magnitude range $-15 \leq r' < -10$. The arrow in the final data point signifies that a minimum completeness correction based on good seeing/low extinction simulations was applied.

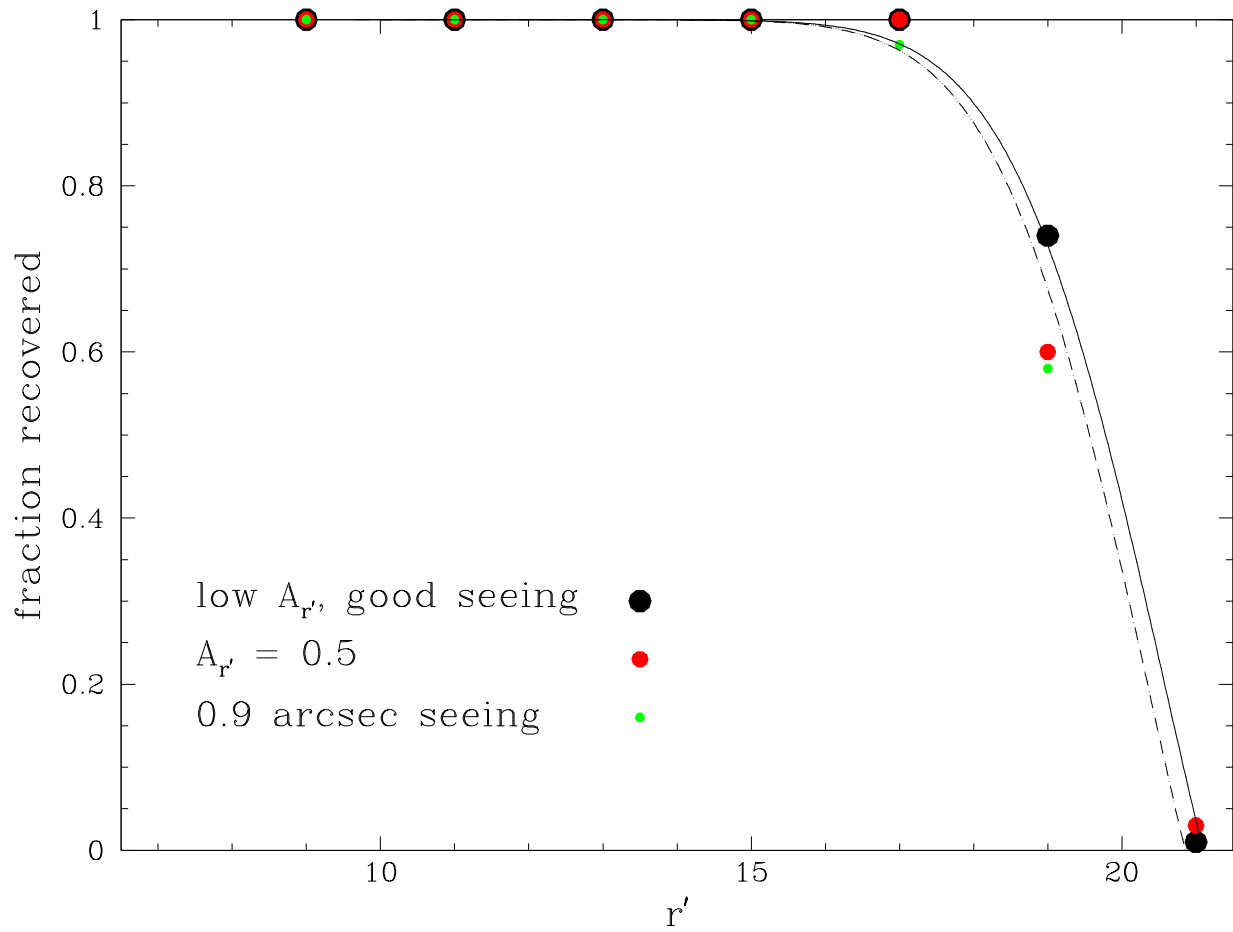


FIG. 28.— We plot detection efficiency as a function of magnitude. The solid line is the best fit to the good seeing, low extinction case, while the dashed line incorporates the survey average effects of seeing, extinction, single exposure regions, and loss of survey area due to coverage by brighter objects.

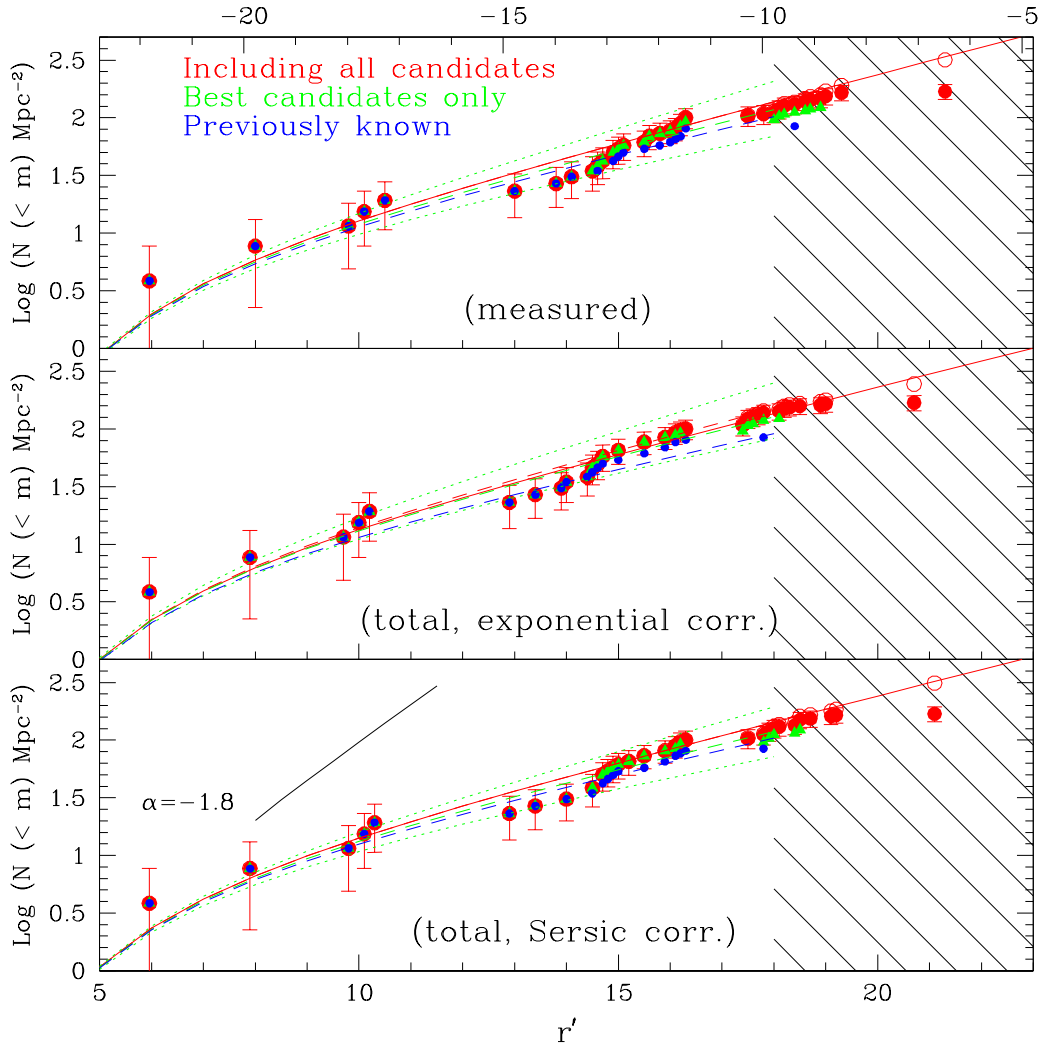


FIG. 29.— Cumulative luminosity function for the M81 Group, using measured magnitudes (top), magnitudes corrected assuming exponential profiles (middle), and corrected magnitudes assuming Sersic profiles (bottom). Counts are normalized to the area of the survey coverage. Large solid circles include previously known group members and all candidates from this survey. Open circles are corrected for incompleteness. The hatched region denotes where this survey is incomplete; brightward of this we expect nearly 100% completeness in the detection of member dwarfs. The best cumulative Schechter function fits to the data brightward of our completeness limit are shown by the dashed lines. The solid red line is the best fit to completeness corrected counts. Dotted lines are $\pm 1\sigma$ fits for the sample of 'best' candidates.

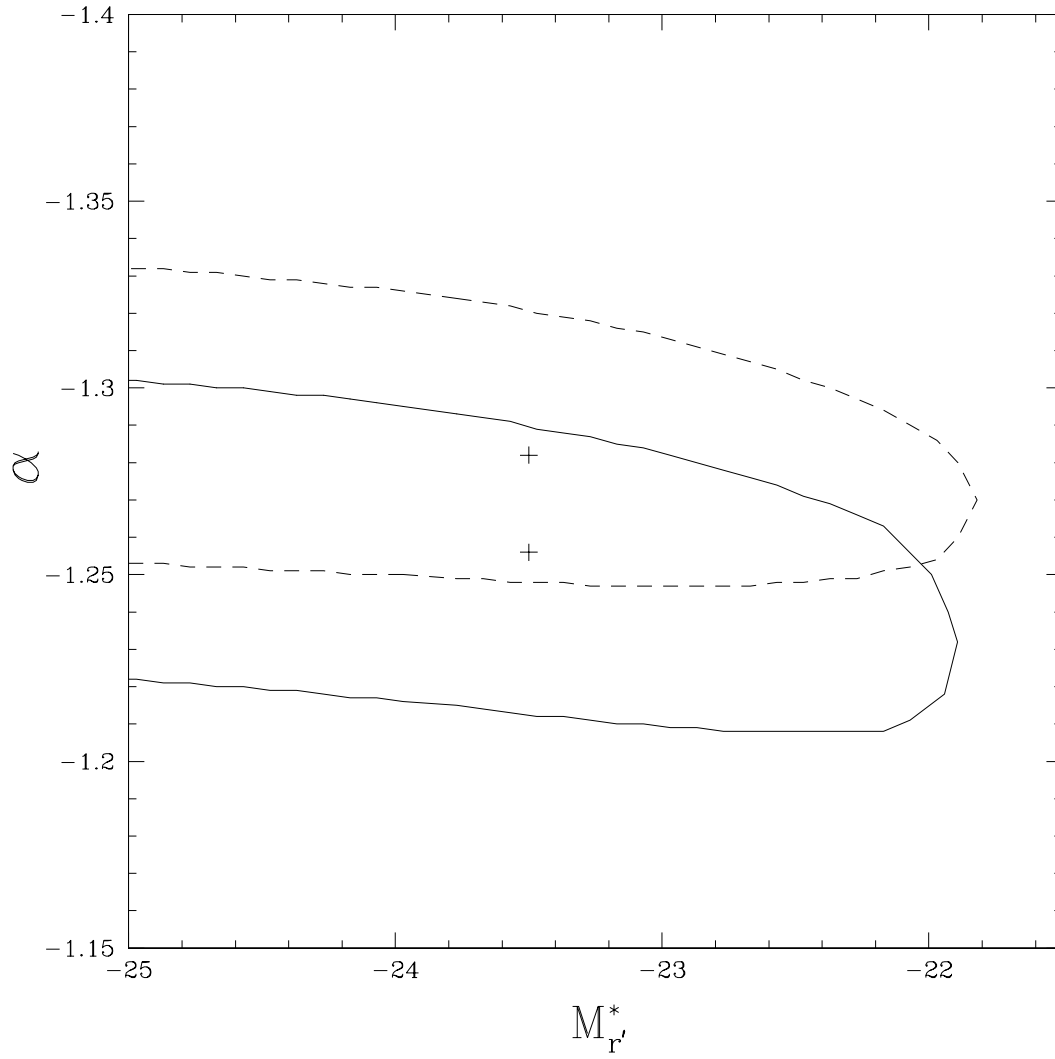


FIG. 30.— We display 1σ error ellipses for the luminosity function parameters α and M_* for our best (solid) and all (dashed) candidate samples using Sersic corrected magnitudes. The values for M_* are unconstrained at the bright end.

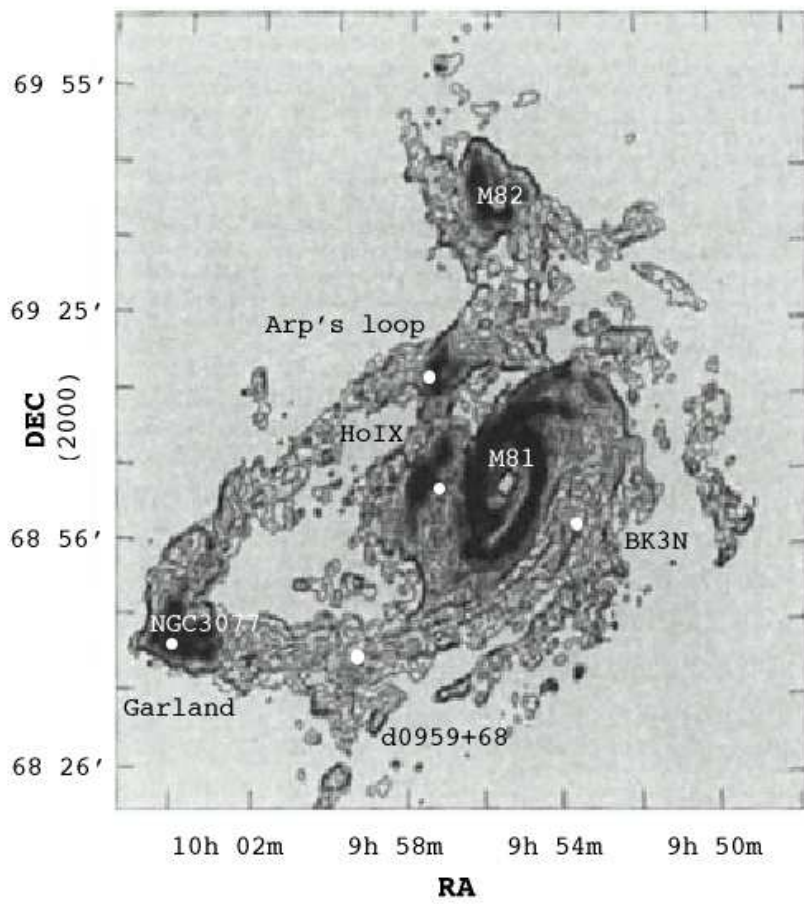


FIG. 31.— We display the M81 HI map of Yun et al. (1994). Overlaid (white dots) are the positions of the five suspected tidal dwarfs. d0959+68 is found to lie in the tidal bridge between M81 and NGC3077. Adapted by permission of Macmillan Publishers Ltd: Nature, copyright 1994.

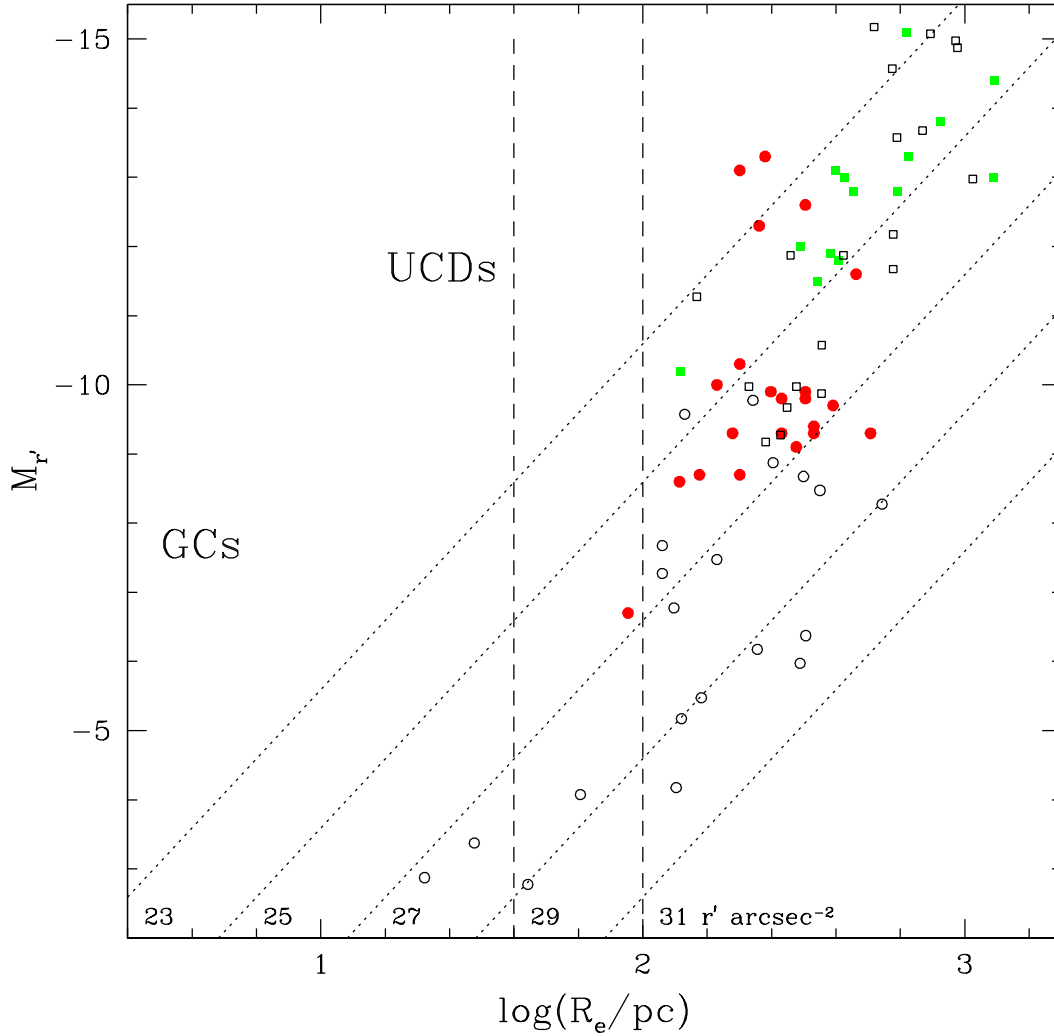


FIG. 32.— Locations of our M81 candidates on a total magnitude vs half-light radius plane (filled circles), along with previously known M81 galaxies (filled squares), Local Group previously known galaxies (open squares) (Irwin & Hatzidimitriou 1995; Mateo 1998; McConnachie & Irwin 2006) and recent discoveries (open circles) (Simon & Geha 2007; Belokurov et al. 2007a; Willman et al. 2005; Walsh et al. 2007; Zucker et al. 2006; Martin et al. 2006; Ibata et al. 2007; Irwin et al. 2008). To transform V magnitudes to r' , we assume $r' = V - 0.84(V - R) + 0.13$ (Fukugita et al. 1996b). The rough locations of globular clusters and Fornax UCDs on this plane are shown. Globular Clusters have sizes that range up to ~ 40 pc, while Local Group galaxies have sizes generally larger than ~ 100 pc. The size gap region falls between the two dashed lines. Lines of constant effective surface brightness are also shown.

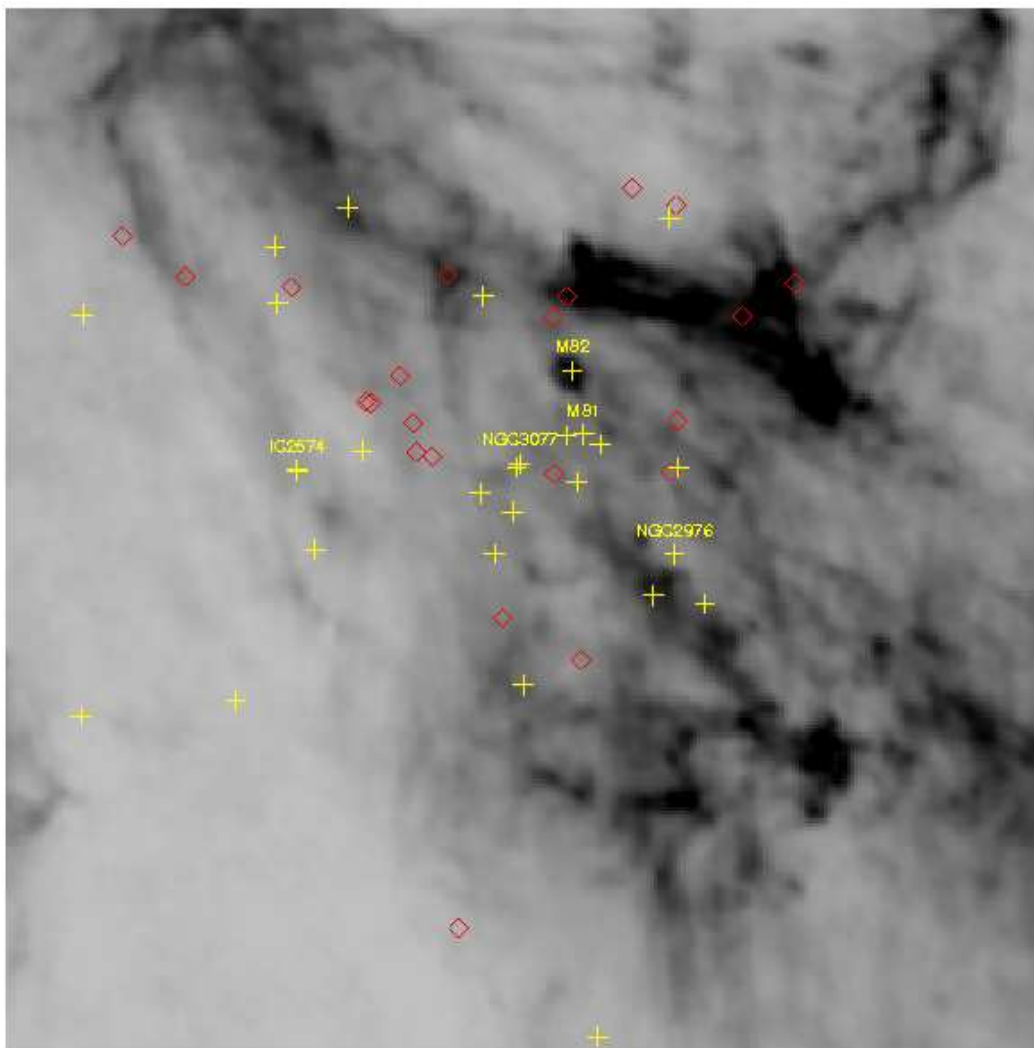


FIG. 33.— We display the M81 galaxy detections superimposed on the Schlegel et al. (1998) dust map. Red diamonds represent newly discovered candidate group members while yellow crosses correspond to previously known group members.

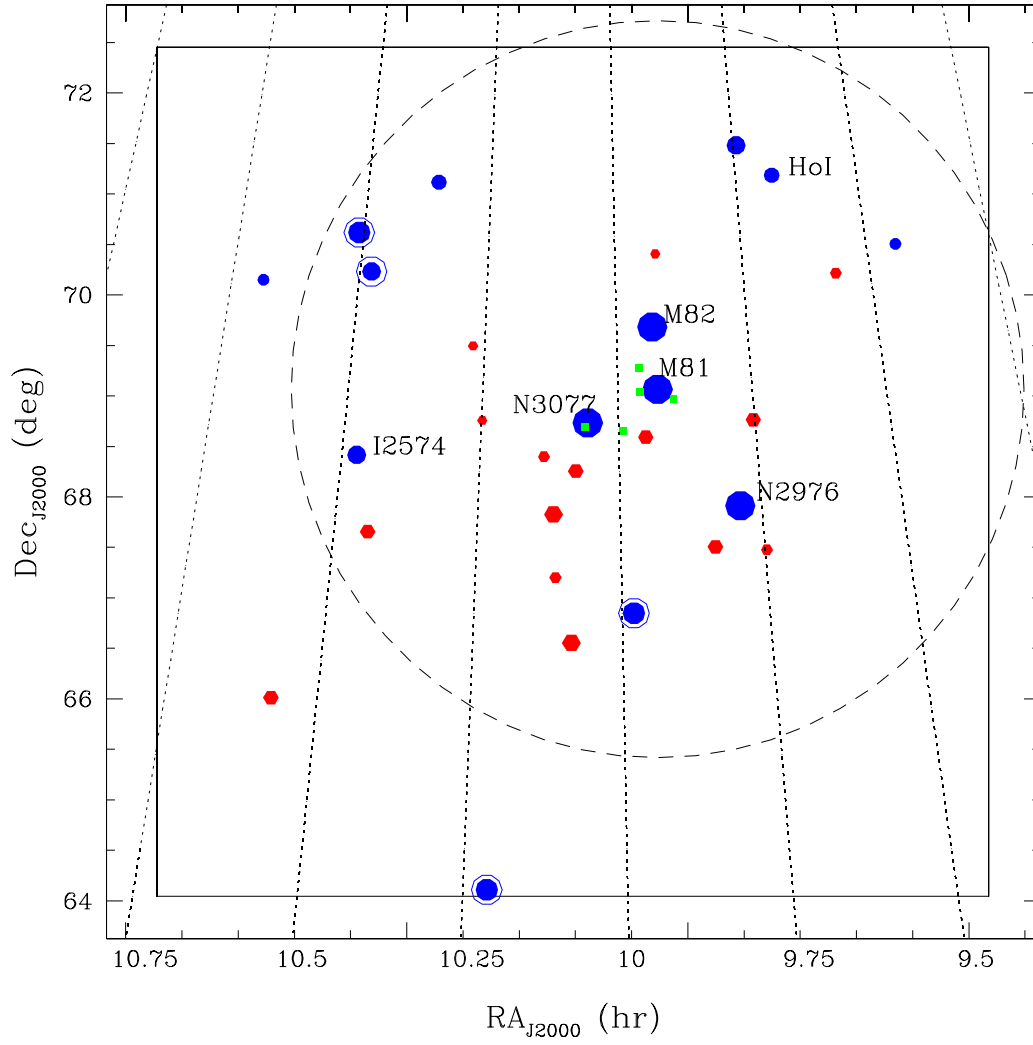


FIG. 34.— Projected distribution of early type (red hexagons) and late type (blue circles) galaxies. Green squares indicate candidate tidal dwarfs. The location of BCD candidates, including DDO 82, are marked by blue rings. We include in this plot only previously known and best candidates. Size indicates surface brightness with larger points denoting brighter effective surface brightness.

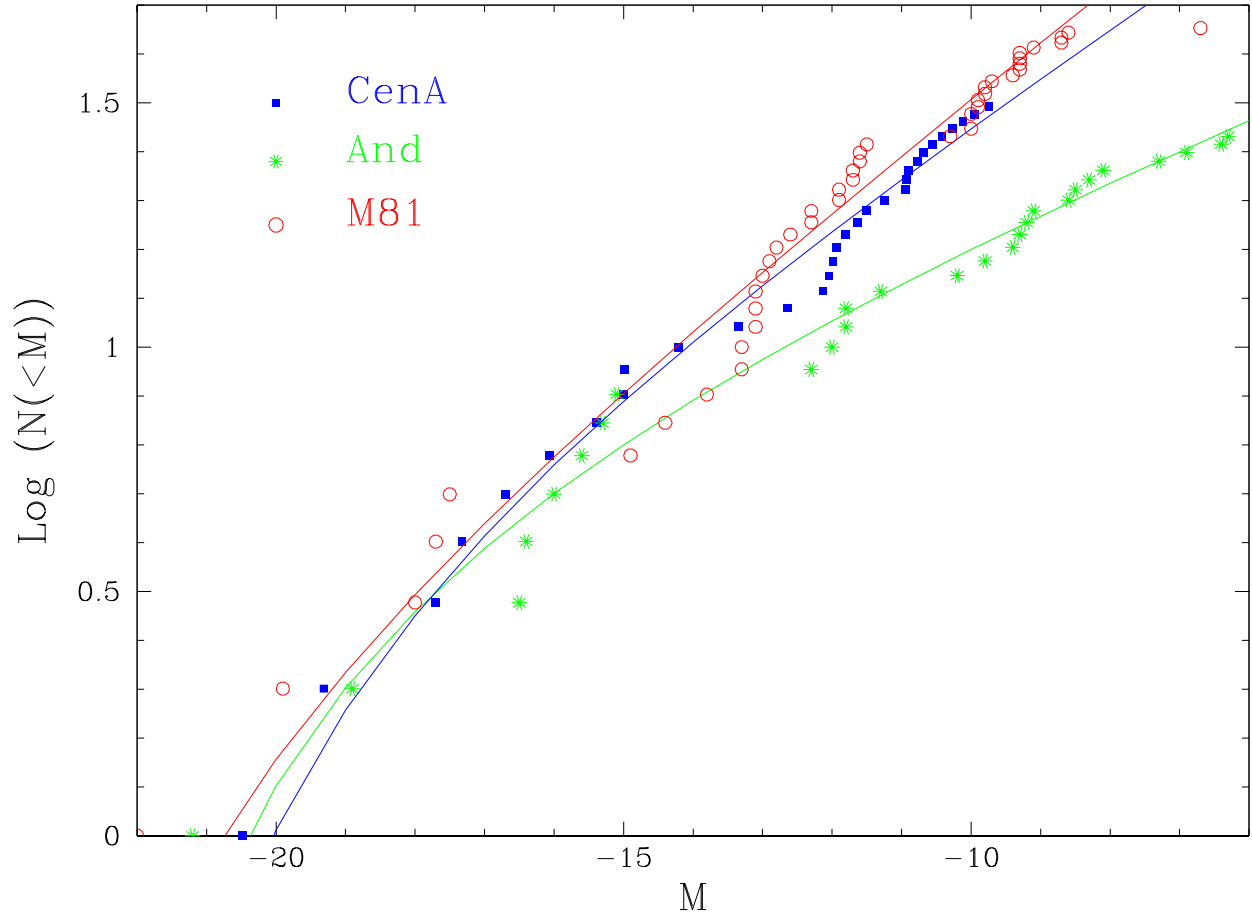


FIG. 35.— Cumulative LFs for Cen A (B band, squares), Andromeda (V band, stars), and M81 (r' band, open circles) satellites. For clarity, we do not include error bars. Applying a cumulative Schechter function to these data, we find faint-end slopes of $-1.13^{+0.06}_{-0.06}$ for Andromeda systems, $-1.23^{+0.04}_{-0.10}$ for Cen A, and $-1.28^{+0.06}_{-0.06}$ for M81.